ABSTRACT

Title of Document:	SYNTHESIS AND INTEGRATION OF ONE-DIMENSIONAL NANOSTRUCTURES FOR CHEMICAL GAS SENSING APPLICATIONS
	Prahalad Madhavan Parthangal, Ph.D, 2007
Directed By:	Michael Zachariah, Professor, Departments of Mechanical Engineering and Chemistry

The need for improved measurement technology for the detection and monitoring of gases has increased tremendously for maintenance of domestic and industrial health and safety, environmental surveys, national security, food-processing, medical diagnostics and various other industrial applications. Among the several varieties of gas sensors available in the market, solid-state sensors are the most popular owing to their excellent sensitivity, ruggedness, versatility and low cost. Semiconducting metal oxides such as tin oxide (SnO_2), zinc oxide (ZnO), and tungsten oxide (WO_3) are routinely employed as active materials in these sensors. Since their performance is directly linked to the exposed surface area of the sensing material, one-dimensional nanostructures possessing very high surface to volume ratios are attractive candidates for designing the next generation of sensors. Such nano-sensors also enable miniaturization thereby reducing power consumption. The key to achieve success in one-dimensional nanotechnologies lies in

assembly. While synthesis techniques and capabilities continue to expand rapidly, progress in controlled assembly has been sluggish due to numerous technical challenges.

In this doctoral thesis work, synthesis and characterization of various one-dimensional nanostructures including nanotubes of SnO_2, and nanowires of WO_3 and ZnO, as well as their direct integration into miniature sensor platforms called microhotplates have been demonstrated. The key highlights of this research include devising elegant strategies for growing metal oxide nanotubes using carbon nanotubes as templates, substantially reducing process temperatures to enable growth of WO_3 nanowires on microhotplates, and successfully fabricating a ZnO nanowire array based sensor using a hybrid nanowire-nanoparticle assembly approach. In every process, the gas-sensing properties of one-dimensional nanostructures were observed to be far superior in comparison with thin films of the same material. Essentially, we have formulated simple processes for improving current thin film sensors as well as a means of incorporating nanostructures directly into miniature sensing devices.

Apart from gas sensing applications, the approaches described in this work are suitable for designing future nanoelectronic devices such as gas-ionization, capacitive and calorimetric sensors, miniature sensor arrays for electronic nose applications, field emitters, as well as photonic devices such as nanoscale LEDs and lasers.

SYNTHESIS AND INTEGRATION OF ONE-DIMENSIONAL
NANOSTRUCTURES FOR CHEMICAL GAS SENSING APPLICATIONS

By

Prahalad Madhavan Parthangal

Dissertation submitted to the Faculty of the Graduate School of the
University of Maryland, College Park, in partial fulfillment
of the requirements for the degree of
Doctor of Philosophy
2007

Advisory Committee:
Professor Michael Zachariah, Chair
Dr. Richard Cavicchi
Professor Phillip DeShong
Professor Raymond Adomaitis
Professor Sheryl Ehrman
Professor Bao Yang

Dedication

This thesis is dedicated to the memory of Swaminathan Gowrisankaran, a close friend and classmate through the first 21 years of my life.

Acknowledgements

Table of Contents

List of Abbreviations

1. GB – gigabytes

2. VOC – volatile organic compound

3. CNT – carbon nanotube

4. MO_x – metal oxide

5. NW – nanowire

6. CVD – chemical vapor deposition

7. MEMS – micro-electromechanical systems

8. SEM – scanning electron microscope

9. TEM – transmission electron microscope

10. SAED – specific area electron diffraction

11. XRD – x-ray diffraction

12. PL – photoluminescence

13. VS – vapor-solid

14. VLS – vapor-liquid-solid

15. LED – light-emitting diode

List of Figures

Appendix A

Chapter 1

Introduction

1.1 Overview

The purpose of this doctoral thesis work is to synthesize and integrate one-dimensional nanostructures of semiconducting metal oxides into miniature devices, towards chemical gas sensing applications. The first portion of this chapter outlines the enormous impact of nanotechnology on diverse fields of research. A brief introduction to the world of chemical gas sensors, their operating principles and applications is presented in the next section. The final section describes the motivations for this work and the overall structure of this investigation.

1.2 Nanotechnology

Nanotechnology has caught the imagination of researchers in the scientific community over the past decade, and has provided tremendous opportunities for exploring new avenues of research and revolutionized technologies in various disciplines. Nanotechnology has also pioneered the emergence of an extraordinary number of interdisciplinary research areas, encouraging collaborations among researchers from diverse backgrounds. In 2001, the United States Government established a federal research and development program to coordinate multi-agency efforts in nanoscale science, engineering and technology, called the National Nanotechnology Initiative (NNI) with an estimated funding budget of $1.39 billion for the fiscal year 2007.[1] The

reason for such colossal interest in nanostructures (structures that have at least one dimension between 1-100 nm) is due to several peculiar and attractive properties that these structures possess, in comparison with their bulk counterparts.

The semiconductor industry may be exemplified as one of the biggest contributors as well as beneficiaries from nanotechnology, with the miniaturization of devices like transistors to the nanoscale, allowing millions of components to be integrated into a single chip, providing faster operation, and reducing power consumption and cost. Nanomedicine is also an emerging field of intense research focused on achieving medical intervention at the molecular scale for curing diseases, targeting and destroying cancer cells, and repairing damaged tissues.[2]

A few of the major reported successes in implementing nanometer technology for commercial product development include visual display units for televisions using carbon nanotube arrays by Motorola Inc. and Applied Nanotech Inc., highly transparent carbon nanotube inks for conductive coatings and circuits by Eikos Inc., the world's first 16 GB NAND memory chip by Samsung Corp., 45 nm nano-processor by Intel Corp. etc. Nanoparticles of several different kinds are regularly employed in industrial processing for chemo-mechanical polishing, fillers for conductive polymers, coatings to prevent corrosion, catalyst supports etc.[1]

In the academic world, several prototypes of nanoscale electronic and photonic devices including single nanowire lasers, single electron transistors, memory units,

sensors, actuators and optical detectors have been successfully conceived, designed and fabricated.[3-7] However, even though several nano-devices can be routinely fabricated in research laboratories at this stage, the processing costs involved are still extremely high for commercial purposes. Hence, it is crucial to develop innovative methods to merge nanoscale research with cutting edge technology in a cost-effective manner. The next section of this chapter is devoted to the topic of chemical gas sensors, their fundamental operating principles and applications, and the importance of nanotechnology in improving the current state of sensors.

1.3 The World of Chemical Gas Sensors

1.3.1 Need for Gas Sensors

One of the major consequences of the progressive industrialization of society through the twentieth century has been the need for improved measurement tools for monitoring and controlling chemical vapors in domestic and industrial settings, and preservation of environment as well. A few of the areas in which reliable gas sensors are indispensable are listed below.

a. <u>Domestic and industrial safety</u>: Detection and control of physically harmful gases such as carbon monoxide (CO), ammonia (NH_3), nitrous oxides (NO_x); flammable volatile organic compounds (VOCs) such as liquefied petroleum gas (LPG) for fire alarms; smoke detectors, hazardous toxic waste monitors.

b. <u>Environmental protection</u>: Air quality analysis based on pollutants from sources like industrial and automobile effluents; detectors for chlorofluorocarbons (CFC) and greenhouse gases for climate change studies.

c.   <u>Food-processing zones</u>: Aroma sensors during baking, roasting processes, freshness monitors.

d.   <u>National security and defense</u>: Detection of chemical and biological warfare agents such as phosgene, chlorine, sarin, tabun etc.

e.   <u>Medical diagnostics</u>: Non-invasive sampling or breath-analysis for treatment of diseases such as diabetes, and gastro-intestinal disorders; alcohol level analyzers (breathalyzers to detect drunk driving).

f.   <u>Aerospace applications</u>: Hydrogen leak detectors, sensors for oxygen, NO_x, VOCs.

1.3.2 Historical Background

A chemical gas sensor may be defined as a device that undergoes a change in its physical properties (e.g. conductance, capacitance, mass) upon exposure to a chemical vapor or a mixture of vapors (analytes) in a way that can be measured and quantified. Technically, all chemical gas sensors are transducer-type devices providing an indirect means of detecting, identifying and measuring gases through electrical or optical signals. The human body has its own gas sensor setup for identification of gases or odors, commonly referred to as the olfactory system wherein receptor neurons within the human nose convey corresponding electrical signals to the brain. While the human nose has the capability of smelling and differentiating between several hundreds of odors, it fails to detect extremely low concentrations of certain gases as well as odorless gases, which necessitate the development of chemical gas sensors that fulfill these requirements.

Historically, research and development in chemical gas sensors began in the 1950s in primarily uncoordinated, independent efforts. Walter Brattain, the Nobel Prize winning physicist at Bell Labs, reported one of the earliest observations of the changes in conductance of a semiconductor due to changes in the composition of surrounding gases.[8] Seiyama and co-workers realized the prospect of building a working gas sensor based on this principle in 1962, with polycrystalline zinc oxide layers sandwiched between metal electrodes.[9] Taguchi successfully built a commercial tin oxide based gas sensor in 1968 that is still very popular, marketed by Figaro Inc.[10-11] Other than semiconductor based sensors, catalytic bead sensors for detection of combustible gases have also been in use for over 50 years. Originally used for monitoring gases in coalmines, these sensors typically employed metals exhibiting excellent catalytic properties such as platinum and palladium. Since 1970, there have been several thousands of research articles published on novel sensing techniques as well as development of technologically advanced sensing systems for a wide range of applications.[12]

1.3.3 Classifications

Chemical gas sensors may be broadly classified based on operating principles into solid-state, catalytic-bead, electrochemical, infrared, and piezo-electric sensors.[13] Solid-state gas sensors typically comprise of a semiconducting material deployed on a heated substrate between two metallic electrodes, detecting gases based on surface reactions of gas molecules on the semiconductor surface. Catalytic-bead sensors employ a catalytic

surface maintained at high temperatures around a temperature sensor, wherein rapid combustion of flammable gas molecules on the catalyst surface result in noticeable temperature changes. Electrochemical sensors include a sensing electrode and a counter electrode immersed in an electrolyte, where reactions of gas molecules with the sensing electrode result in a change in the measured current between the electrodes. Infrared (IR) sensors use IR radiation to thermally excite gas molecules and differentiate between gases based on their absorption spectra. Sensors based on the piezo-electric effect, such as surface acoustic wave (SAW) and quartz crystal monitors (QCM) undergo a change in surface mechanical oscillation frequency upon interaction with gases.

Each type of sensor has its own set of advantages and limitations and is normally selected depending on the type of application. For example, solid-state sensors are widely used for domestic and industrial safety; catalytic-bead sensors in high temperature, harsh environments; electrochemical sensors for toxic gas detection; IR detectors for volatile organic compounds; SAW devices for chemical warfare agents, and hazardous chemical vapors etc. Since this thesis work is focused on the synthesis of novel solid-state metal oxide gas sensors, a detailed description on their design, sensing mechanism, advantages and applications will be developed in the following sub-sections.

1.3.4 Solid-state Gas Sensors

Among the different kinds of sensors available in the market, solid-state gas sensors are the most popular owing to their excellent sensitivity, versatility, vast range of detection, reliability, rugged construction and low cost.[14] Semiconducting metal oxides

such as tin oxide (SnO_2), titanium oxide (TiO_2), zinc oxide (ZnO), tungsten oxide (WO_3), and indium oxide (In_2O_3) are widely preferred materials for the sensing element since they present an opportunity for surface reactions involving molecular chemistry with a wide range of gases, the electrical consequences of which are manifested through a considerable volume of the material. The effectiveness of these sensors is governed not only by the electronic properties of the material but also on the available surface area for reaction, existence of stable sub-stoichiometric states, catalytic properties as well as temperature of operation.[14]

1.3.5 Physics of Conductometric Gas Sensing

Even though it has been known for a very long time that adsorption and desorption of gas molecules on and from the surface of a metal oxide semiconductor causes a change in its electrical conductance, the exact gas sensing mechanism is yet to be fully understood. The fundamental operational scheme for a conductometric gas sensor may be summarized as follows: on the surface of a wide bandgap semiconducting metal oxide, there exists a certain finite density of electron donors or acceptors; adsorption of gas molecules from the surrounding medium (usually air) result in an electronic charge transfer from the semiconductor forming ionized oxygen adsorbates such as O^- and O^{2-}. Thus a negative charge is generated on the surface leading to a depletion region or space charge layer close to the surface, reducing the conductance of the semiconductor. When this surface is exposed to a gas or gas mixture that interacts with the pre-adsorbed oxygen ions, the conductivity of the space charge region is modulated which is correspondingly measured as an electrical signal.[12, 15-17]

The adsorption of oxygen molecules on the sensing surface is either through physisorption or chemisorption depending on the temperature. Physisorption normally occurs at temperatures below 100 °C (e.g. room temperature), with weak binding between the molecules and the semiconductor held together by van der Waal forces. Typically, metal-oxide gas sensors are operated at temperatures above 250 °C in order to achieve reasonable signal to noise ratios. At these operating temperatures, chemisorption is the dominating adsorption process wherein the oxygen molecules are connected via dipole bonding to the semiconductor surface and form chemical bonds after electronic charge transfer. The usual active sites for chemisorption include normal sites, adatoms, dislocations, grain boundaries or impurity atoms etc. A schematic diagram of a semiconducting metal oxide surface after adsorption of oxygen molecules from the surrounding medium is shown in Figure 1.1.
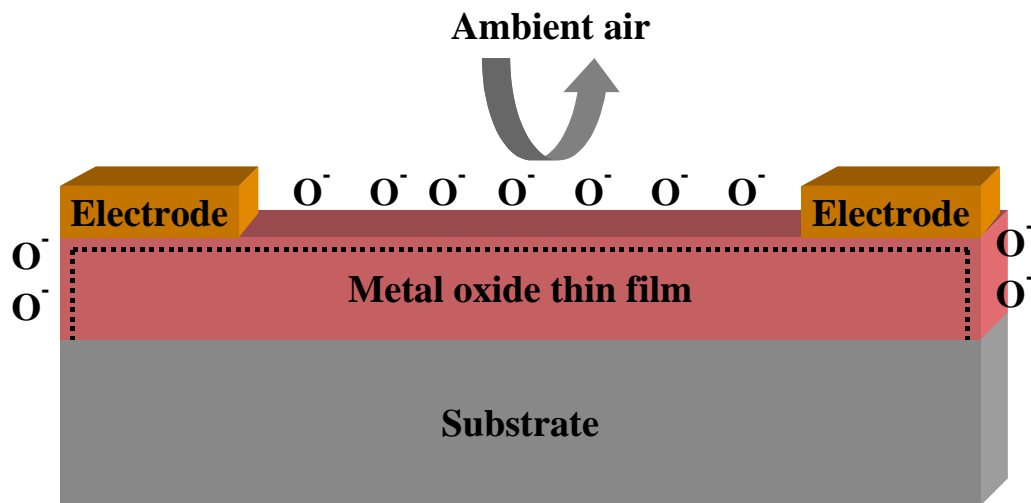
Figure 1.1 – Schematic view of the semiconducting metal oxide surface with pre-adsorbed oxygen ions upon exposure to ambient air. The dotted line represents the space-charge layer formed close to the surface where the semiconductor is depleted of electrons.

Upon exposure of the sensing surface to reducing or oxidizing gases, the measured surface conductance between electrodes is correspondingly modulated, the former causing an increase and the latter causing a decrease in conductance. The interaction of a reducing gas with the sensing surface may be expressed as follows:

$$R + O^- \rightarrow RO + e^-$$
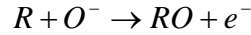
Reducing agents such as hydrogen (H_2), methanol (CH_3OH), carbon monoxide (CO) etc. tend to reduce the adsorbed oxygen on the sensing surface during which process, electronic charge carriers are replaced within the conduction band of the semiconductor leading to increased conductance, while the reaction products desorb from the surface. Chemical reactions corresponding to these processes are detailed below:

$$H_2 + O^- \rightarrow H_2O + e^-$$

$$CH_3OH + O^- \rightarrow HCHO + H_2O + e^-$$
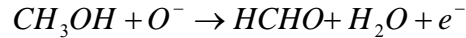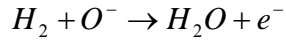
Oxidizing gases such as nitrous oxide (NO/NO_2), ozone (O_3) etc. on the other hand lead to a decrease in sensor conductance on reaction with surface-adsorbed oxygen. The chemical reactions representative of this interaction are shown below:

$$NO + O_2^- + e^- \rightarrow NO_2^- + O^-$$

$$NO_2 + e^- \rightarrow NO_2^-$$

$$NO_2 + O_2^- + 2e^- \rightarrow NO_2^- + 2O^-$$
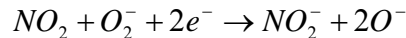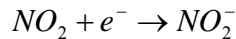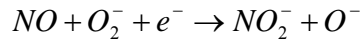
Generally, given a constant partial pressure of oxygen in the surrounding medium, the conductivity change in the semiconductor is in accordance with the concentration of the

test gas species (analyte). A more detailed description on the physical effects of these adsorption/desorption processes on the metal oxide surface including surface band bending, space-charge region buildup, Fermi-level pinning upon equilibration, and calculations of excess charge carrier densities may be found elsewhere.[15-16] At this point, it is important to point out that the surface conductance and not bulk conductance values are modulated and measured as electrical signals, hence it is advantageous to have sensing films as thin and porous as possible. A schematic view of the physics of gas-sensing including reception, transduction and measurement schemes for a typical solid-state gas sensor are shown in Figure 1.2.[18]
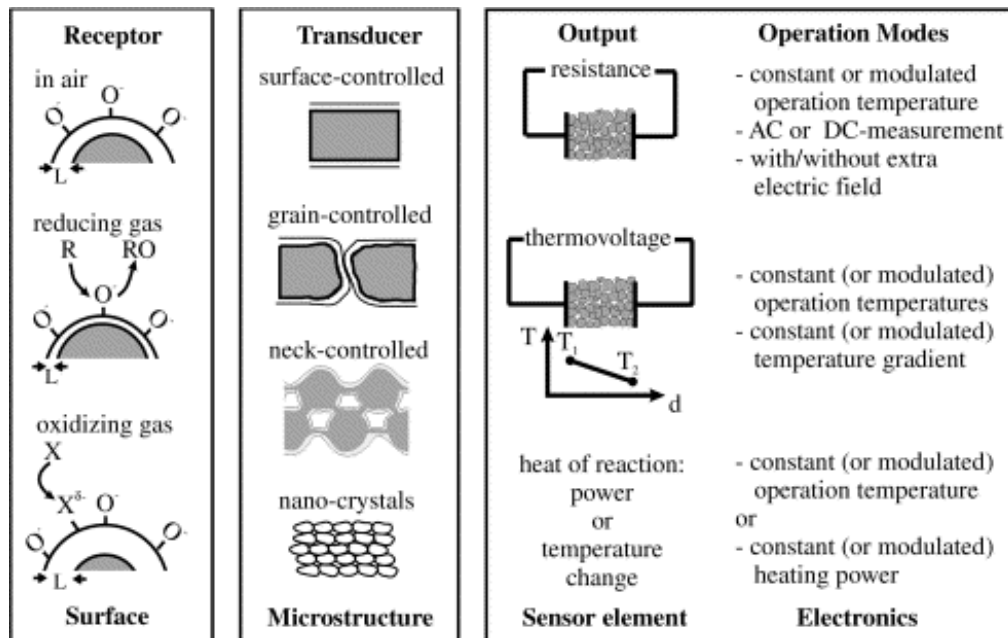
Figure 1.2 – Schematic view of the physics of chemical gas-sensing devices. Reproduced from Ref [18].

1.3.6 Desirable Sensor Characteristics

The main parameters that are often cited to be the most desirable characteristics a sensor should possess are:

a. Sensitivity: Good signal to noise ratio for very low concentrations of analytes.

b. Selectivity: Ability to differentiate between different analytes.

c. Stability: Reproducible signals with minimal fatigue upon continuous operation for long periods of time.

d. Speed of response: Rapid detection of changes in surrounding environment.

Apart from these properties, commercial sensors also need to be cost-effective, reliable and operate with minimal power drain. Unfortunately, creating a sensor that satisfies all these requirements adequately has not yet been realized. A rational step in the right direction towards realizing an ideal sensor is described in the next sub-section.

1.3.7 Electronic Noses

There is a burgeoning interest in developing arrays of solid-state gas sensors coupled with pattern-recognition algorithms, commonly referred to as "electronic noses" or e-noses.[19-22] The purpose of creating an e-nose is to effectively differentiate between gases in a complex gas mixture or odor and analyze the chemical makeup of the odor. This is particularly important for solid-state gas sensors, which generally have excellent sensitivity, stability and speed but poor selectivity. The e-nose gets its name from the fact that the arrangement involved mimics a human or animal olfactory system, i.e. it consists of multiple receptors that respond differently to various odors and the overall assimilation

of these responses through a pattern-recognition system analogous to a brain, is used for odor identification.

Amongst the various metal oxide sensor materials, SnO_2 has received far more research attention than others since Taguchi built and marketed the first commercial SnO_2-based sensor, because of its high reactivity to many gaseous species.[10] However due to its lack of selectivity, investigation of other metal oxides has been necessary in an effort to build an effective e-nose. A digital photograph and a schematic diagram of a Taguchi sensor marketed by Figaro Inc. are shown in Figure 1.3.[11]
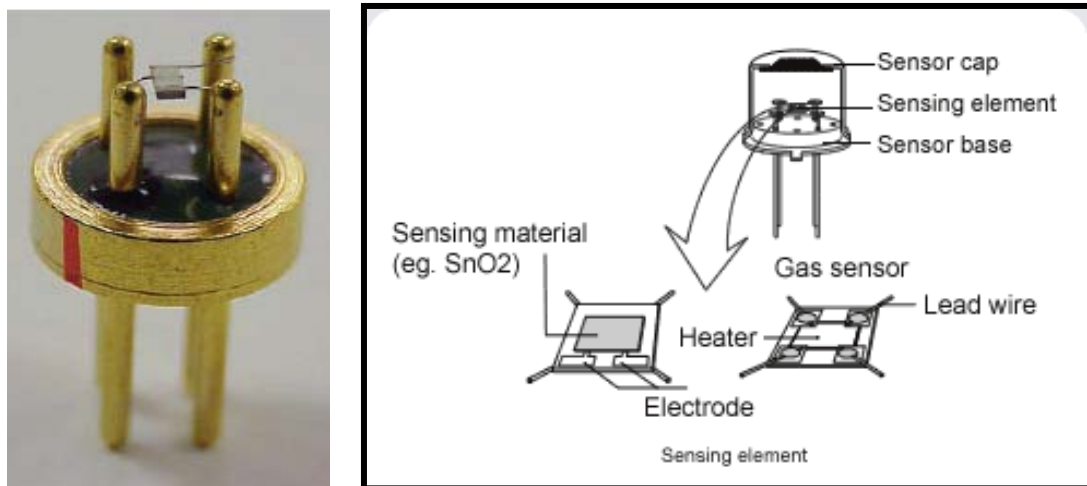
Figure 1.3 – Digital photograph and schematic view of the components of a commercial Taguchi sensor. Reproduced from Ref [11].

1.3.8 Importance of Nanotechnology in Sensor Research

The key areas of current solid-state sensor research include the development of sensing platforms with improved sensing capabilities, size-reduction of devices to enable low-power consumption and affordability, as well as improving data analysis methods to accurately identify analytes. The importance of incorporating nanostructures into sensing elements is multiple fold; their incredibly high surface to volume ratios provide enhanced surface areas for interaction with gases, their unique electronic properties enable rapid detectable signal changes, their extremely small sizes allows them to be integrated into miniature devices that can be operated at low powers.[18,23] Several kinds of nanostructures of various materials have been studied for gas sensing applications including nanocrystalline thin films, nanoparticle films, porous membranes, one-dimensional structures such as nanowires and carbon nanotubes, nanobelts, nano-shells etc. and observed to possess superior sensing characteristics than existing thick film sensors.[24-30]

1.4 Structure of this Investigation

The purpose of this doctoral thesis work is in examining the possibilities of improving sensing characteristics of metal oxides using one-dimensional (1-D) nanostructures. Different approaches have been undertaken in synthesizing these nanostructures, some of which were original ideas developed during the course of persistent experimentation. The three primary materials studied were SnO_2, WO_3 and ZnO. In spite of an enormous amount of literature devoted to the creation of 1-D nanostructures of these materials, there has been a surprising lack of methods describing the direct integration of these nanostructures into miniature gas sensing devices. Hence, the synthesis methods utilized

in this work were developed with the objective of non-destructively integrating as-grown 1-D nanostructures into functional microscale chemical gas sensing devices. Excellent reviews on the current state of 1-D nanostructure research including synthesis and applications may be found in Refs. [31-33].

The focus of chapter 2 is on the synthesis of SnO_2 nanotubes using carbon nanotubes as removable templates on micromachined platforms called microhotplates. Two contrasting approaches have been undertaken in directly synthesizing carbon nanotubes on microhotplates. In the course of process development, two significant challenges have been overcome, the first involving carbon nanotube growth on metallic surfaces using a novel, bi-metallic catalyst and the second concerning the direct growth of high density carbon nanotube arrays on microhotplates. SnO_2 nanotubes have been generated subsequently, using the carbon nanotubes as easily removable templates. The gas sensing characteristics of the SnO_2 nanotubes has been evaluated and compared with SnO_2 thin films. The synthesis process described in this chapter can be extended to create nanotubes of any metal oxide.

Chapter 3 deals with the synthesis of WO_x nanowires through a direct thermal reconstruction of tungsten thin films heat-treated in the presence of an RF plasma. The nanowire synthesis technique, which is based on an existing process, has been modified to considerably reduce the processing temperature in order to achieve direct growth of nanowires on a microhotplate. In addition to nanowires, unusual hollow square shaped structures called microducts have also been grown under certain specific process

conditions. The growth mechanisms, influence of operational parameters on nanostructure evolution, advantages of using WO$_3$ nanowires over thin films in gas-sensing devices, as well as other potential applications of nanowires have been elucidated.

Chapter 4 concerns synthesis of ZnO nanowire arrays on a variety of different substrates at low temperatures and the development of a unique, non-destructive approach to achieving electrical contacts to the nanowire arrays using nanoparticle films. The extremely high aspect ratios of the nanowires has been exploited by employing the nanowire tips as electric field concentrators, to selectively deposit conductive nanoparticles on top of the nanowire array and using the nanoparticle film as a top contact. A highly sensitive gas-sensing device has been conceived and successfully fabricated using this approach. The approach described is universally applicable and has several interesting implications in the design of future nanoelectronic and photonic devices.

Chapter 5 offers a brief summary of the various synthesis and integration approaches developed during this doctoral thesis work and concluding comments on the future of scientific research involving 1-D nanostructures. Discussions on avenues for future research, working principles of various characterization techniques, and simple nanostructure synthesis procedure steps may be found in the appendices.

Chapter 2

Tin Oxide Nanotubes

2.1 Carbon Nanotubes

2.1.1 Introduction to Carbon Nanotubes

Since the original report of their discovery in 1991, carbon nanotubes (CNTs) have been the subject of immense research.[34] They may be thought of as graphitic sheets with a hexagonal lattice that have been wrapped up into a seamless cylinder (Figure 2.1).[35] Two common types of carbon nanotubes are cited in literature, single and multi-walled nanotubes depending on the number of graphene sheets wrapped into the cylindrical structure, each having distinct properties.
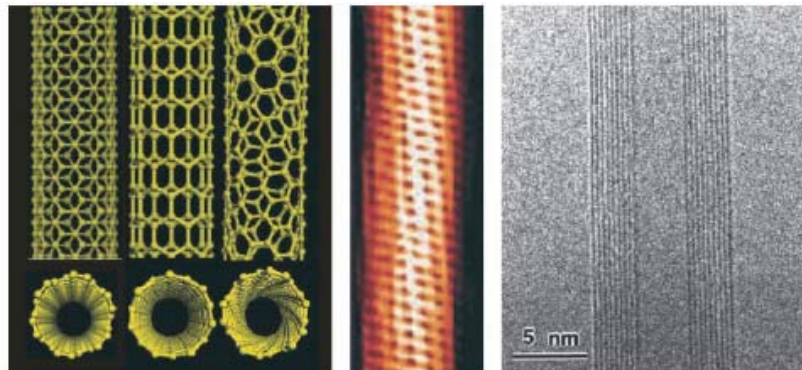
Figure 2.1 – Schematic diagram of graphitic sheet structure of carbon nanotubes and a transmission electron microscope image of a multi-walled nanotube. Reproduced from Ref. [35].

Carbon nanotubes have several peculiar physical, chemical, electronic and optical properties, which may be exploited in myriad applications including field-emission devices, field-effect transistors (FETs), electrical interconnects for silicon technology,

fillers for conductive plastics, fibers and fabrics, catalyst support, energy storage, chemical and bio-sensors etc.[36-45] Their extremely small diameters (few nanometers) and long lengths (few micrometers up to few centimeters possible) give them enormously high aspect ratios which are exploited in several of these applications.[46] Comprehensive information on the theoretical aspects of CNT structure and the influence of nearly one-dimensional structure on their unique properties may be found in Refs. [47-48].

2.1.2 Growth Mechanism

The exact growth mechanism of CNTs is still not fully understood. Generally, the controlled synthesis of CNTs through thermal CVD processes requires transition metal catalyst nanoparticles (e.g. iron, nickel, or cobalt), a carbon feedstock (e.g. hydrocarbons, alcohols, or carbon monoxide) and a heat source. The most commonly accepted mechanism, proposed by Baker et al. in the early 1970s, involves catalytic decomposition of the carbon precursor and bulk diffusion of carbon.[49] According to this mechanism, the carbon precursor undergoes thermal decomposition on the catalyst surface releasing hydrogen and carbon, which dissolve into, diffuse and precipitate out of the particle. However, instead of bulk diffusion, another growth model based on the surface diffusion of carbon around the metal particle to form a tubular structure is agreed upon as a more applicable mechanism. Two different growth modes, depending on the adherence of the catalyst particle with the substrate or support have been observed, called root and tip growths as shown in Figure 2.2.[50]
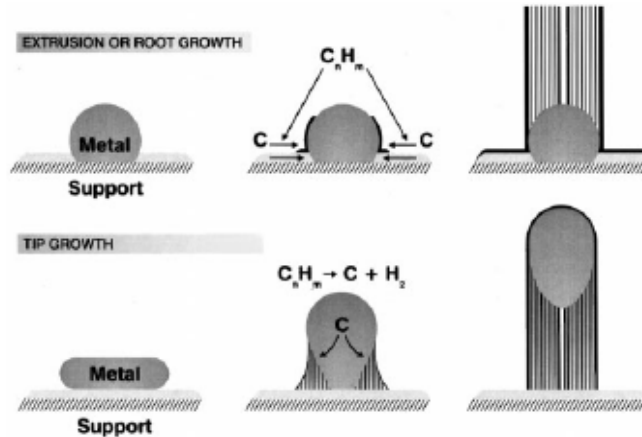
Figure 2.2 – Root and tip growth modes for carbon nanotubes. Reproduced from Ref. [50].

2.1.3 Growth Techniques

There are several different synthesis techniques for the growth of CNTs including arc discharge, laser ablation, CVD, flame synthesis etc. Amongst these techniques, CVD is one of the most popular and versatile processes allowing systematic process control. Different types of CVD processes have been employed for CNT growth including thermal CVD, plasma enhanced CVD etc. using a variety of different precursors (e.g. methane, ethylene, acetylene) over a wide range of temperatures (600 to 1200 °C) resulting in both single and multi-walled nanotubes. A typical thermal CVD process for CNT growth involves deposition of catalyst particles on a substrate which is then placed within a furnace equipped with gas inlet lines delivering dilute concentrations of carbon precursors in carrier gases (such as argon or nitrogen, along with hydrogen).

2.1.4 Carbon Nanotubes as Templates

Like CNTs, inorganic nanotubes and nanoparticles have also attracted intense scientific attention owing to their interesting electronic and mechanical properties.[51-54] CNTs themselves have been utilized as templates for the creation of a variety of inorganic nanostructures such as nanotubes of SiO_2, Al_2O_3, V_2O_5, MoO_3, ZrO_2, Fe_2O_3 as well as nanorods of Si_3N_4, Si_2N_2O, and SiC.[55-61] One of the biggest advantages of using this templated approach is that it is very useful in synthesis of one-dimensional nanostructures of refractory materials such as metal oxides and nitrides, which would otherwise necessitate very high process temperatures.

2.2 Microhotplates

Giant strides in silicon based micro-electromechanical systems (MEMS) technology over the last decade have made the design of nanoscale sensors and actuators possible. A microhotplate is one such micro-machined platform that was designed and fabricated as a first step towards the creation of miniature chemical gas-sensing devices. Briefly, each microhotplate is a multi-layer structure (lateral dimensions $\approx$ 200 μm) consisting of a buried polycrystalline silicon heater, a metallic heat-distribution plate and metal contact pads, each layer being separated by insulating films of silicon dioxide.[62-63] This arrangement allows very fast heating cycles and low power consumptions. Images of a typical 9-element package, individual microhotplates and a cross-sectional view of the heater and electrode assembly are shown in Figure 2.3.

19
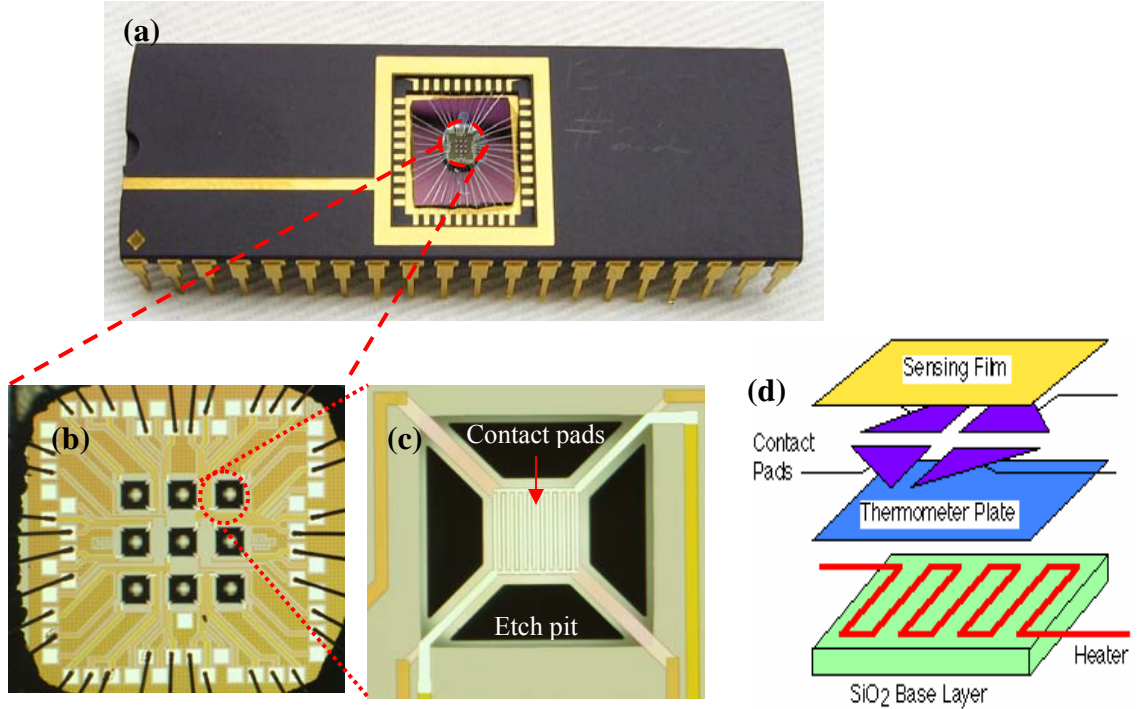
Figure 2.3 – (a) Digital photograph of a package containing a 9-element array of microhotplates; (b), (c) Optical micrographs of microhotplates; (d) Multi-layered structure of an individual microhotplate device

Microhotplates can be fabricated as arrays on a single chip through a commercial CMOS (complementary metal oxide semiconductor) process, and since each element can be individually controlled by a micro-heater, localized heating of specific elements on the same chip can be achieved. Microhotplates also possess very low thermal response times (~ 0.6 ms) and consume very little power (thermal efficiency in air ~ 8 °C/mW). The variation in conductance of the sensing film is monitored using contact electrodes during gas sensing measurements. Since several different film microstructures may be grown on different elements on the same array, the responses from all of these elements can be monitored and studied simultaneously, in the presence of test gases. Sensing kinetics can also be controlled through rapid thermal modulation of each element. Microhotplates may

have different designs for contact electrodes (square pads, interdigitated comb-like pads etc.) and packages containing 4, 9, 16, 27, 36, and 48-element arrays of hotplates on a single chip have been demonstrated. One of the limitations of growing sensing films on a microhotplate is that the growth temperature cannot exceed 620 °C for stable operation of the device owing to the presence of the aluminum heat distribution layer. A detailed description of microhotplate fabrication procedures, sensor designs and applications may be found Refs. [64-68].

2.3 Overall Process Description

In this work, we were particularly interested in creating metal oxide nanotubes (e.g. tin oxide) using CNTs as templates. Usually, as-grown CNTs at temperatures below 650 °C tend to be multi-walled, metallic in nature and relatively inert to changes in surrounding gas medium. However, their extremely high aspect ratios may be exploited to create a very high surface area metal oxide simply by coating the nanotubes. They are also easily removed through thermal annealing in air and hence provide an ideal template for growing metal oxide nanotubes. The generation of this nanostructure can be expected to have better sensor characteristics than a thin film owing to the very high surface area of nanotubes for interaction with gases.

The first approach undertaken towards growing CNTs on microhotplates is explained in the next section.

2.4 Carbon Nanotube Synthesis – First Approach

2.4.1 Nickel Catalyst Nanoparticle Deposition

Among the numerous nanoparticle generation techniques described in literature, we employed laser ablation as a convenient way of generating nanoparticles and their aggregates. A Nd-YAG laser beam (1064 nm) was focused on an ultra-pure Ni target (Kurt J. Lesker Co., 1" dia, 0.125" thick) with nitrogen (N_2) as carrier gas. The purity of the generated particles in this technique depends entirely on the purity of the carrier gas and the target material. Upon impingement, the laser beam evaporates material from the target material into the surrounding gas, where it is rapidly cooled, allowing homogenous nucleation and growth of nanoparticles. The generated nanoparticles were size-selected based on their electrical mobility in a differential mobility analyzer (DMA), then sintered at 1100 °C to reshape them into uniform spheres, and charged positively using a unipolar charger. These charged particles were transported into the deposition chamber containing the microhotplate assembly. A high voltage ($\approx$ 1-2 kV) was applied between the hotplates and the aerosol inlet carrying the particles, in order to create an electric field conducive for the deposition of charged nanoparticles onto the microhotplates. A schematic diagram of the entire process of nanoparticle generation and deposition is shown in Figure 2.4.
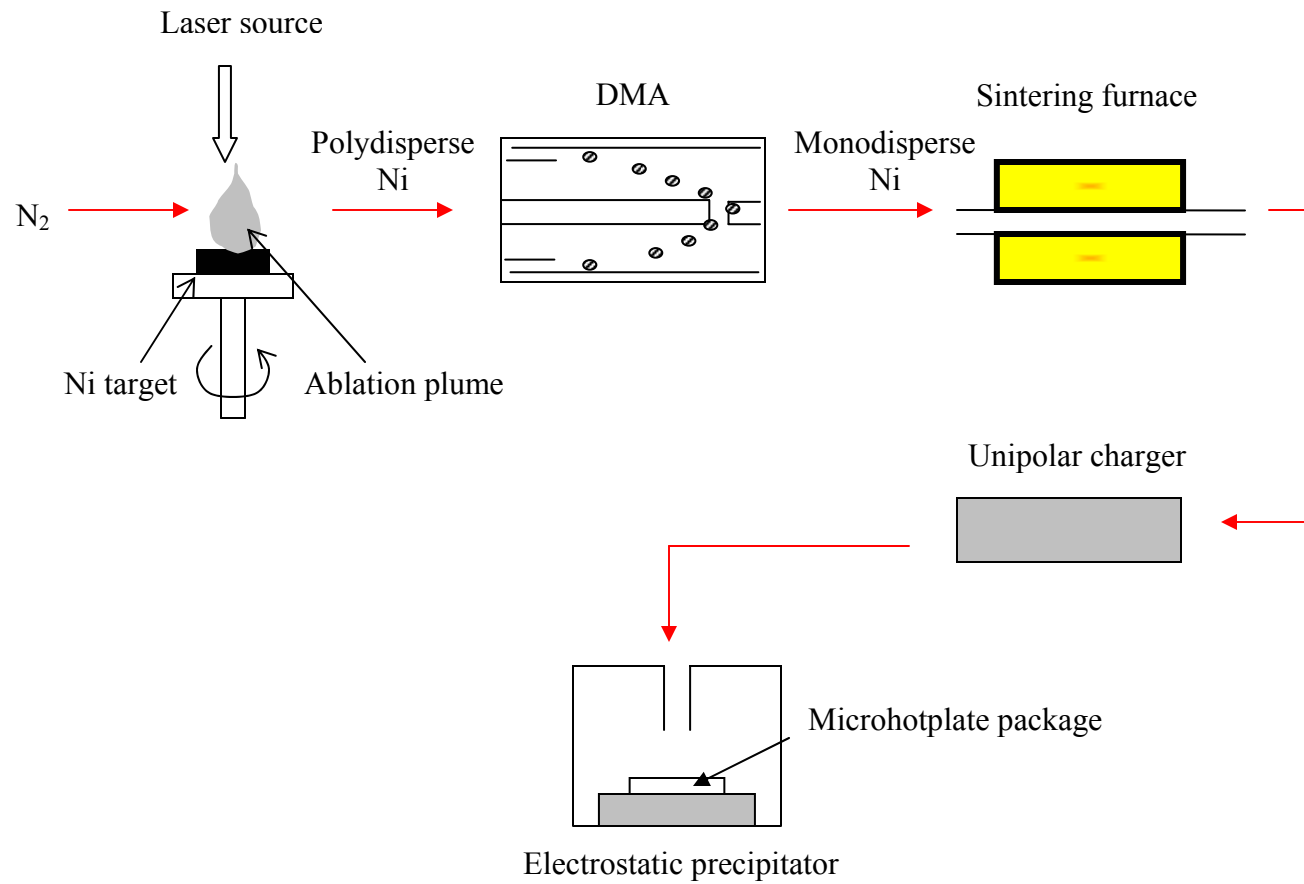
Figure 2.4 – Schematic diagram of Ni nanoparticle generation and deposition

2.4.2 Carbon Nanotube Growth and Characterization

After nanoparticle deposition, the microhotplate array was transferred to a low-pressure CVD system, for the growth of CNTs. The chamber was evacuated using a rotary mechanical rough pump, and then argon (Ar) and hydrogen (H_2) were introduced at mass flow rates of 150 sccm (standard cubic centimeters per minute) and 30 sccm respectively. The Ni was then annealed in this Ar/H_2 flow at 600 °C, at a chamber pressure of 4 torr, for about 10 minutes. This was done to remove any oxide layer that might have formed on the particles during generation and deposition. After this pre-treatment, the micro-heater was turned off and the hydrocarbon precursor acetylene (C_2H_2) was introduced into the chamber with a flow rate of 20 sccm. A throttle valve connecting the chamber to the rough pump was then completely closed to bring the chamber pressure up to 1 atmosphere, under the flow of Ar, H_2 and C_2H_2. The microhotplates were once again heated to 550-600 °C, and CNTs were grown for ≈10 minutes. SEM images of 30 nm sized Ni nanoparticles and corresponding CNTs grown on a microhotplate are shown in Figure 2.5. It is worth mentioning that unlike the conventional CVD of CNTs within tube furnaces maintained at temperatures above 600 °C, the CNTs grown here were driven primarily by a buried micro-heater without any pre-heating of the precursor gases. The CNTs were observed to have diameters between 30 and 50 nm, and lengths between 1 and 4 μm. At these diameter scales, the nanotubes were generally multi-walled.
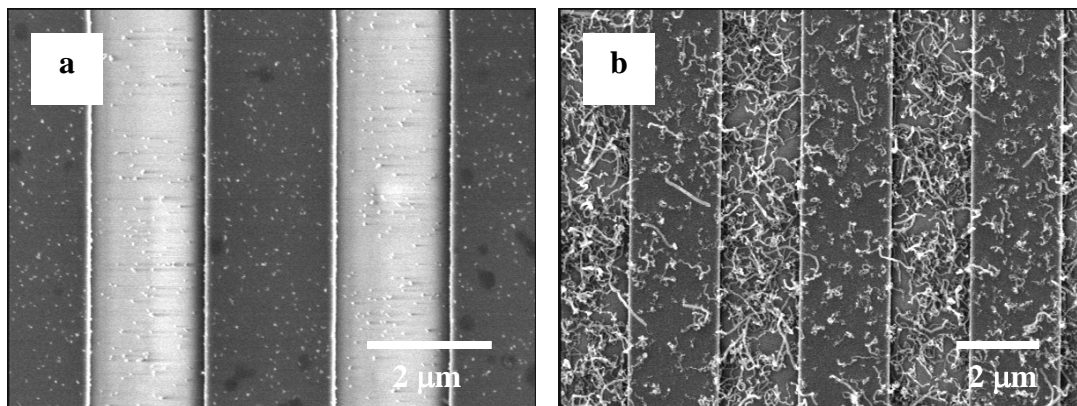
Figure 2.5 – SEM images of microhotplate surface following (a) 30 nm sized Ni nanoparticle deposition; (b) carbon nanotube growth

2.4.3 Tin Oxide Thin Film Deposition

The growth of tin oxide (SnO_2) through a CVD process followed the growth of CNTs on the microhotplates. The hotplates were placed within a CVD chamber and the system was pumped down to an ultimate pressure of $\approx 10^{-6}$ torr using a turbo pump and brought up back to about 150 millitorr under a flow of Ar. The hotplates were then exposed to a flow of tin nitrate $Sn(NO_3)_4$ for about 10 minutes to allow equilibration of gas flows within the chamber. Specific elements on the microhotplate array were then heated to 375 °C, for exposure times varying between 10-20 seconds. The flow of tin nitrate was then shut off and the gases were pumped out for another hour to completely remove all reactants, before the chamber was brought up to atmospheric pressure in Ar. The microhotplate surfaces were examined under the SEM, normally on the same region of the hotplate before and after SnO_2 deposition to examine the extent of coating, which can be seen in Figure 2.6. It was clearly visible that SnO_2 deposited both on the nanotubes as

well as the hotplate surface underneath, and the thickness of the coating could be manipulated based on growth time.
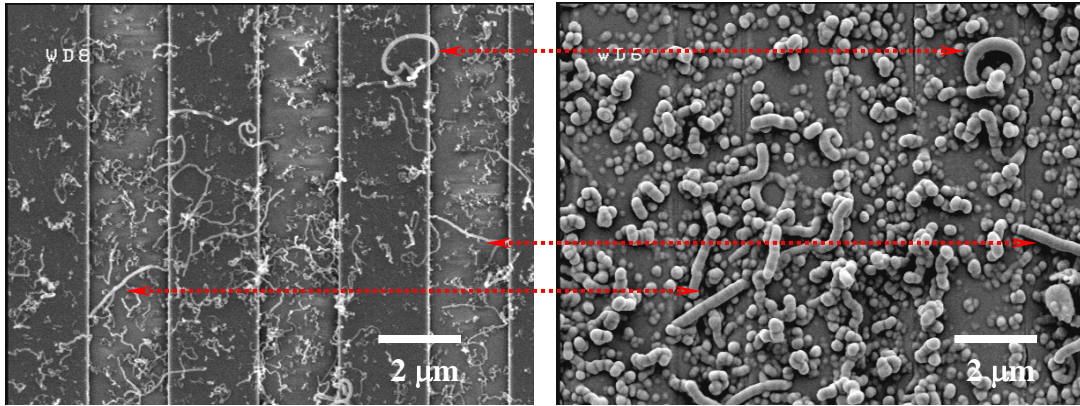
Figure 2.6 – SEM images of microhotplate surface before and after SnO_2 deposition. The arrows indicate specific shapes on the surface that were imaged to verify conformal coating.

2.4.4 Disadvantages of this Approach

Even though the approach of growing CNTs from nanoparticles deposited from the vapor phase was effective, it resulted in very low coverage of nanotubes between sensor pads and hence the difference in sensing behaviors between a SnO_2 nanotube coated hotplate and a SnO_2 thin film coated hotplate was not appreciable. Hence at this stage, a need arose to design an effective way of achieving high-density CNT growth directly on microhotplates at temperatures suitable for device operation (below 625 °C).

2.5 Carbon Nanotube Array Synthesis – Second Approach

2.5.1 Technical Challenges

Previously, growth of CNTs has been largely confined to non-conductive substrates owing to significant catalyst-metal interactions restricting availability of catalytic particles for CNT nucleation. Several groups have demonstrated the growth of aligned CNT arrays on silicon (Si) wafers either through sputtering or micro-contact printing of catalyst layers followed by CVD.[69-70] Ng et al. investigated the effects of several catalysts and underlayers deposited on Si wafers and observed that iron/nickel (Fe/Ni) and Ni catalysts on aluminum (Al) underlayers gave rise to aligned, oriented CNTs.[71] Wang and co-workers reported on the growth of aligned CNTs on metal sheets of Ni, titanium (Ti), tantalum (Ta) and Al-coated Si through pyrolysis of iron phthalocyanine at 950 °C.[72] However, this process was unsuccessful in growing CNTs on gold (Au), copper (Cu) or nichrome (Ni-Cr). Very recently, Talapatra and co-workers reported on the direct growth of aligned CNT arrays on a metal alloy, Inconel through a vapor-phase floating-catalyst CVD process but this technique is not suitable for direct growth of CNT arrays on metals such as Si or Au.[73]

2.5.2 Bi-metallic Catalyst

In this work, we developed a generic CVD process for the direct growth of well-aligned CNT arrays at low growth temperatures (550 °C to 700 °C) using a bimetallic iron/alumina (Fe/Al_2O_3) composite catalyst on a range of conductive substrates such as

pure metals, metal alloys and ceramics. The addition of non-catalytic Al_2O_3 to the catalytic Fe was crucial in enabling high-density aligned CNT growth without catalyst alloying or poisoning. Very recently, the aerosol form of this composite catalyst was employed as a means of generating hybrid nanoparticle-CNT structures resembling sea urchins.[74] Our approach was to design an optimal process of growing CNTs on macro-scale metallic substrates, with the intention of successfully reproducing the growth process on microhotplates later.

2.5.3 Experimental Details

Several commonly used metals such as highly doped Si, Au, Ag, Cu, Al, tungsten (W), and platinum (Pt), as well as metal alloys such as titanium nitride (TiN), nichrome (Ni-Cr) and steel were considered as substrates for the growth of aligned CNT arrays in our work. The metal films were either sputtered or evaporated (typically 100 nm thick) onto silicon dioxide (SiO_2) wafers except for W (TEM grids) and steel (hot-rolled steel plate). All substrates were ultrasonically cleaned in ethanol before CNT growth. The chemicals used for preparing catalyst solutions were acquired from a commercial vendor (Sigma-Aldrich).

A 10 mmol/L aqueous solution containing equal proportions of iron nitrate [$Fe(NO_3)_3.9H_2O$, ACS reagent, 98+%] and aluminum nitrate [$Al(NO_3)_3.9H_2O$, ACS reagent, 98+%] was prepared and employed as the catalyst solution for CNT growth. The solution was then applied onto the substrates using a micropipette and allowed to dry at

room temperature. The substrates were then loaded onto an alumina boat and placed within a gas flow reactor consisting of a 1" (2.54 cm) diameter quartz glass tube inside a temperature-controlled tube furnace. Under a steady gas flow rate of 200 sccm (standard cubic centimeters per minute) argon (Ar) and 45 sccm hydrogen (H_2), the furnace was heated to 600 °C. The substrates were typically annealed in this Ar-H_2 mixture for 10 min before the introduction of 5 sccm acetylene (C_2H_2) to begin CNT growth. CNTs were grown for 5 min, then the carbon precursor was shut off and the substrates were cooled down to room temperature in Ar.

2.5.4. Surface Morphology

All the metal substrates considered in this work except Pt allowed the nucleation and growth of CNTs. The results of CNT growth on various substrates have been listed in Table 2.1. SEM images of substrates of Si, Au, Ag, Cu, Al, Pt and W following CNT growth are shown in Figure 2.7. On Si, Au, Ag, Al and W, the CNT arrays were uniformly aligned along the substrate normal. A closer inspection of the arrays indicated that the CNTs were approximately 10nm to 20 nm in diameter and a few tens of micrometers in length. Even though individual CNTs seemed to be bent, the overall nanotube array structure exhibited excellent alignment, vertical to the substrate. In the case of Pt, the metal surface appeared to have swelled and restructured into platelets. On the other hand, nanotubes on Cu were highly non-uniform both with respect to diameter (10 nm to 75 nm) and lacked any orientation ('spaghetti'-like).

Remarkably, even on metal alloys and conductive ceramics such as TiN, NiCr and steel, our growth process resulted in well-aligned nanotube arrays wherever catalyst was dispersed (Figure 2.8). Upon further investigation, we found that even in areas where the Fe/Al_2O_3 catalyst was not applied, nanotubes as well as amorphous carbons and other carbon nanostructures appeared to have grown on the NiCr and steel substrates. The CNT arrays grown on steel were however very weakly adhered to the substrate and peeled off from the surface readily.

Table 2.1 – CNT growth characteristics on various metals and metal alloys

Substrate	CNT characteristics
Si	Uniform, well aligned
Au	Uniform, well aligned
Ag	Uniform, well aligned
Cu	Non-uniform, random growth
Al	Uniform, well aligned
Pt	No CNT growth
W	Uniform, well aligned
TiN	Uniform, well aligned
NiCr	Uniform, well aligned
Steel	Uniform, aligned, not well adhered
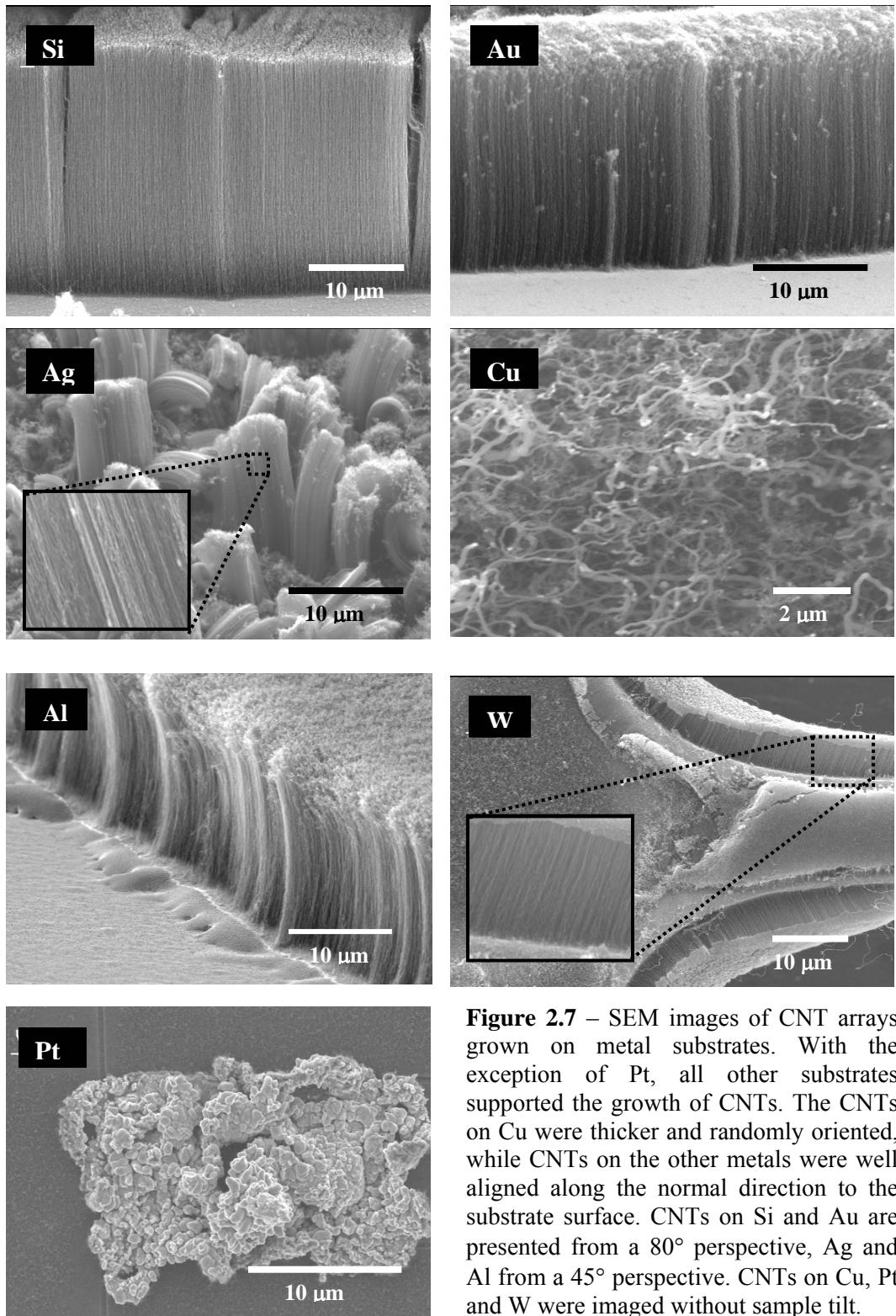
Figure 2.7 – SEM images of CNT arrays grown on metal substrates. With the exception of Pt, all other substrates supported the growth of CNTs. The CNTs on Cu were thicker and randomly oriented, while CNTs on the other metals were well aligned along the normal direction to the substrate surface. CNTs on Si and Au are presented from a 80° perspective, Ag and Al from a 45° perspective. CNTs on Cu, Pt and W were imaged without sample tilt.

31
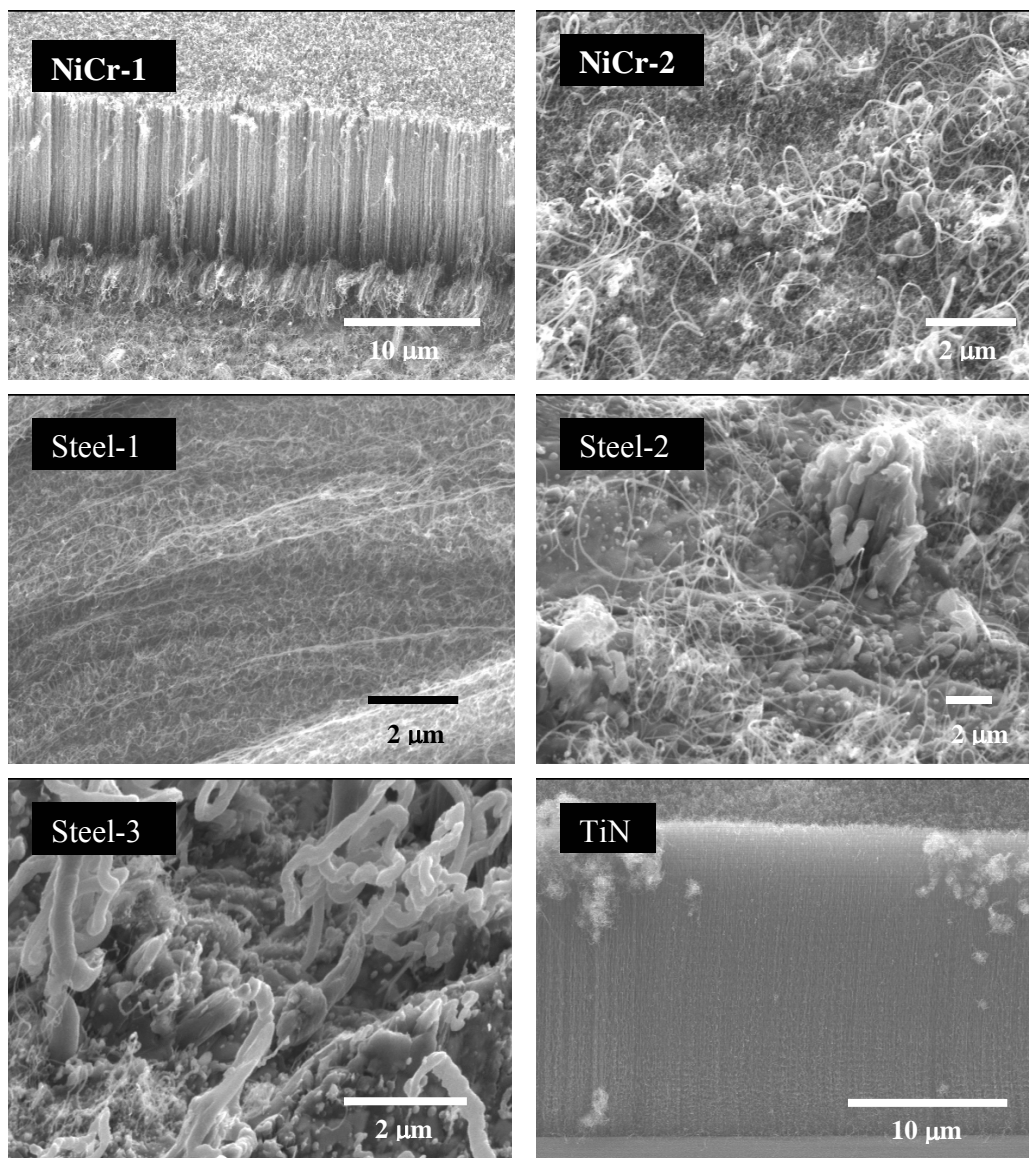
Figure 2.8 – SEM images of CNTs grown on metal alloys nichrome (NiCr) and steel, and a conductive ceramic (TiN). The CNTs were vertically aligned wherever catalyst was deposited (NiCr-1, Steel 1, TiN). NiCr-2, Steel-2 and Steel-3 are images of CNTs, fibers and amorphous deposits observed to grow in areas of NiCr and steel where the catalyst was not applied, due to the intrinsic presence of catalytic metals (Ni, Fe) on their surfaces. NiCr-1 and TiN are presented from an 80° perspective. NiCr-2, Steel-2 and Steel-3 are presented from a 45° perspective. Steel-1 represents a portion of the CNT array that peeled off from the substrate.

2.5.5 Structural Characterization

High-resolution TEM (HR-TEM) images of CNTs removed from an array grown on Au are shown in figure 2.9. An imaged 17 nm multi-walled CNT had $\approx$ 16 concentric graphene sheets wrapped around a hollow inner core of $\approx$ 5 nm diameter. An oblong catalyst particle could be found on a few of the CNTs suspended on the grid, indicative of tip-growth. We observed that CNTs grown on several other substrates also exhibited similar characteristics from our TEM analysis.
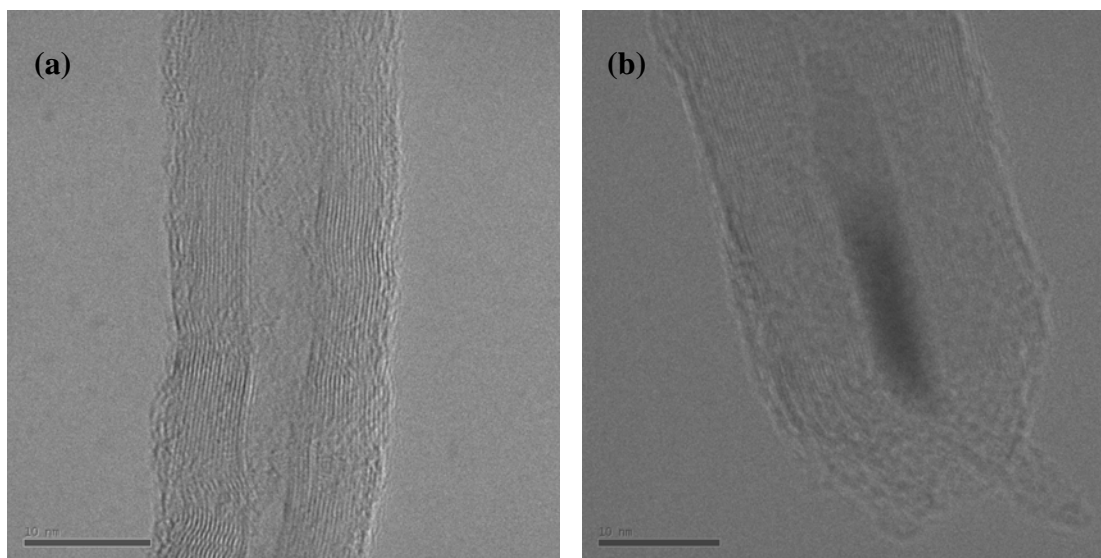
Figure 2.9 – High-resolution TEM images of a single multi-walled CNT (grown on Au) clearly represent highly crystalline graphene sheets overlapping a hollow core. An oblong catalyst particle could be found on the tips of a few CNTs. The scale bars represent 10 nm.

2.5.6 Growth Mechanism

We believe that addition of Al_2O_3 plays a crucial role in reducing Fe-substrate interactions (acting like a diffusion barrier), resulting in the formation of uniform Fe catalyst nanoparticles for CNT nucleation into well-aligned arrays. Both Fe and Al

nitrates undergo thermal decomposition into their respective oxides (Fe_2O_3 and Al_2O_3) above 250 °C.[75] Since the nitrates are well mixed at room temperature, well-distributed Fe_2O_3 particles in an Al_2O_3 matrix will be initially formed on the substrate. When this film is annealed in Ar-H_2 at 625 °C, the Fe_2O_3 is readily reduced to Fe while the Al_2O_3 remains quite stable in these conditions. During the CNT growth process, the carbon precursor C_2H_2 readily decomposes on the well-dispersed catalytic Fe particles confined within the non-catalytic Al_2O_3 matrix, resulting in the growth of well-aligned CNT arrays. The alignment of the CNTs may be explained based on the "crowding effect" and van der Waal interactions, with each CNT being supported by a neighboring CNT.[76]

2.5.7 Substrate Effects

The above-mentioned discussion is applicable to describe the growth of CNT arrays on most metal substrates. Pt however, is well known for its catalytic properties in the presence of H_2, which explains its failure to allow the nucleation of CNTs.[77] Even though the Pt film is covered entirely by the Fe-Al_2O_3 composite, the H_2 molecules tend to easily diffuse through the composite and interact with the Pt underneath, causing swelling and rendering the film unsuitable for CNT growth. We have observed that without the use of H_2 in our process, amorphous carbon tends to coat the catalyst surface following CVD of C_2H_2. In the case of Cu, we believe that the tendency of Cu to alloy with a lot of materials including both Al_2O_3 and Fe tends to hinder uniform catalyst particle nucleation resulting in more randomly oriented non-uniform CNTs with a wide size distribution.[78] The vertically aligned CNT arrays grown on the rest of the metal substrates (Si, Au, Ag, W, Al) had very similar morphologies. The CNTs on every individual array were of

uniform length with growth rates of ≈ 2 μm/min to 4 μm/min. Unlike the previous attempts to grow CNT arrays directly on metals, we do not expect the underlying metal layer to exert any significant influence on the CNT morphology or growth behavior as long as the metal does not alloy with Al_2O_3.[79-83]

The generic nature of our process was reflected by the successful growth of aligned CNT arrays even on commonly employed metal alloys and ceramics such as TiN, steel and nichrome. We also observed that steel and nichrome also catalyze a variety of carbon nanostructures including randomly oriented CNTs, fibers, and particles in areas not covered with our Fe/Al_2O_3 composite catalyst, due to the intrinsic presence of catalytic metals Fe and Ni on their surfaces. The growth results on all substrates were observed to be reproducible.

2.5.8 Parametric Study

The results from a parametric study on the influence of temperature and growth time on the CNT array length (on Au substrates) are shown in Figure 2.10. For growth temperature studies, CNT arrays were grown for 5 minutes each at temperatures between 550 and 750 °C. For temperatures below 550 °C, the samples were generally covered with amorphous carbon deposits. The array length was seen to increase until 650 °C and followed an opposing trend at higher temperatures. CNTs were not observed to grow beyond 750 °C possibly due to highly mobile metal underlayers interacting and alloying

35

with the catalyst particles at such high temperatures. The CNT growth resembled an Arrhenius-type reaction, with estimated activation energy of 1.41 eV.
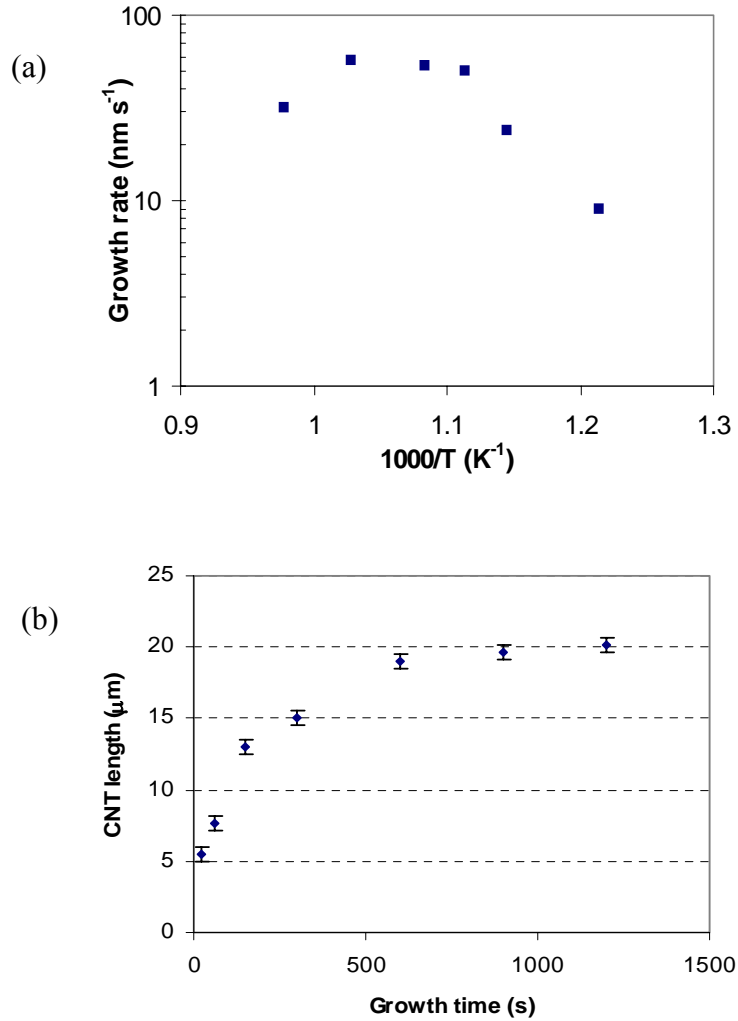
Figure 2.10 – Influence of growth temperature (a) and growth time (b) on CNT array lengths. Temperature for growth time study = 620 °C.

The dependence of CNT array length on growth time implied that the growth of CNTs was essentially complete after about 20 minutes of growth. The possible reason for such a

saturation-effect might be complete coating of catalyst particles by carbon following continued growth.

2.5.9 Contact Resistance Measurements

One of the key requirements for the electrical and electronic applications of CNTs such as interconnects, field emitters etc. is the need for a low metal-CNT contact resistance.[79-80] We measured the 2-pt resistance between the underlying metal and the top of the CNT array using a probe station (contact tip size ≈ 25 μm) and observed that the overall resistance inclusive of the contact resistance was under 400 Ω for several samples (Au, Si, Ag, Al). We further investigated the exact contact resistance for CNTs on Au using a combination of 2-pt and 4-pt resistance measurements and calculated it to be $\approx$ 135 Ω. Previous studies have shown that the contact resistance between metals and CNTs measured by simply placing CNTs on a metal electrode to be on the order of several hundreds of kilo ohms.[80] However, in our growth process, since the CNTs were directly grown on the metal electrodes, the contact resistance was significantly lower.

2.6 Tin Nanotubes Arrays on Microhotplates

2.6.1 Carbon Nanotube Arrays on Microhotplates

Encouraged by the positive results in achieving high-density CNT arrays on metallic substrates, we carried out the same process on microhotplates. The surfaces of a 16-element microhotplate array were initially pre-cleaned using an Ar-ion beam. Optical images of the microhotplate array used in this work are presented in Figure 2.11. The bimetallic catalyst solution was prepared as detailed before. A drop of the catalyst solution was then placed over the chip containing the array and dried. The package was secured to a fixture equipped with gas-inlet and exhaust lines such that the microhotplate surfaces were sealed from the outside air through a viton O-ring. Mass-flow controlled gas lines carrying nitrogen (N_2), hydrogen (H_2) and acetylene (C_2H_2) were connected to the gas-inlet to the fixture containing the microhotplates. The microhotplate surfaces were individually annealed in 100 sccm N_2 (1 sccm = 0.0167 cm^3/s) and 30 sccm H_2 for 2 min followed by CNT growth in 5 sccm C_2H_2 for 5 min, at 600 °C.
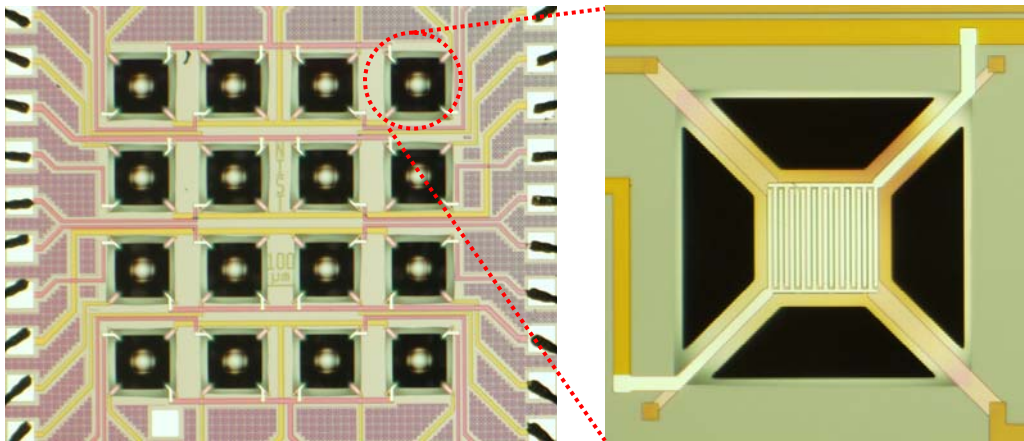
Figure 2.11 – Optical images of a 16-element microhotplate array and a single microhotplate consisting of interdigitated comb-like contact pads (Distance between pads $\approx$ 2 μm)

38

2.6.2 Tin Oxide CVD on Carbon Nanotube Arrays

The microhotplate package was loaded into a low-pressure CVD chamber, which was pumped down to $\approx 10^{-4}$ Pa using a turbo pump and brought back up to ≈ 20 Pa under the flow of N_2. The hotplates were then exposed to a flow of tin nitrate $[Sn(NO_3)_4]$ for about 10 minutes to allow equilibration of gas flows within the chamber. The microhotplates (with and without CNTs) were then individually heated to 375 °C, for exposure times varying between 10-20 s. The flow of tin nitrate was then shut off and the gases were pumped out for another hour to completely remove all reactants, before the chamber was brought up to atmospheric pressure in N_2. The CNT templates were then removed completely by annealing the microhotplates in air at 450 °C for ≈ 8 h. The surface morphologies of the microhotplates were imaged using a Hitachi S-8000 scanning electron microscope (SEM) before and after SnO_2 CVD.

2.6.3 Surface Morphology

The SEM images of high-density, uniformly well-aligned forests of CNTs grown directly on microhotplates are shown in Figure 2.12. The CNTs have nominal diameters between 10 and 20 nm and lengths of the order of micrometers, representing a very high aspect ratio (L/D $\approx 10^4$). The irregularities seen in the top view of the forests is attributed to catalyst film cracking during the H_2 anneal step preceding CNT growth. However, the overall resistances of the CNT forests grown on several different microhotplates were observed to be in the range of 250 to 300Ω, indicative of their metallic nature and excellent adhesion to the contact pads. At this point, it is noteworthy that the CNT forests

were grown primarily using the buried polycrystalline silicon micro-heater as the heat source driving CNT nucleation and growth processes at such low growth temperatures. The growth conditions here are hence markedly different from conventional CNT growth processes within a high-temperature furnace.
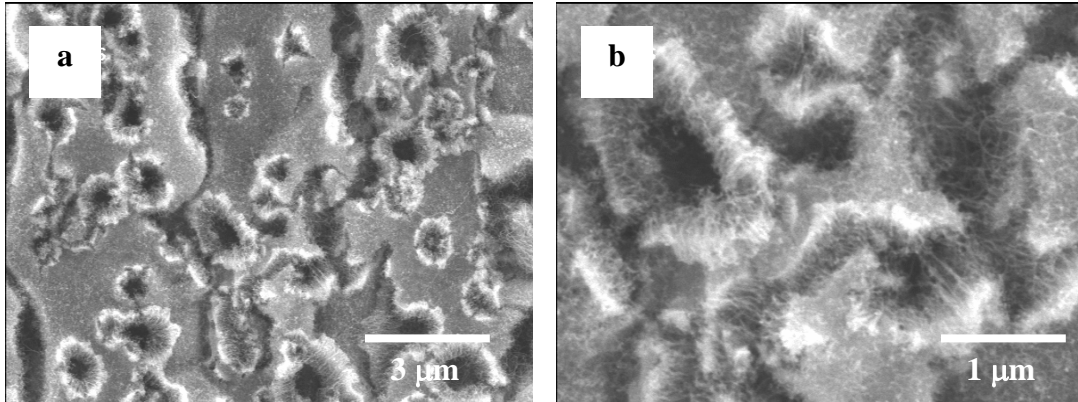
Figure 2.12 – Vertically aligned CNT forests grown directly on a microhotplate. The nanotubes completely covered the sensor pads.

The as-grown CNTs are typically multi-walled, exhibiting metallic character. Additionally, MWCNTs are generally chemically inert and hence are not useful for chemical gas sensing applications. However, the CNT forest packs an extremely high surface area within a small volume; thereby they could be used as templates for the creation of other nanomaterials. It is well known that MWCNTs can be easily etched away by thermal annealing in the presence of oxygen at temperatures over 400 °C. Thus coating the CNTs with SnO_2 followed by annealing would not only remove the CNT templates but would also ascertain SnO_2 crystallization.

During the SnO$_2$ CVD process, the sensor resistances marginally increased by $\approx$ 5 to 10 Ω depending on the time of deposition. However, the overall appearances of the coated microhotplates were clearly different upon inspection with an optical microscope. Upon annealing the SnO$_2$ coated CNT forests in air at 450 °C, the resistance across the sensor pads of the microhotplate increased steadily. The devices were observed to achieve stable baseline room-temperature resistances between $\approx$ 800 kΩ to 1 MΩ, after several hours of annealing, representing the successful removal of the underlying CNTs. SEM images of the microhotplate surface following CNT removal are shown in Figure 2.13. Remarkably, the surface morphology did not show signs of disintegration, maintaining the integrity of one-dimensional structure.
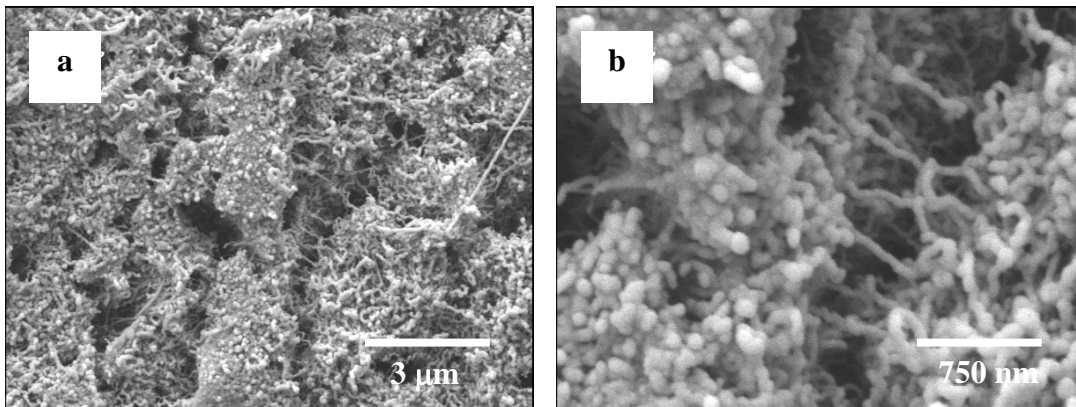
Figure 2.13 – SnO$_2$ nanotube surface following SnO$_2$ CVD and removal of CNT templates

2.7 Gas Sensing Measurements

2.7.1 Measurement Setup

Controlled mass flow rates of dilute methanol vapor and zero-grade dry air were delivered through a computer-automated delivery system. The test-gas mixture flow direction was switched between a bypass line and over the microhotplate array using a three-way valve. The microhotplate array itself was sealed from outside air and exposed only to the methanol/dry-air mixture or dry air. The resistance between sensor pads of the hotplate was monitored continuously during the sensing measurement cycle. Fixed temperature measurements of the responses of a microhotplate containing SnO_2 nanotubes and a microhotplate containing a SnO_2 thin film were recorded. A schematic diagram of the gas-sensing measurement setup and a digital photograph of the fixture containing microhotplate are shown in Figure 2.14.
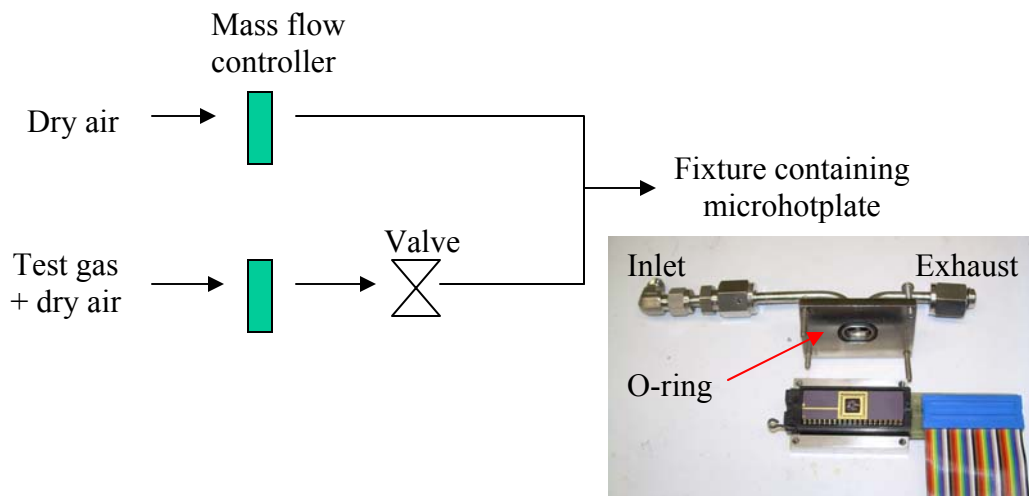
Figure 2.14 – Schematic representation of gas-sensing measurement setup

2.7.2 Gas Sensing Responses

The typical fixed temperature responses of the SnO_2 nanotubes to varying pulsed concentrations (10 to 100 ppm) of methanol at 300 and 400 °C are shown in Figure 2.15. Clearly, the nanotube sensor could detect even very low concentrations of methanol, as evidenced by the huge change in resistance measured between the sensor pads. The measurements were generally repeatable on several other microhotplates consisting of nanotubes within the same chip. The sensitivity of the samples was calculated as the ratio of the change in electrical signal upon exposure to methanol to the baseline signal, represented by the following equation:

$$S = \frac{\Delta R}{R} = \frac{R_{air} - R_{gas}}{R_{gas}}$$

A comparative plot of the sensitivities measured from the SnO_2 nanotube samples and the corresponding sensitivities of a plain SnO_2 thin film sample are shown in Figure 2.16. One of the key advantages of growing SnO_2 nanotubes directly on a microhotplate is reproducibility. The sensing responses from five different microhotplates consisting of SnO_2 nanotubes grown and processed under identical conditions resulted in highly reproducible sensing responses as well as sensitivities.
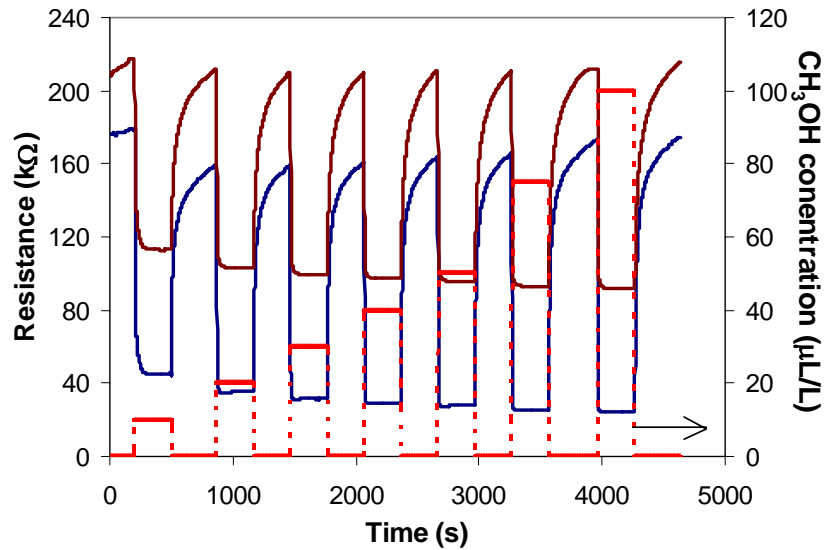
Figure 2.15 – Typical gas sensing responses measured from a SnO$_2$ nanotube covered microhotplate sample to varying concentrations of methanol (red, axis on the right) at 300 °C (brown, top) and 400 °C (blue, bottom).
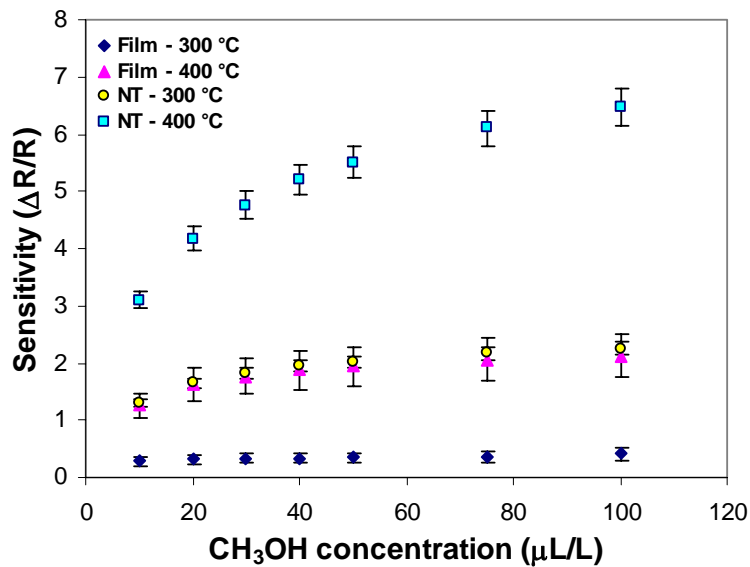
Figure 2.16 – Sensitivity plots of microhotplate surfaces covered with SnO$_2$ nanotubes (NT) and bare SnO$_2$ thin films at 300 and 400 °C to varying concentrations of methanol.

Clearly, the SnO_2 nanotube samples presented much higher sensitivities than a SnO_2 thin film operated under the same conditions. The responses of the nanotube samples were also very rapid even for minute concentrations of methanol. These effects are indeed due to the extraordinarily higher surface to volume ratios that the nanotubes possess in comparison with thin films. Thus, by simply including a CNT growth step prior to sensing film deposition, the sensing characteristics of the film were significantly improved. Moreover, the process developed may be extended to create nanotubes of several other metal oxides reflecting its generic nature.

2.8 Summary

A simple scheme for the growth of tin oxide nanotubes directly on microhotplates, using CNTs as templates has been described. During the course of synthesis of CNTs on microhotplates, two significant technical challenges were overcome, the first on achieving CNT growth on a range of conductive substrates including metals and metal alloys using a bi-metallic catalyst, and the second involving the direct growth of high-density CNTs on microhotplates using just a buried micro-heater as the heat source driving growth. Tin oxide nanotube structures were created by coating CNTs with tin oxide followed by the removal of carbon through a simple annealing process. The tin oxide nanotube coated microhotplates were observed to have much better sensing characteristics in comparison with bare tin oxide thin films operated under the same conditions. Thus, a single-step process for the improvement of sensor quality has been achieved, and the process may be replicated to create nanotube structures of any other

metal oxide. A highly sensitive electronic nose based on an array of microhotplates, each

covered with nanotubes of different metal oxides may hence be readily envisioned.

Chapter 3

Tungsten Oxide Nanowires

3.1 Introduction to tungsten oxide

3.1.1 Physical properties

As mentioned in the first chapter on the development of chemical gas sensors, among the binary metal oxides employed as sensing materials, SnO_2 has received maximum attention from researchers owing to its superior reactivity to a variety of gaseous species. However, due to its low level of selectivity, investigation of other metal oxides such as WO_3, ZnO, TiO_2 and In_2O_3 has increased multiple-fold in the last decade. For example, in the ongoing efforts to build an electronic nose, arrays consisting of various metal oxides as well as other materials have been utilized in conjunction.

Tungsten oxide is most commonly found to exist as WO_3, having a cubic perovskite-like structure with corner sharing of O atoms with central W atoms arranged in a regular octahedron, as seen in Figure 3.1.[81]
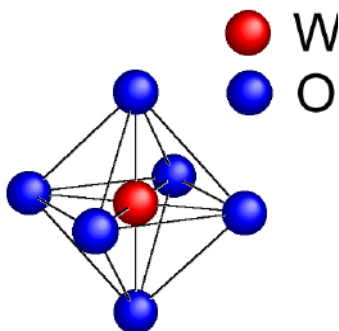
Figure 3.1 – Crystal structure of WO_3

WO$_3$ is known to exist in several stable sub-stoichiometric structures (WO$_x$, 2.5<x<3) called Magnéli phases, thereby enhancing its utility as an effective gas sensing material, since oxygen deficiencies play a key role in the gas sensing mechanism. Since the earliest reports on WO$_3$ as a gas sensor, there have been several studies and publications indicative of its advantages over other metal oxides in the detection of vapors of ammonia (NH$_3$), hydrogen sulphide (H$_2$S) and nitrous oxides (NO$_x$).[82-88] Apart from gas sensing, WO$_3$ has garnered attention for its interesting electrochromic and photochromic properties, which are valuable in the development of smart windows and information displays.[89-91]

3.1.2 Prior work on tungsten oxide nanostructures

Very recently, Lee et al. reported the growth of tungsten nanowires of less than 100 nm in diameter and about 1 μm in length by thermal treatment of tungsten films in the presence of H$_2$, and demonstrated excellent field emission properties.[92] Gu et al. grew tungsten oxide nanowires on metal tungsten tips (prepared by electrochemical etching of tungsten wires) heated in argon at 700 °C.[93] They observed tungsten oxide nanowires between 10 and 30 nm in diameter and about 300 nm in length. Well-aligned nanowire arrays of molybdenum oxide were grown through thermal evaporation at 1100 °C by Zhou et al. and subsequently reduced to molybdenum nanowires under a heated H$_2$ atmosphere.[94] Using a similar approach, Liu et al. synthesized large-scale arrays of aligned tungsten oxide nanorods by heating a spiral tungsten coil to ≈ 1000 °C.[95] Vaddiraju et al. also demonstrated vapor phase synthesis of tungsten and tungsten oxide

nanowires in a hot-filament CVD reactor, at temperatures above the decomposition temperature of tungsten oxide ($\approx$1450 °C).[96] Three-dimensional tungsten oxide nanowire networks have also been grown through a chemical vapor transport process involving the direct thermal evaporation of tungsten powders at $\approx$1450 °C at low pressures.[97] Apart from nanowires, other nanostructures such as whiskers and hollow fibers of tungsten oxide have been studied in the past.[98-100] More recently, Li et al. grew $W_{18}O_{49}$ nanotubes and nanowires by infrared irradiation on W foils under different vacuum conditions.[101]

3.1.3 Motivation for this work

Working temperatures below 620 °C are essential for successful operation of microhotplates. We have devised an approach to substantially reduce the processing temperature required to restructure tungsten thin films directly into tungsten oxide nanowires by coupling RF plasma with the growth process. Surprisingly, in addition to nanowires, we also observed that in regions of restricted gas-phase mass transfer, the tungsten film was converted into unusual hollow nanostructures of square cross-section. A few of these nanostructures, termed microducts, were seen to be quite long (10 to 200 μm) with edge lengths of 0.5 μm. Based on a series of experiments, we understood that the growth mechanisms of nanowires and microducts were quite different, the former occurring by nucleation from the vapor phase, and the latter involving surface restructuring of the thin film and growth in regions of restricted gas-phase mass transfer. After the growth processing conditions were optimized using tungsten thin films deposited on Si wafers, we successfully reproduced the same process on a tungsten-coated microhotplate. A comparative study between the gas sensing properties of a

tungsten oxide nanowire coated microhotplate and a tungsten oxide thin film coated microhotplate to trace concentrations of nitrous oxide established the superior sensing properties of the nanowires.

3.2 Nanowire and microduct syntheses and characterization

3.2.1 Experimental setup

Tungsten films of 300-350 nm were deposited on a flat, polished substrate (1 cm^2) of sapphire by DC-magnetron sputtering from a high purity tungsten (99.99% pure) target with pure argon (99.9995% pure) as the sputtering gas. The substrate was then secured to a heater-plate assembly using a ceramic clip and transferred (in air) to a low-pressure CVD chamber where argon and H_2 were metered with mass flow controllers, and chamber pressure maintained at 5 torr during growth using a rotary mechanical rough pump. Ar flow rate was kept constant at 300 sccm for all experiments. The substrate temperature was then maintained between 500 and 700 °C and monitored using a thermocouple in contact with the substrate. An RF-plasma was easily generated within the chamber by winding a copper coil around the 7.5 cm cylindrical quartz chamber, and the plasma power (20 W) was controlled using a matching network. Growth times were typically 10 minutes, after which the heater was turned off and the substrate was cooled to room temperature, while the chamber was continuously purged with Ar and H_2. A schematic diagram representing the experimental setup employed for the growth process is shown in Figure 3.2. For growth on microhotplates, a tungsten thin film coated microhotplate was heated to 550 °C under similar process conditions.

After growth, substrate morphologies were imaged using a Hitachi S-4000 field emission scanning electron microscope (SEM). Nanowires grown directly on a commercial tungsten TEM grid were imaged using a Zeiss CM-10 transmission electron microscope (TEM).

CVD chamber   Purple RF plasma zone   Ceramic clip

Ar + H$_2$

Copper coil   Substrate heater   Pump outlet
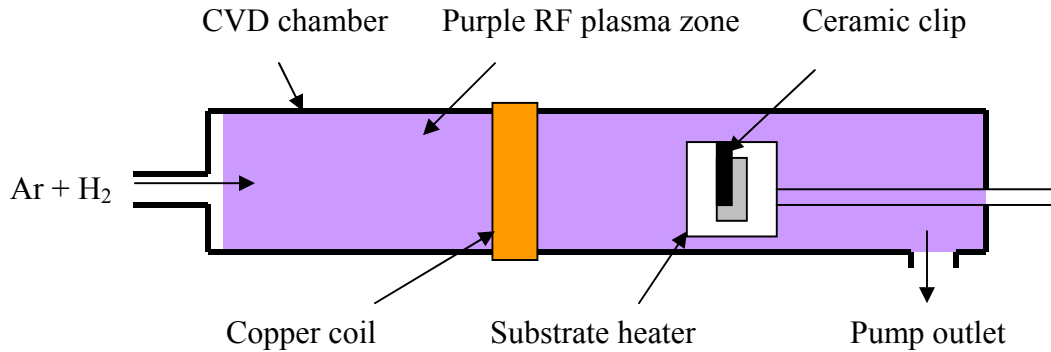
Figure 3.2 – Schematic diagram of experimental setup

3.2.2 Surface Morphology Study

Initially, experiments were conducted in the absence of the RF plasma. Heating the film in pure Ar between 750 and 800 °C without any H$_2$, resulted in the restructuring of the smooth tungsten surface into a grainy, nodular one, as seen in Figure 3.3. However, when H$_2$ was introduced (30 sccm) along with Ar at these temperatures, nanowires appeared on the surface, similar to those observed by Lee et al.[92] With an RF plasma, it was found that a lower substrate temperature and a lower concentration of H$_2$ also produced nanowires. Figure 3.4 shows the result of heating a tungsten film to ≈ 550 °C with a reduced H$_2$ flow rate of 5 sccm for 10 minutes. A uniformly dense network of nanowires was seen to have grown with diameters between 10-30 nm and lengths between 0.5-1 μm.

51
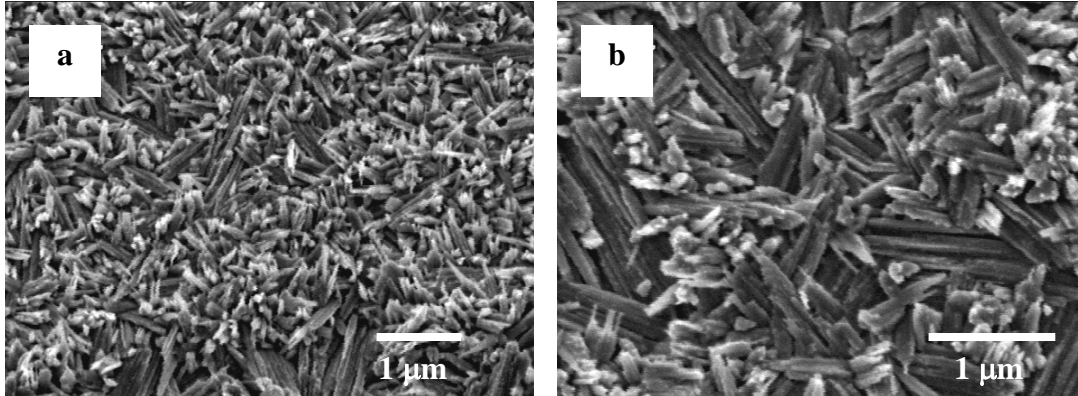
Figure 3.3 – SEM images of grainy, nodular surface of tungsten film heat treated at 750 °C in pure Ar.
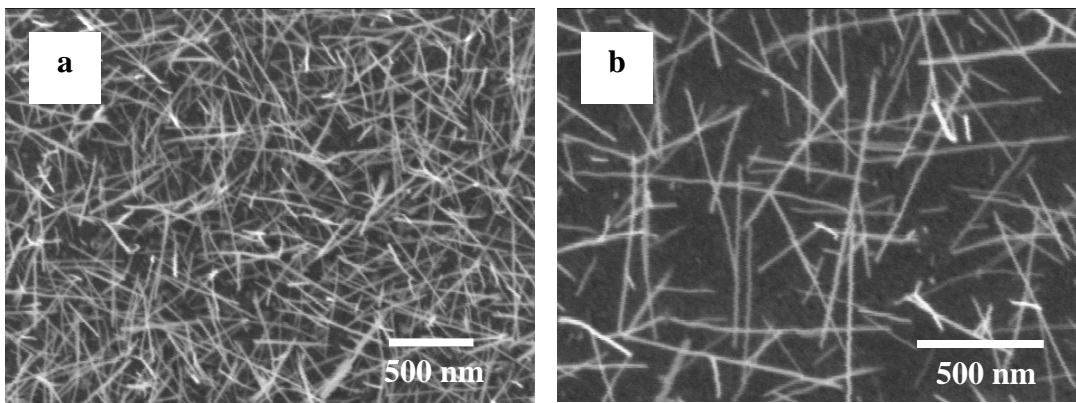
Figure 3.4 – Uniform network of nanowires grown by heating a tungsten film at 550 °C in RF Ar/H$_2$ plasma.

Increasing the substrate temperature to 600 °C produced several larger crystallite structures in addition to nanowires. However above ~ 620 °C, no evidence of wires could be found; rather the films consisted of large crystallite structures of various shapes as well as solid square nanorods. Typical surface morphologies for these process conditions are shown in Figure 3.5.
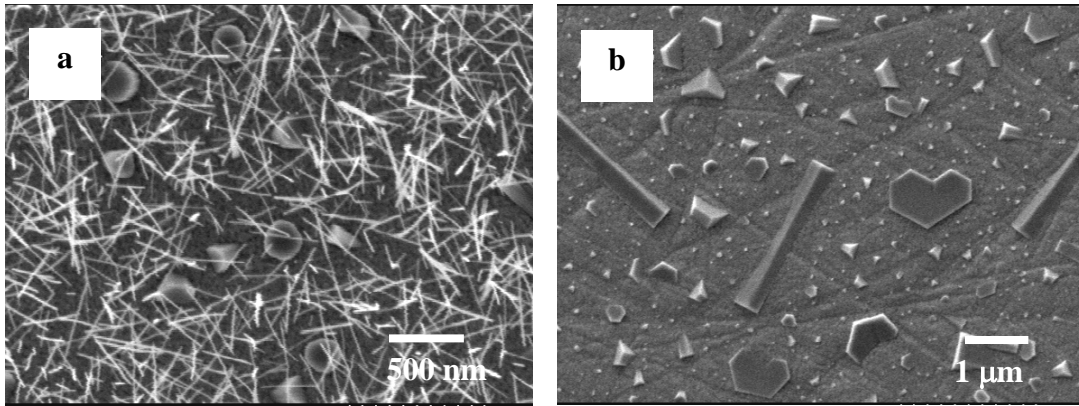
Figure 3.5 – (a) Nanowires and crystallite structures grown by heat treatment of tungsten film at 600 °C in RF Ar/H_2 plasma. (b) Solid nanorods and other crystallite structures grown at 650 °C in RF Ar/H_2 plasma.

A significant finding was that for samples which were heated to temperatures between 550 and 620 °C, several unusual hollow microstructures with a square cross-section (henceforth referred to as "microduct") had grown in the region of the substrate underneath the ceramic clip that was securing the sample. These microducts had average edge lengths of ≈ 0.5 μm, wall thickness of about 20 to 30 nm, and lengths ranging from tens to a few hundreds of micrometers. The SEM images of the microducts are presented in Figure 3.6.
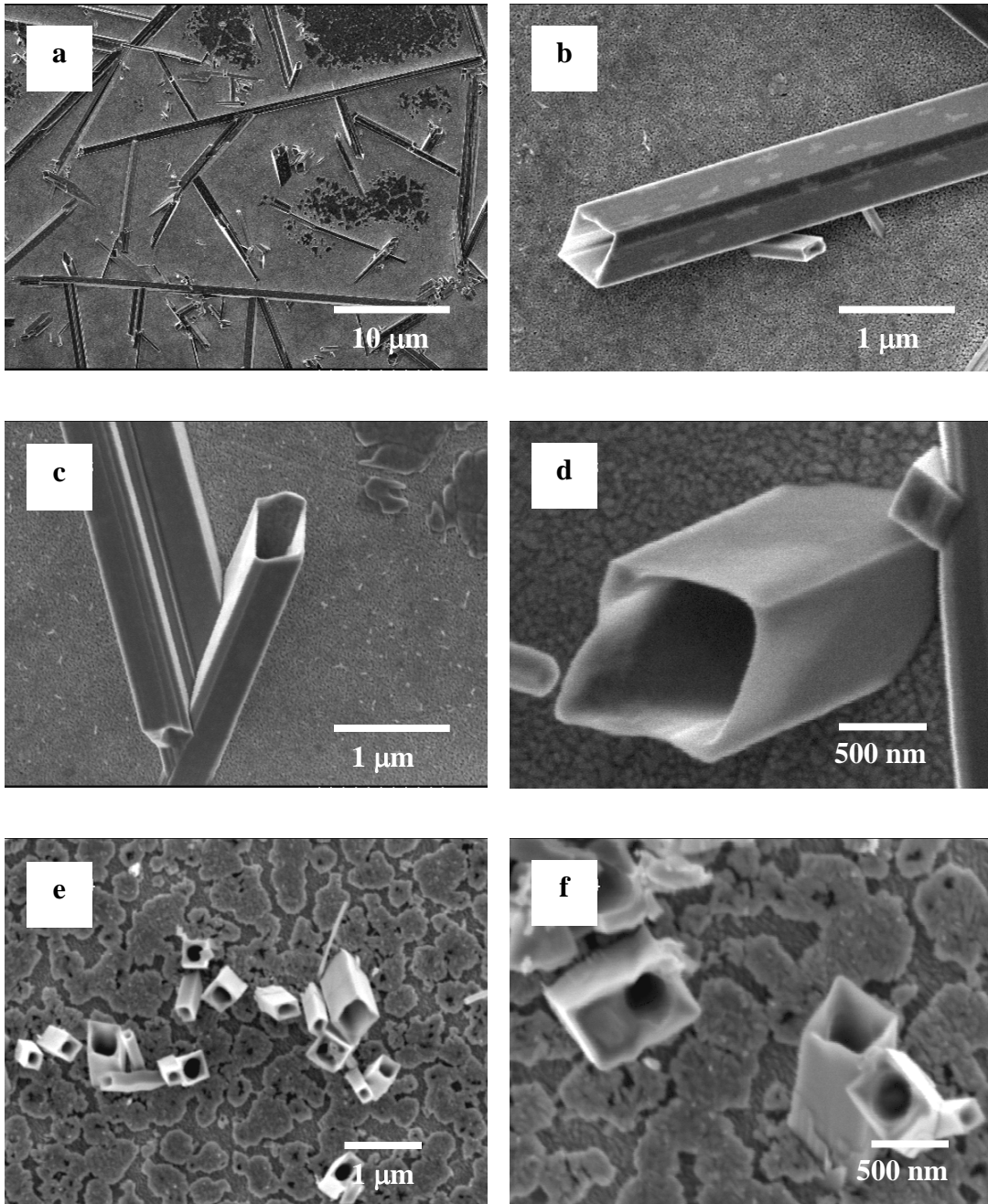
Figure 3.6 – Hollow, square microducts observed to grow in the certain specific regions of the substrate. (a-d) and (e-f) represent ducts grown on 2 different samples. Some of the ducts were several hundred microns long.

To test the generality of our process, we heated a 0.005" diameter tungsten wire (Alfa Aesar), as well as a tungsten coated TEM grid (Pacific Grid Tech – 200 mesh) subject to 550 °C in an RF Ar/H_2 plasma within the chamber, and observed that nanowires grew over the entire surface of both the wire and the TEM grid, as evidenced in Figures 3.7 and 3.8.
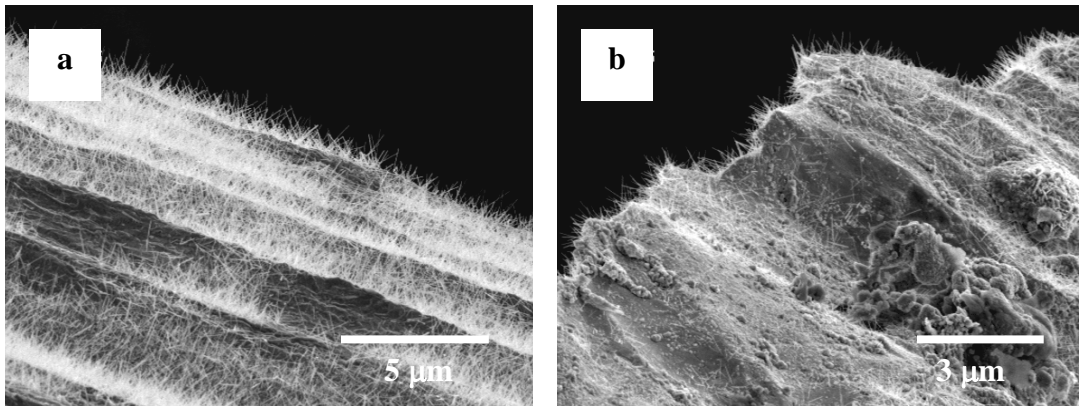
Figure 3.7 – Nanowires grown on the surface of a commercial tungsten wire heated at 550 °C in RF Ar/H_2 plasma. Some nanowires extend out from the edge of the wire.
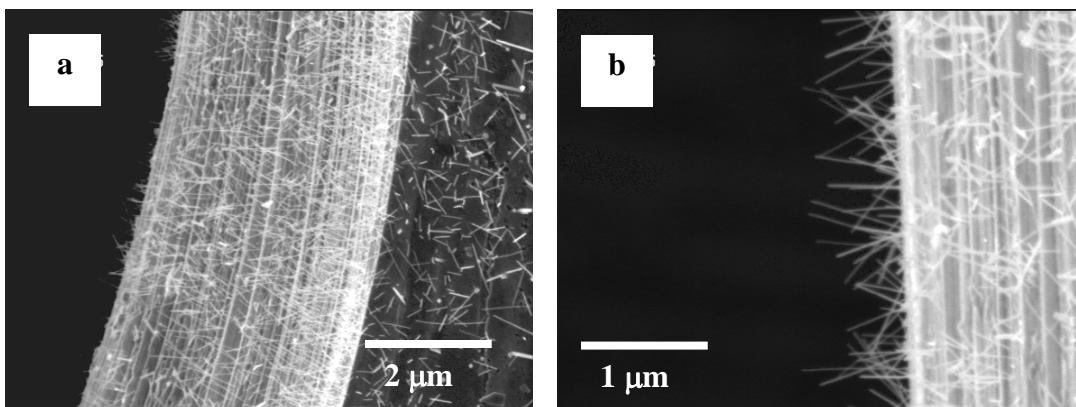
Figure 3.8 – Nanowires grown on the surface of tungsten TEM grids heated at 550 °C in RF Ar/H_2 plasma.

3.2.3 Structural Characterization and Crystallography

Nanowires grown on the tungsten TEM grid were analyzed by transmission electron microscopy (TEM) to obtain phase information and growth direction. Low and high-resolution TEM images of a nanowire and electron diffraction patterns obtained from two different nanowires, are shown in Figure 3.9. Upon inspecting several different nanowires, two different electron diffraction patterns were observed, as seen in Figures 3.9 (c), (d). The d-spacings of approximately 0.38 nm and 1.75 nm corresponded most closely to the d-spacings of $W_{18}O_{49}$. The streaked pattern obtained from some other nanowires, indicates the presence of disordered intergrowths, which may be due to varying oxygen stoichiometry within different nanowires.
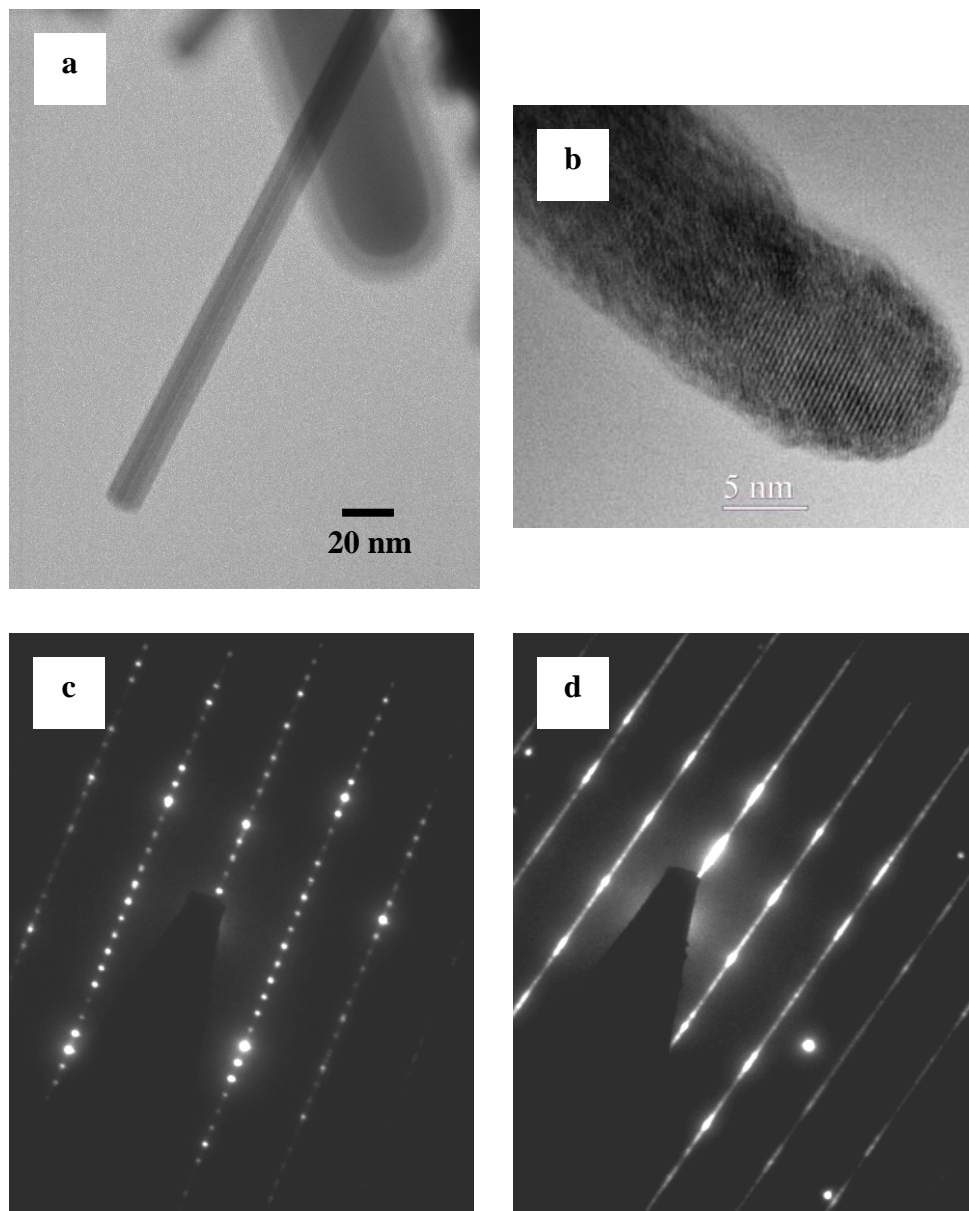
Figure 3.9 – (a,b) Low and high resolution TEM images of W nanowires. (c,d) Electron diffraction patterns arising from 2 different nanowires.

3.3 Description of Growth Mechanism

3.3.1 Vapor-solid mechanism

Since no catalyst material was present to initiate the growth of nanowires, the VLS (vapor-liquid-solid) growth mechanism does not apply here. Growth of nanowires may be explained based on a modified VS (vapor-solid) mechanism, where the tungsten film deposited on the substrate acts as a self-catalytic layer.[102] Upon heating the film to 550 °C in low-pressure plasma (~ 4 torr), the volatile surface oxide evaporates. This vapor phase oxide should be reduced in the H_2 plasma to a lower tungsten oxide, which then re-condenses back on the film surface as a nanowire. A schematic diagram of the V-S growth mechanism for the nanowires is depicted in Figure 3.10. The vapor phase mechanism was confirmed, as nanowires were also seen to form on a pristine silicon wafer placed just above the heated tungsten sample. This mechanism implied that a source of oxygen (background from the rough vacuum pumped chamber) played a necessary role in constantly oxidizing the tungsten film so as to create a volatile tungsten containing species. To test this hypothesis, we conducted experiments in a high vacuum chamber. A tungsten sample heated to about 700 °C in pure H_2 and Ar failed to produce any nanowires. However, when a trace amount of air or oxygen (1-2 vol. %) was bled into the system, nanowires appeared.

Reduction by H_2

Volatile WO_x Condensation
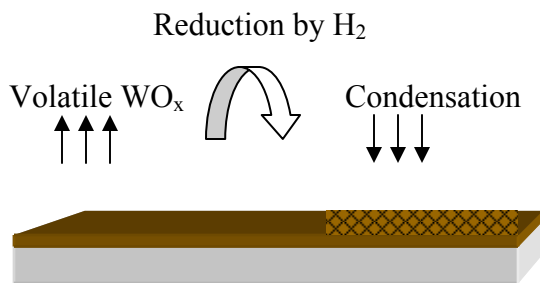
Figure 3.10 – Vapor-solid growth mechanism of WO_x nanowires

3.3.2 Role of Mass Transfer

We believe that gas phase mass transfer rate of the reducing agent may play a pivotal role in determining whether growth of nanowires or microducts are preferred, since the latter grew only in specific regions underneath the clip. To test this hypothesis, we placed a ceramic substrate at a slight angle to the heated tungsten substrate as schematically illustrated in Figure 3.11. The purpose was to impose a mass transfer resistance of varying degree to the substrate and observe the resulting morphologies at different points along the length of the substrate. We discovered that the tungsten oxide nanowires grew over most of the sample, but with a higher density in the regions farthest from the contact point between the two substrates. Microducts and tungsten oxide crystallite structures were observed to grow exclusively in the region where the gap between the substrate and sample was very narrow. The occurrence of nanowires with varying oxygen levels may also be explained through such an argument.
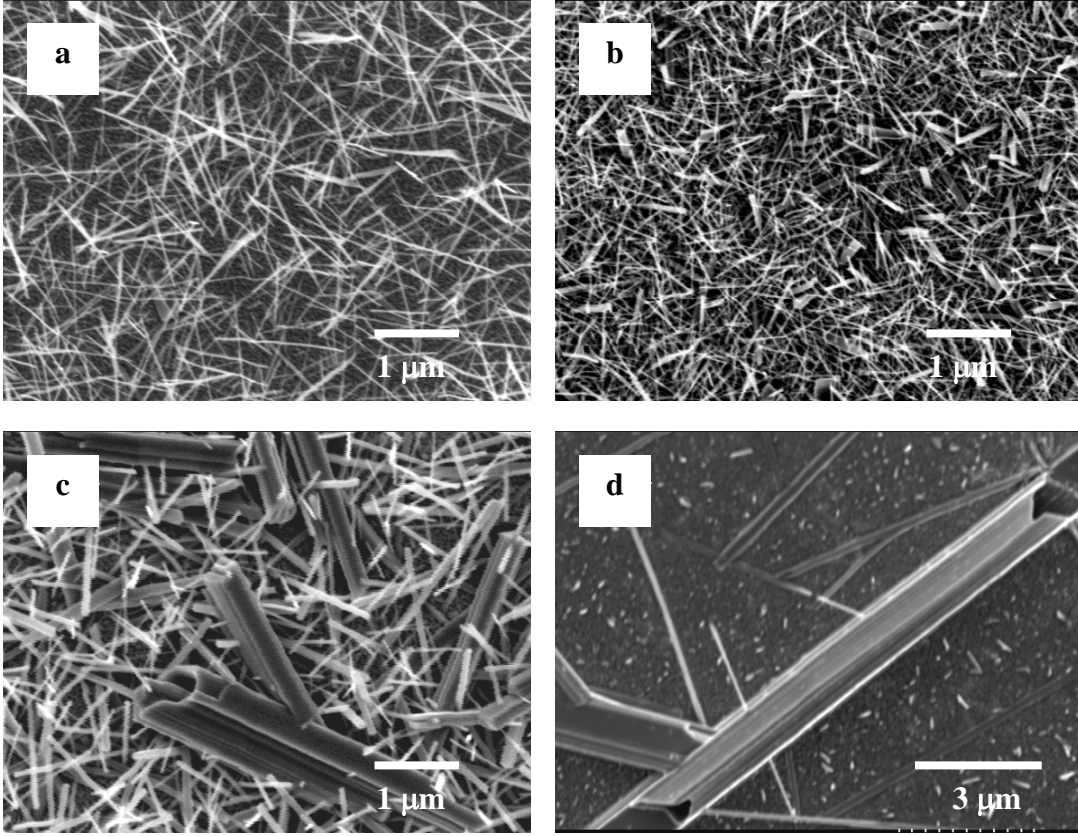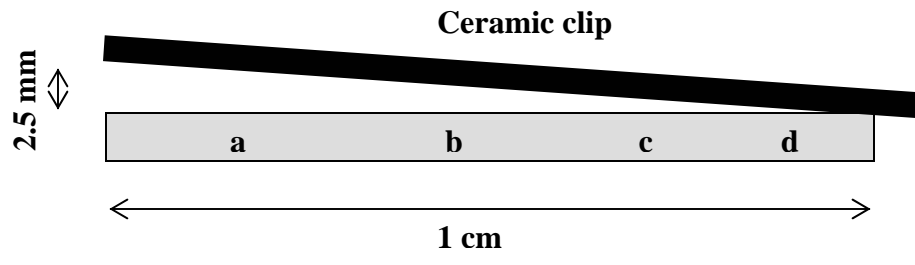
Figure 3.11 – Schematic illustration of clip-substrate assembly used for mass-transfer dependence study. SEM images depict nanostructures grown in the regions indicated along the length of the substrate. (From left edge, a = 2 mm, b = 6 mm, c = 8.5 mm, d = 9.5 mm)

Mayers and Xia recently reported on the growth of hollow nanotubes as well as solid nanorods of tellurium through a solution phase approach.[103] They observed that varying the mass transfer rate of tellurium to the seed surface could control the type of nanostructure grown, a lower tellurium concentration resulting in the hollow nanotubes while a higher concentration resulted in solid nanorods. We believe that the hollow microducts of tungsten oxide grew only in regions on the substrate that offered maximum resistance to gas phase mass transfer of H_2, which in turn influenced the rate of addition of tungsten oxide to the surface. At temperatures greater than 620 °C, the production rate of tungsten oxide atoms is enhanced allowing uniform addition of tungsten oxide over the entire surface and resulting in solid nanorods and other stable crystallite structures.

3.3.3 Role of Reducing Agent

To verify the role of H_2 as reducing agent rather than as an agent for creation of a WH_x species, we replaced the H_2 with carbon monoxide (CO), and heated the sample to 550 °C in the RF plasma. The results were quite definitive in showing that H_2 was not necessary for the growth of nanowires so long as another reducing agent was present, as observed in Figure 3.12. However, instead of hollow microducts with regular square cross-section, we observed several hollow nanostructures of irregular shapes (Figure 3.13). This difference in nanostructures resulting from a different reducing agent may be due to the weaker reducing effect of CO in comparison to H_2 in addition to dissimilar mass transfer rates.

61
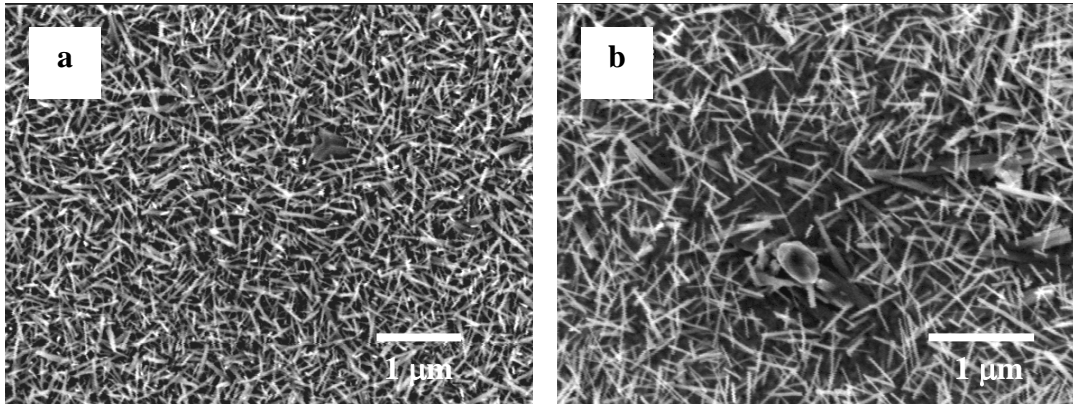
Figure 3.12 – Uniform network of nanowires grown by heating a tungsten film to 550 °C in RF Ar/CO plasma.
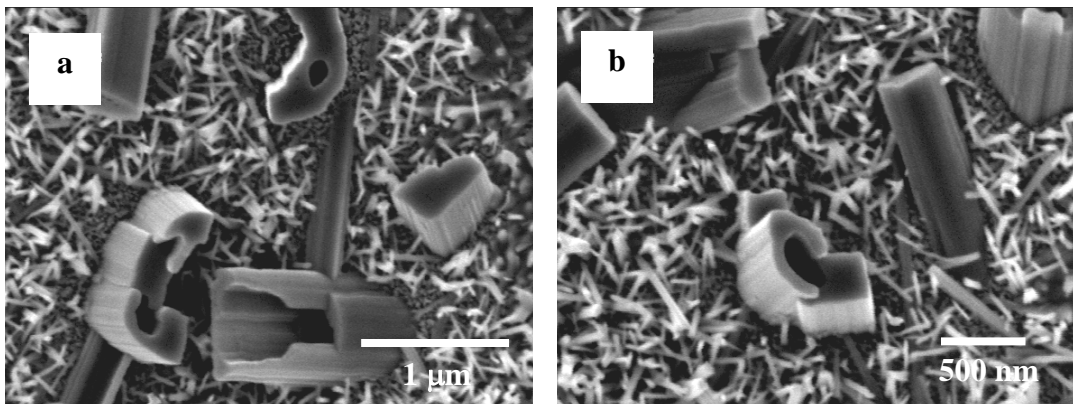
Figure 3.13 – Irregular hollow nanostructures and solid nanorods observed to grow on a tungsten surface heated to 550 °C in RF Ar/CO plasma.

3.4 Gas Sensing Measurements

We have done some preliminary tests on the application of WO_x nanowires grown by this approach, as gas sensors. Gas sensing properties of WO_3 nanoparticle films have been studied in the recent past, showing excellent sensitivity to H_2S gas and selectivity to other gases.[85] In our experiment, nanowires were grown on a microhotplate, annealed in air at 500 °C for 30 minutes, which possibly completely oxidizes them into WO_3, and

then exposed to the test gas (20 ppm of NO_2/NO in air). An optical image of the tungsten-coated microhotplate prior to processing is shown in Figure 3.14. SEM images of the annealed WO_3 nanowires grown device used for gas sensing measurements are shown in Figure 3.15.
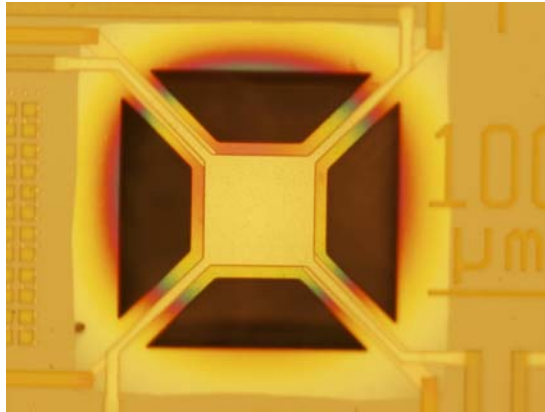
Figure 3.14 – Optical image of a tungsten thin film coated microhotplate device prior to nanowire growth
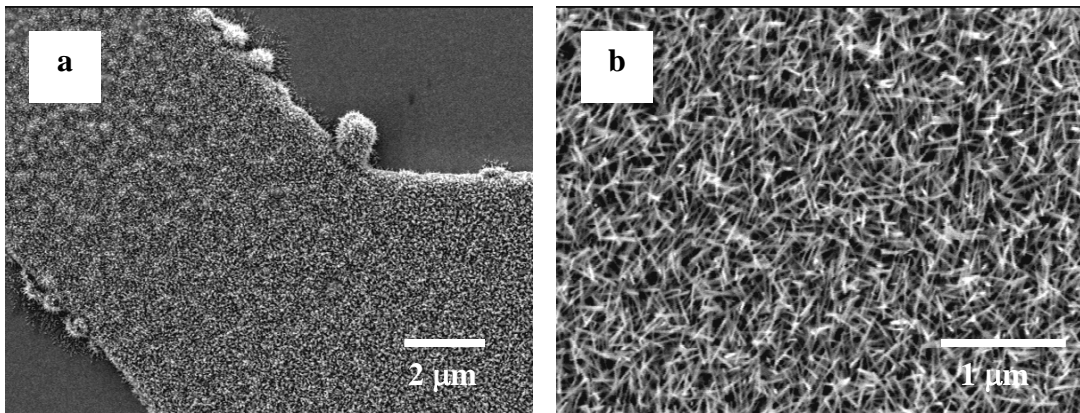
Figure 3.15 – SEM images of tungsten oxide nanowires grown on a microhotplate

The typical sensor responses to 20 ppm concentrations of nitrous oxide from surface covered with WO$_3$ nanowires and from a WO$_3$ thin film based on multiple runs are shown in Figure 3.16.
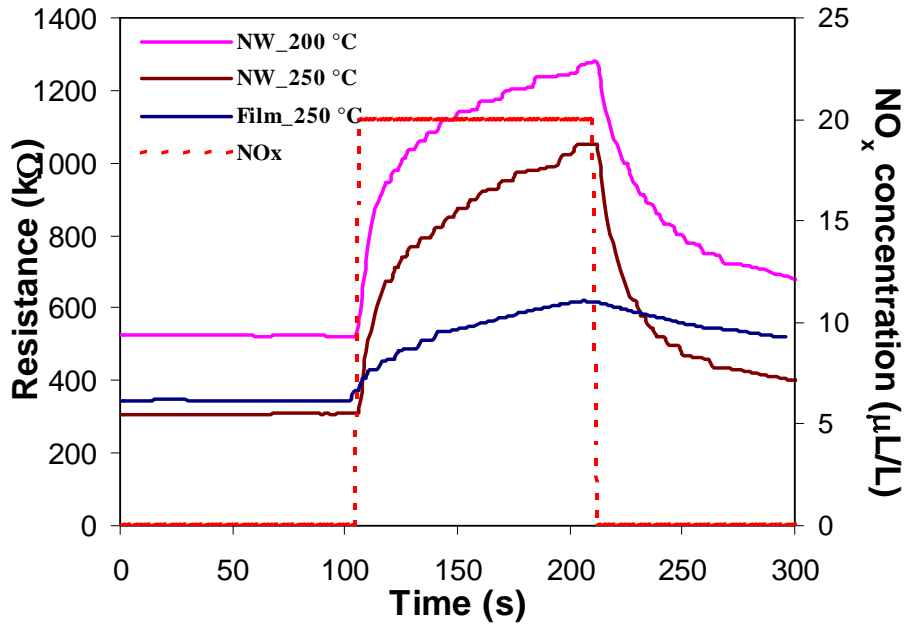
Figure 3.16 – Gas sensing responses to 20 ppm NO$_x$ recorded from WO$_3$ nanowires and a WO$_3$ thin film

The sample covered with WO$_3$ nanowires exhibited much better sensitivities as well as better recovery patterns when compared with a WO$_3$ thin film. Overall, a simple one-step thermal treatment of a W thin film at 550 °C in RF Ar/H$_2$ plasma has been shown to create much better sensing characteristics.

3.5 Summary

In summary, we have developed a method of restructuring tungsten substrates into tungsten oxide nanowires and hollow microducts by simple thermal treatment in RF plasma at temperatures between 550 and 620 °C, in the presence of a reducing gas like H_2 or CO. The nanowires have diameters between 10 and 30 nm with lengths up to 500 nm, while the microducts have square edge lengths of approximately 0.5 μm and lengths up to a few hundred micrometers. It is worth pointing out that the growth temperature of tungsten oxide nanowires in our work is significantly lower (by about 250 °C) than previous methods. A trace amount of background oxygen is essential in growth of these nanostructures, which can be grown preferentially by controlling the mass transfer rate of gas phase species to various regions on the substrate. Nanowires were also grown on commercial tungsten wires and tungsten coated TEM grids, reinforcing the generality of the process. Apart from field emission sources, these nanowires could be employed as tips for STM and AFM. In addition, nanowires annealed in air are capable of sensing low concentrations of NO_x. The hollow microducts could find applications as building blocks for many functional devices like micro-batteries, as micro-fluidic channels, and in micro-encapsulation for drug delivery.

Chapter 4

Zinc Oxide Nanowires

4.1 Growing interest in zinc oxide

4.1.1 Physical properties

Zinc oxide (ZnO) is a key technological material possessing several interesting physical, chemical, mechanical and optical properties finding utility in an extensive range of applications. The crystal structure of ZnO is commonly referred to as the wurtzite structure, with a hexagon-shaped unit cell. The structure may be described as having alternating planes consisting of tetrahedrally coordinated O^{2-} and Zn^{2+} ions, stacked along the c-axis or [0001] direction, as illustrated in Figure 4.1. The non-central symmetry in the ZnO crystal structure leads to its interesting piezoelectric and pyroelectric properties.
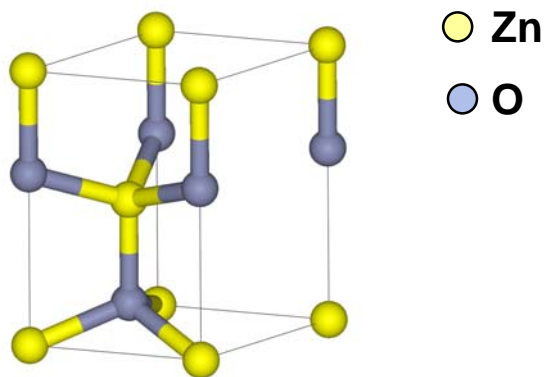
Figure 4.1 – Wurtzite crystal structure of ZnO

4.1.2 Prior Work on ZnO Nanostructures

ZnO is a wide-bandgap semiconductor (E_g = 3.37 eV) with a wurtzite crystal structure with an emission spectrum in the ultraviolet/blue regime, suitable for a variety of electronic and photonic applications. Since the seminal work on the demonstration of an optically pumped ZnO nanowire nanolaser in 2001, there has been an exponential increase in scientific research focused on synthesis and design of ZnO nanostructure-based devices.[104] One-dimensional ZnO nanowires have been proven to be excellent candidates for nanoscale devices such as UV/visible photodetectors, FETs, solar cell electrodes, and chemical gas sensors.[105-108]

A recent article by Xiang et al. described the growth of p-type ZnO nanowires directly on sapphire, through phosphorus doping from phosphorus pentoxide.[109] This process has opened up several avenues for further research including novel nanoelectronic devices such as nano-LEDs, and electrically driven nanolasers. Very recently, the piezoelectric properties of ZnO nanowire arrays have been studied as a possible method of generating power to run nanoscale devices as well as the design of novel piezo-electric transistors, diodes and actuators.[110-112]

4.1.3 ZnO Nanostructure Synthesis Techniques

Synthesis of well-aligned nanowire arrays of ZnO is of prime importance for the realization of nano-electronic devices like LEDs and laser diodes. Several groups have synthesized ZnO nanowires by simple thermal evaporation of commercial Zn and ZnO

powders.[113-114] Huang et al developed a vapor transport and condensation process for growing ZnO nanowires by carbothermal reduction of ZnO powder, using a gold catalyst.[104] Gao et al. grew aligned ZnO nanowires using a similar approach using tin as catalyst.[115] Metal-organic CVD (MOCVD) of ZnO nanorods has also been demonstrated using precursors like diethyl zinc and zinc acetylacetonate hydrate.[116-117] Other techniques for the growth of nanowire networks include template assisted synthesis and electric field alignment.[118-119] Apart from nanowires, several other interesting morphologies of ZnO including nanocombs, nanobelts, seamless nanorings, nanoribbons, tetrapods etc. have been grown and studied.[120] A solid-vapor process involving direct thermal evaporation of ZnO at temperatures above 1300 °C grew most of these nanostructures. Topical reviews on the synthesis of various ZnO nanostructures, their growth kinetics and potential applications may be found in Refs [120-122].

4.1.4 Motivation for This Work

Despite significant advancements in nanowire growth techniques and device descriptions, establishment of electrical contacts to nanowire assemblies through non-destructive methods has not yet been successfully realized. The commonly employed method involves physically removing nanowires from the sample, dispersing them in solution, and transferring them onto another surface containing probe pads, and depositing contact electrodes onto individual nanowires through some form of lithography.[108] Such a series of steps are not only destructive, but also expensive and tedious. Another method described in literature involves burying the nanowire array in an insulating matrix such as spin-on glass or polystyrene, followed by plasma etching to

expose the nanowire tips.[123] However, this approach prevents access to the surface of the nanowires, which would be necessary for applications like gas sensing.

We have developed a simple method for growing contact electrodes in-situ to the top of a vertically aligned nanowire assembly by selectively attaching gold nanoparticles to the tips of nanowires and forming a continuous film. The electric field enhancements around the sharp tips of nanowires as well as their high aspect ratios are exploited in this procedure, which is generic to a wide range of nanomaterials and nanostructures. The result is a device, which consists of an ensemble of single nanowire devices connected in parallel. For sensor applications there may be signal to noise advantages in such an arrangement compared to single nanowire devices. Previous nanowire-based sensors have involved disordered nanowire networks, where electrical contact is determined primarily by the contacts between individual nanowires.[108,124] In contrast, this new device's properties reflect the electrical transport along isolated nanowires. Our approach may also be suitable for electrically driven optical devices based on nanowires.

4.2 Nanowire Syntheses and Characterization

4.2.1 Experimental Setup

For catalytic nanowire growth, silicon wafers (1 cm^2) were ultrasonically cleaned in acetone and 15 nm of chromium (Cr) followed by 150 nm of gold (Au) were deposited by thermal evaporation (Cr was deposited to ensure better adhesion of Au to the substrate). Non-catalytic growth of ZnO nanowires was directly carried out on plain silicon wafers (1 cm^2). The substrates were placed in an alumina boat containing commercial Zn powder

69

(Aldrich, 99.5%), and loaded into a quartz tube placed within a horizontal tube furnace, the substrates being held 5 cm downstream of the Zn powder. The tube was then evacuated using a rotary mechanical vacuum pump, followed by the introduction of 150 sccm (standard cubic centimeters per minute) nitrogen (N_2) and 10 sccm oxygen (O_2) and brought back up to atmospheric pressure. The nanowires were grown at 550 °C for about 2 h and the substrates were then cooled down to room temperature.

4.2.2 Characterization Techniques

Nanowire-grown substrate morphologies were imaged by SEM while crystallography studies were carried out using wide-angle x-ray diffraction. TEM and selected area electron diffraction (SAED) were performed on individual nanowires. The optical properties of the nanowires were analyzed through photoluminescence.

4.2.3 Description of Synthesis Results

The SEM images of non-catalyzed ZnO nanowire arrays grown directly on a Si wafer are shown in Figure 4.2. The nanowires grew uniformly over the entire substrate surface, with diameters between 400 and 450 nm, and lengths between 10 and 15 μm. Aligned nanowires were also observed to grow out from the substrate edges, as observed in Figure 4.2 (a). The nanowires were nicely faceted with flat, hexagonal heads and had nearly uniform lengths and diameters.
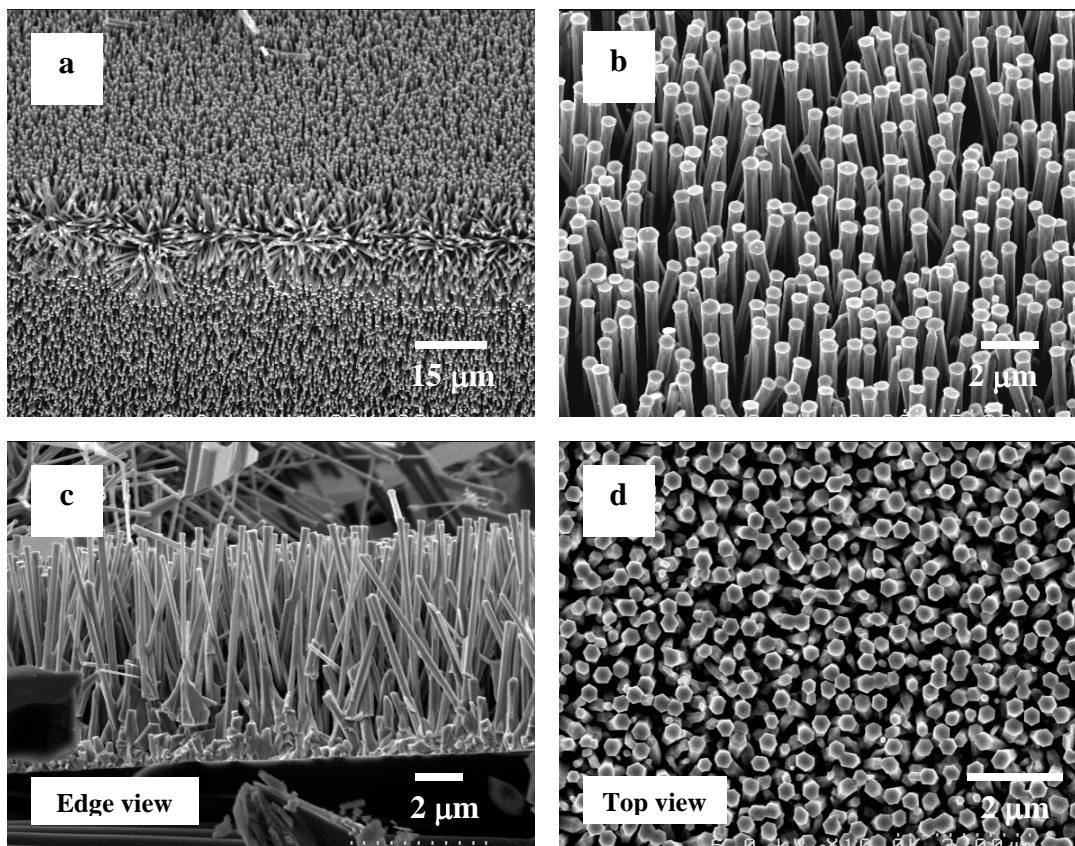
Figure 4.2 – Aligned ZnO nanowire arrays grown directly on a Si wafer at 550 °C. (a) and (b) represent images of nanowires from a 45° perspective.

SEM images of Au catalyzed ZnO nanowire arrays are shown in Figure 4.3. Once again, uniform and highly oriented nanowires were observed to grow from the Au catalyst layers. The typical nanowire diameters were between 50 and 70 nm with lengths ranging between 8 and 10 μm depending on the time of growth.
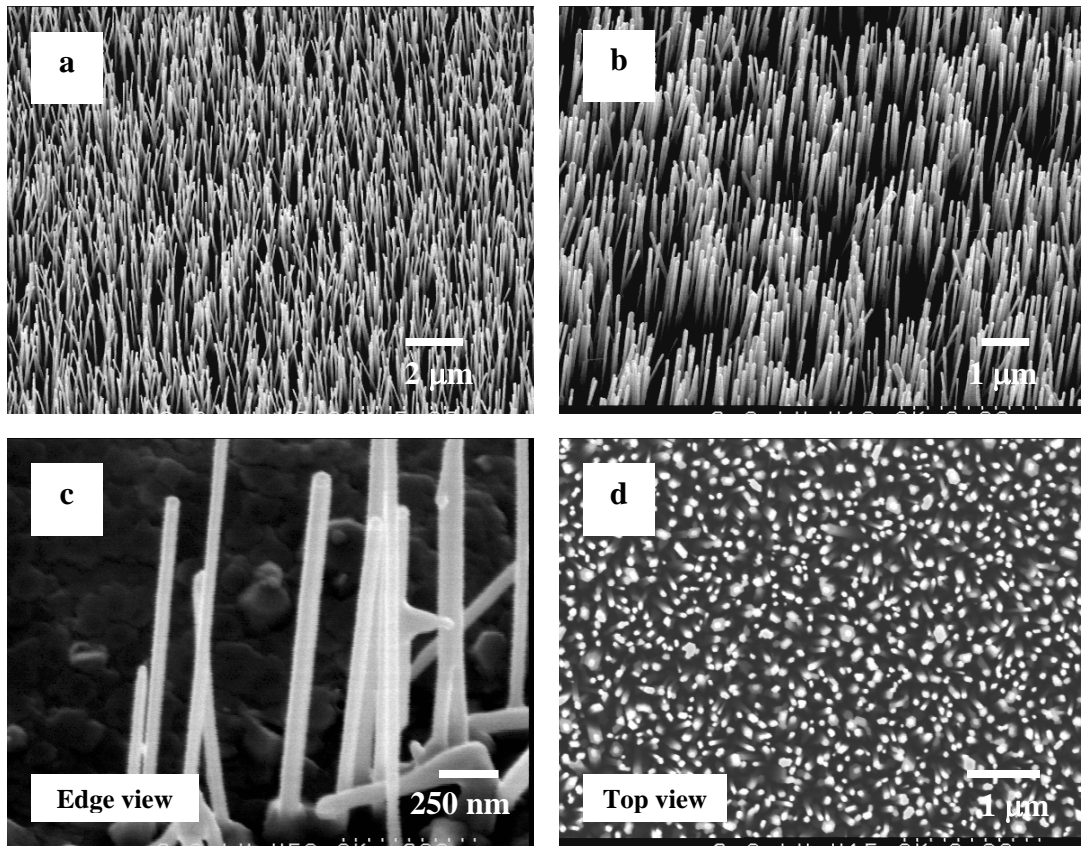
Figure 4.3 – Aligned ZnO nanowire arrays grown on Au coated Si wafers at 550 °C. (a) and (b) were imaged from a 45° perspective.

Figure 4.4 represents a typical XRD pattern obtained from the nanowires, where the sharp peak at a 2-theta value of 34.42° corresponds to the (002) plane of the hexagonal ZnO crystal. TEM and electron diffraction analysis of individual nanowires revealed that the nanowires are single crystalline, with a growth direction along the c-axis of ZnO, shown in figure 4.5. The spacing of 2.56 ± 0.05 Å between adjacent lattice planes corresponds to the distance between two (002) crystal planes, providing further confirmation of <0001> as the preferred growth direction for the nanowires.
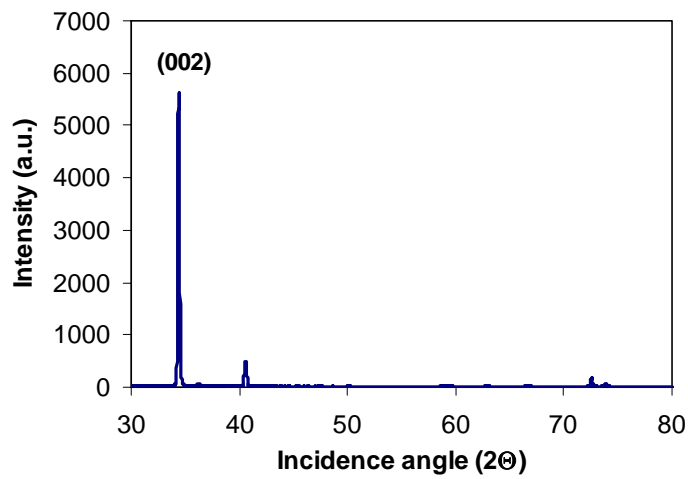
Figure 4.4 – XRD pattern of Au-catalyzed ZnO nanowire arrays grown on Si.
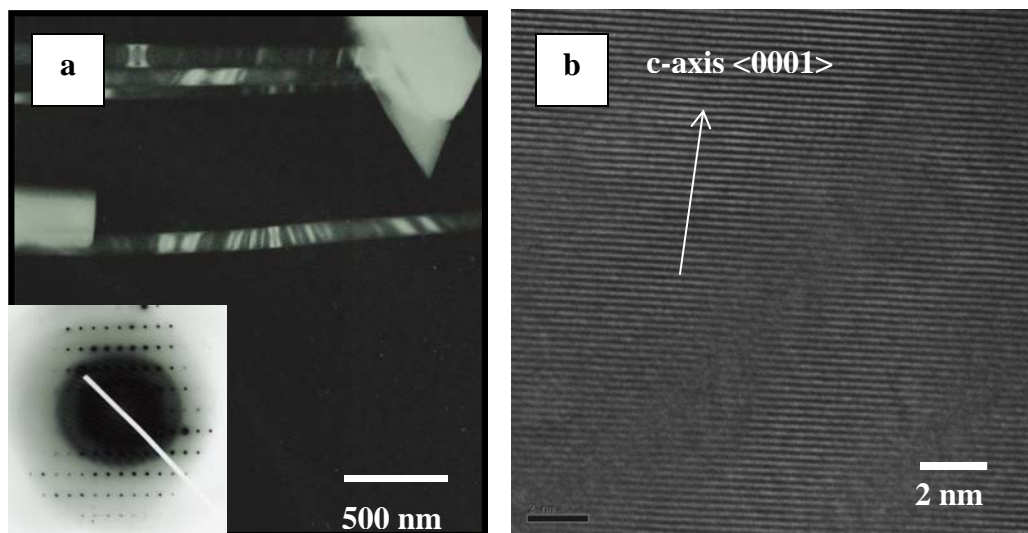
Figure 4.5 – (a) Low-resolution TEM images of individual ZnO nanowires; Inset depicts SAED patterns from a nanowire. (b) High-resolution image of ZnO nanowire lattice planes.

The excellent optical properties of as-grown ZnO nanowires were confirmed through photoluminescence (PL) studies. A typical PL spectrum collected from a ZnO nanowire array sample is shown in Figure 4.6.
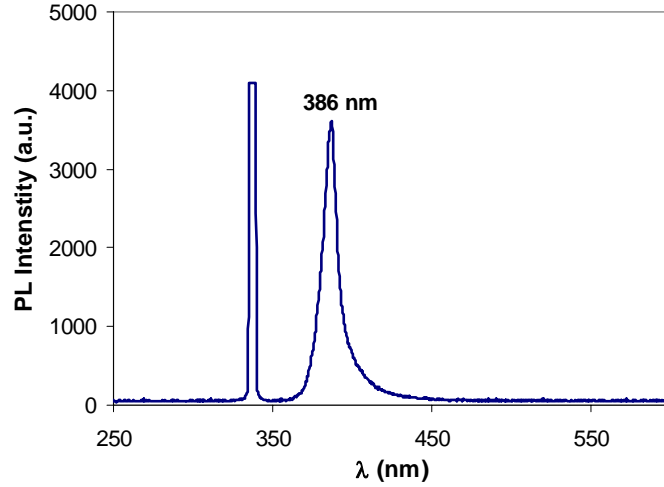
Figure 4.6 – Room-temperature PL spectrum collected from Au catalyzed ZnO nanowire arrays on Si. The 338 nm peak corresponds to the exciting N_2 ion laser while the 386 nm peak is recorded from the ZnO nanowires.

The PL spectra were measured using an N_2-ion laser (338 nm) as the excitation source at room temperature. The measured UV emission peak at 386 nm with a FWHM of ≈ 11 nm from the nanowires corresponds to near band-edge emission. In several previous studies, a broad green emission peak around 520 nm has been commonly observed, attributed to deep-level or trap-state emissions due to oxygen vacancies.[125-127] This peak was not observed in our spectrum, indicating that our nanowires were almost entirely stoichiometric.

4.2.4 Growth Mechanisms

Direct growth on Si generally follows a non-catalytic vapor-solid (VS) mechanism, in which zinc and zinc suboxides condense on the Si surface to form droplets which act as nuclei for ZnO nanowire growth.[102] The growth mechanism for the nanowires on Au on the other hand, follows a vapor-liquid-solid (VLS) mechanism wherein Zn vapor is transported and reacted with the Au catalyst, forming alloy droplets, which provide nucleation sites for ZnO vapors to condense and grow into well-crystallized nanowires.[128] The two mechanisms are pictorially depicted in Figure 4.7. We observed that aligned ZnO nanowires could be grown through a chemical vapor transport process using Zn powder as precursor at temperatures as low at 450 °C. Zn has a relatively low melting point ($\approx$ 420 °C) and a high vapor pressure allowing the nucleation and condensation of highly crystalline one-dimensional nanostructures.
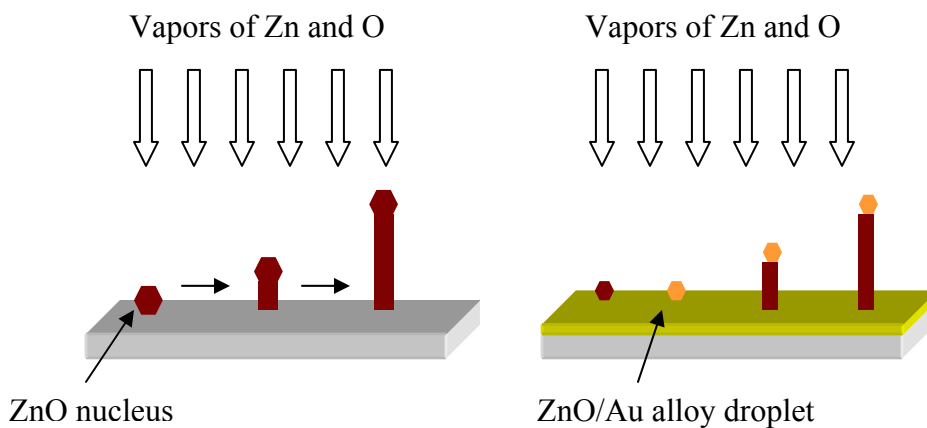
Figure 4.7 – Non-catalytic V-S and catalytic VLS growth mechanisms of ZnO nanowires grown by chemical vapor transport.

4.3 Nanoparticle Electrodes

4.3.1 Outline of the Approach

Even though nanowire arrays of various materials have been routinely synthesized and studied over the last decade, there has been surprisingly little progress in the development of methods for electrically contacting them as grown, i.e., without removing them from the substrate. We conceived a simple technique for achieving electrical contacts to both ends of our nanowire array using an Au catalyst layer as the bottom electrode, and a conducting nanoparticle film as the top electrode. The nanoparticles could potentially be attracted exclusively onto the nanowire arrays within a high electric field. The key aspect of the high field deposition is that the nanowire tips act as electric field concentrators thereby ensuring very high collection efficiencies.

4.3.2 Nanoparticle Generation and Deposition

Ag nanoparticles were generated through an aerosol spray-pyrolysis method. Typically, an aqueous solution of silver nitrate ($AgNO_3$) was sprayed into droplets with an atomizer using a carrier gas flow of 2 slpm (standard liters per minute) N_2. The flow containing the droplets was passed through silica gel dehumidifiers, and then into a tube furnace maintained at 600 °C, to thermally crack the precursor and form nanoparticles. The particles were then positively charged with a home-built unipolar charger and introduced into an electrostatic precipitator containing the substrate with the grown nanowire arrays of ZnO. A high negative electric field (-10 kV/cm) was applied to drive the particle deposition. A schematic diagram of this process is presented in Figure 4.8.
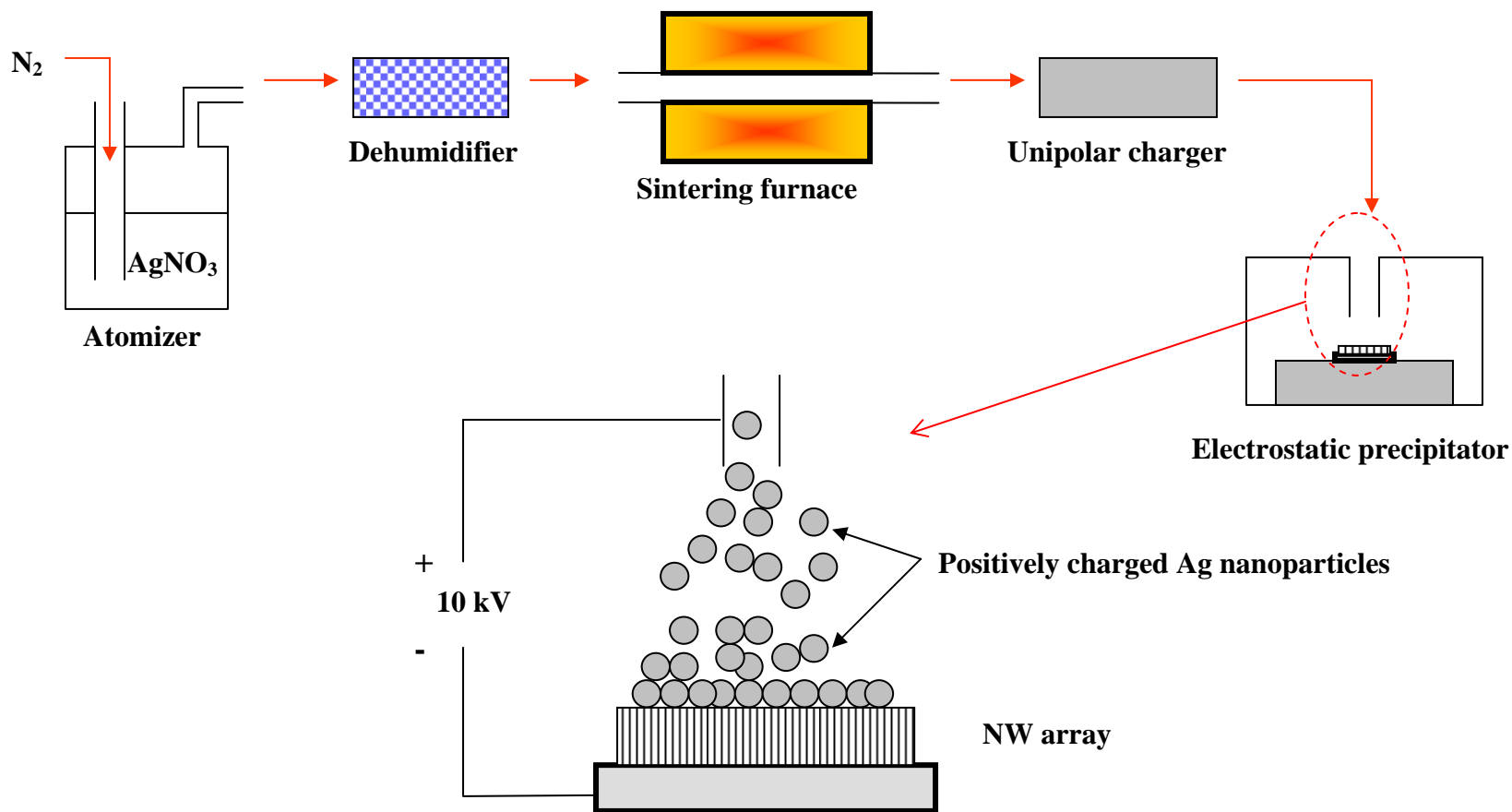
Figure 4.8 – Schematic diagram of Ag nanoparticle generation by aerosol spray-pyrolysis followed by sintering, charging and deposition on a ZnO nanowire array within an electrostatic precipitator

SEM images of Ag nanoparticles deposited on top of the ZnO nanowire array are shown in Figure 4.9. Clearly, the nanoparticles rested on top of the nanowires, bolstering the concept that electrostatic-directed deposition could be a viable approach to make a top contact.
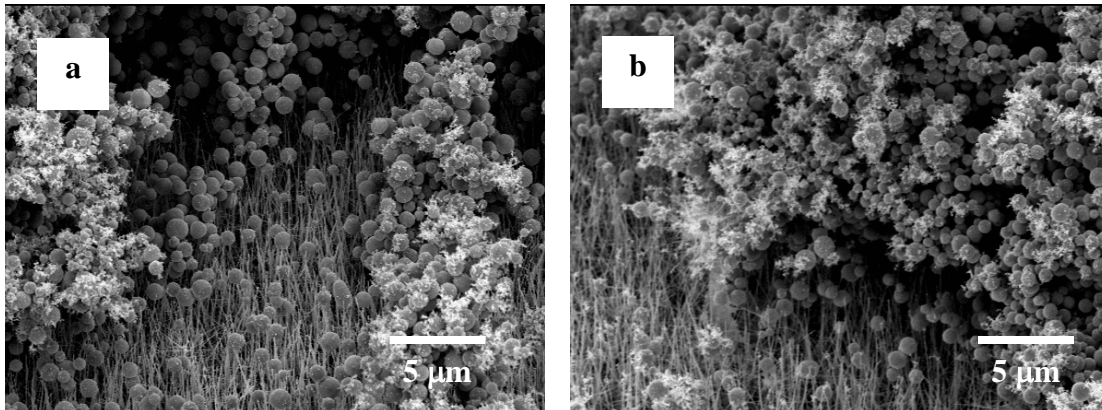
Figure 4.9 – SEM images of Ag nanoparticles resting above the ZnO nanowire array imaged from a 45° perspective.

4.3.3 Gas Sensing Device Design and Fabrication

A suitable design for a gas-sensing device based on aligned ZnO nanowire arrays was conceived at this juncture. Silicon dioxide wafers (1 cm^2) were ultrasonically cleaned in acetone and 4 electrically isolated pads of Cr/Au were deposited through thermal evaporation. A pair of small SiO$_2$ wafers was placed partially covering areas on all 4 Au pads before being loaded into the tube furnace for nanowire growth. The main idea here was to provide an easy electrical access to the bottom of ZnO nanowires grown on each pad. For the top contact, a gold nanoparticle film was chosen primarily because Au resists oxidation and maintains metallic character even at high temperatures. The Au nanoparticle film was deposited through a shadow mask in such a way that it made

contact with two of the four gold pads. A diagram representing the series of steps involved in device fabrication as well as a side view of the device is shown in Figure 4.10.
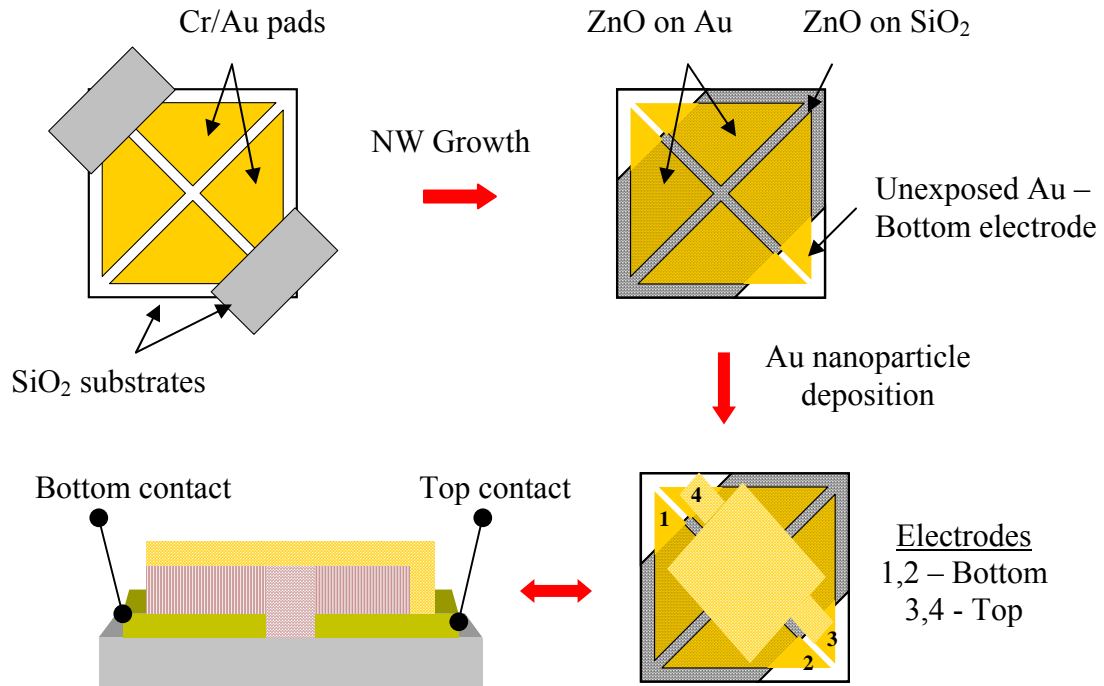
Figure 4.10 – Schematic diagram of gas sensing device fabrication steps. The bottom images represent side and top views of the device.

SEM images of the surface of the device revealed vertically aligned nanowire growth on the gold catalyst pads while the nanowires in the adjacent SiO_2 region were randomly oriented, as seen in Figure 4.11. SEM images of the Au nanoparticle film deposited on top of the nanowires at various stages of deposition are shown in Figure 4.12.
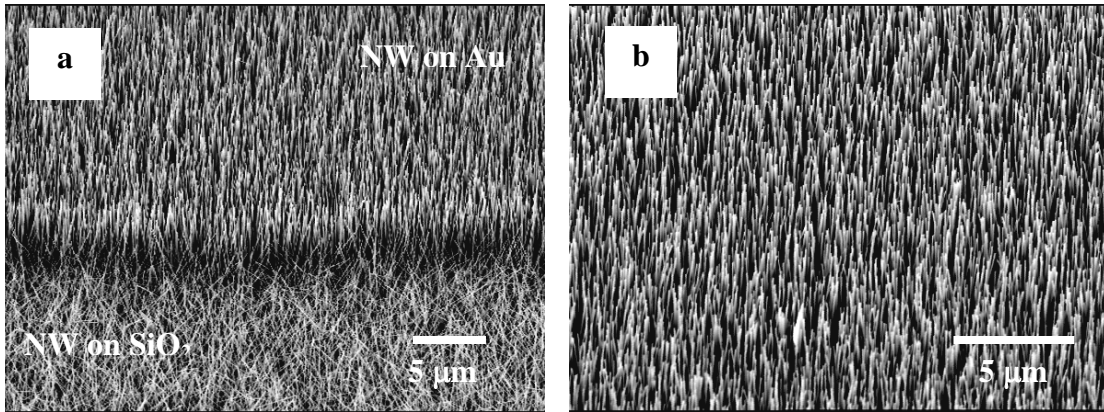
Figure 4.11 – SEM images of gas sensing device sample surface. Vertically aligned nanowire grew on Au catalyst pads while randomly oriented nanowires grew on SiO_2
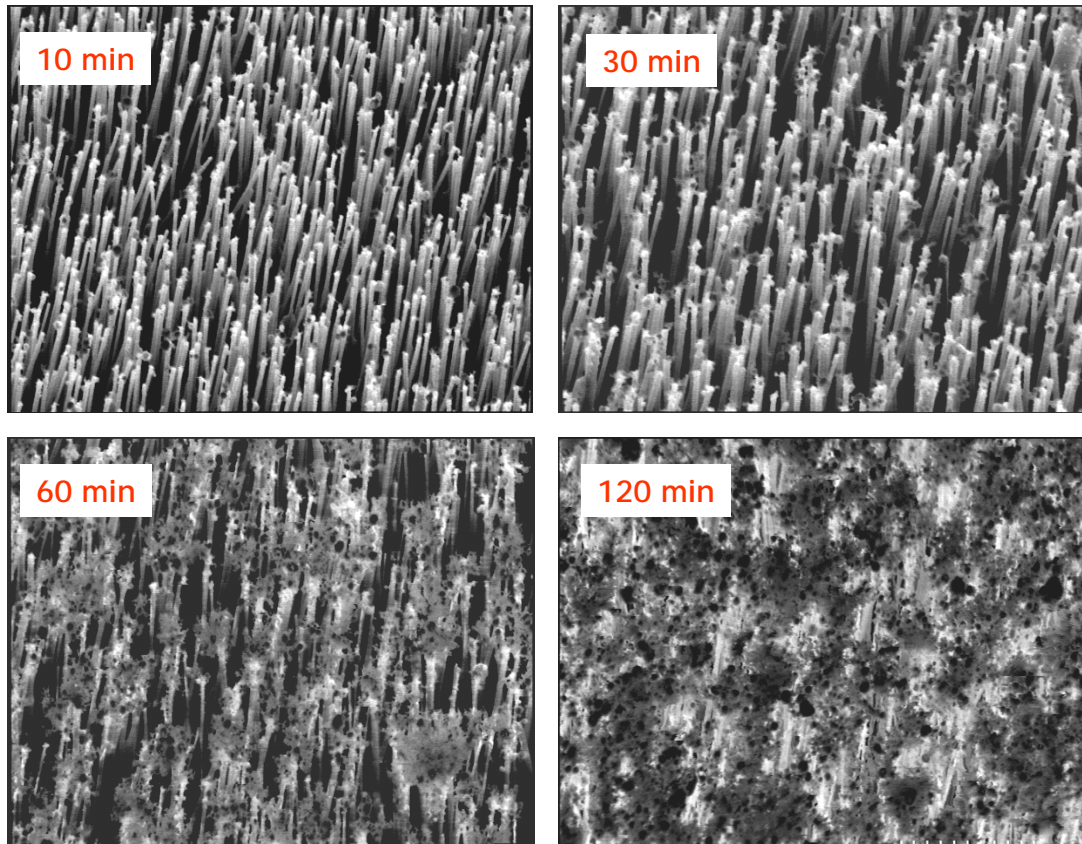
Figure 4.12 – Evolution of Au nanoparticle film top contact at various stages of deposition.

The device was then glued onto a large square package containing pin contacts for electrical connections using a high-temperature adhesive paste (Ceramabond 503; Aremco Products Inc., NY). Wire bonds were attached to all 4 gold pads for electrical measurements. A digital photograph of the device used for further measurements is shown in Figure 4.13.
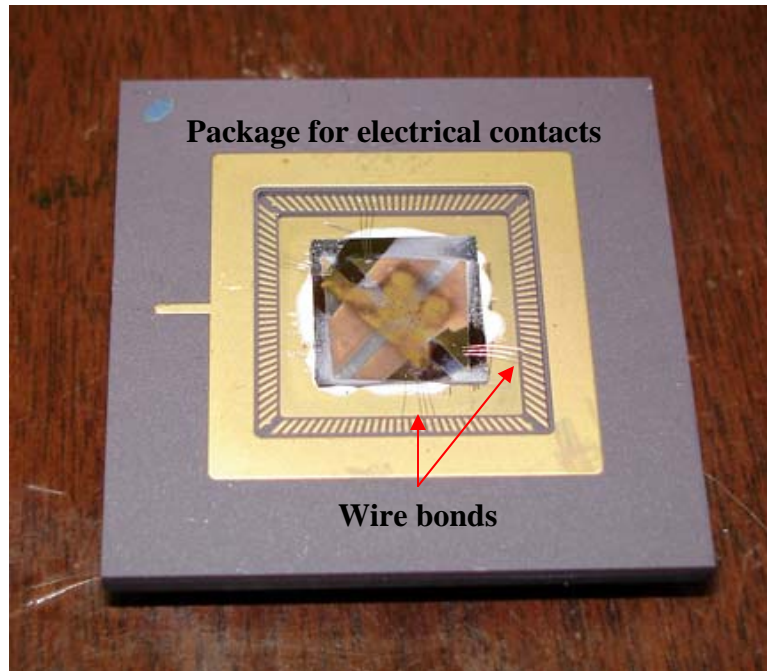
Figure 4.13 – Digital photograph of the nanowire array based gas-sensing device glued to a package containing pin contacts for electrical connections.

4.3.4 Electrical Characterization

A probe station was used to measure resistances between various points on the same contact electrode to verify film continuity, and between the top and bottom contacts to measure the nanowire array resistance. Before nanowire growth, electrical isolation between the various pads of Cr/Au was confirmed. Following nanowire growth and nanoparticle film deposition, both the underlying and overlying Au layers were verified to be conducting ($R_{2pt} < 10\ \Omega$), and there was no visible shorting between the bottom and top electrodes. As mentioned earlier, the Au nanoparticle film was deposited such that it made contact with two of the four gold pads, thereby enabling simple electrical continuity verification. Typically, the device was annealed in air at 300 °C for over 8 h to ensure stability of the electrodes to heat treatment. This is an important step since the gas sensing capabilities of metal oxide sensors in general are effective at such operating temperatures. The contact between ZnO and Au was observed to transition from a Schottky-type contact to an Ohmic contact after heat treatments in air. I-V characteristics of the nanowire array in air were measured and averaged for different bias voltages applied between the two contacts indicating good contact between the nanowires and nanoparticles, as seen in figure 4.14. These results confirmed that the approach to create a top-contact for nanowire arrays using a nanoparticle aerosol source was successful.
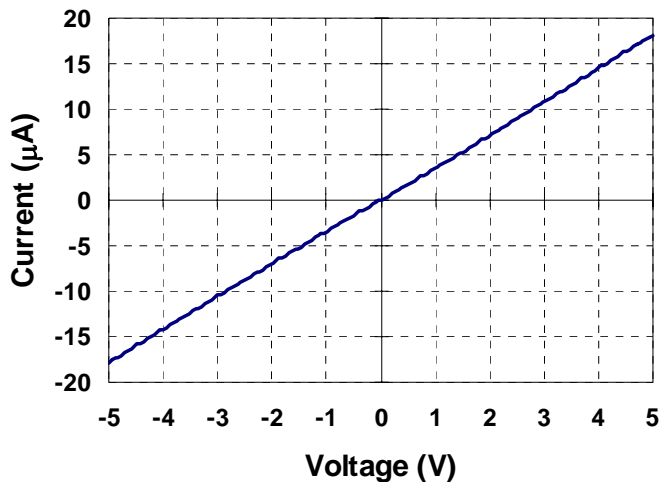
Figure 4.14 – I-V characteristic of the device following repeated heat treatments at temperatures up to 350 °C.

4.4 Gas Sensing Measurements

Several different morphologies of ZnO including thin films, flakes and nanowires have been tested for the detection of gases including ethanol, carbon monoxide, hydrogen sulphide, oxygen, and nitrous oxides.[108,129-133] Due to their very high surface to volume ratio, nanowires present an attractive alternative to thin films for improved gas sensing characteristics, including sensitivity and overall speed of response. In the past, as-grown nanowire arrays could not be used for gas-sensor testing, possibly due to difficulties in achieving a continuous top contact to the nanowires using standard approaches like thermal evaporation, without interfering with the ability of the analytes to interact with the sensing material (nanowires). Our technique for attaching electrodes to nanowire arrays could solve this vexing problem since the nanoparticle film is a porous but electrically continuous electrode, allowing gases to come into contact and adsorb onto the nanowires both from the sides as well as the top.

Fixed temperature responses of the nanowire assembly to pulsed concentrations (10 to 50 ppm) of methanol (CH_3OH) and nitrous oxides (NO/NO_2) were measured at 275 °C and 325 °C. The sensor responses recorded at 325 °C for the two gases are shown in Figures 4.15 and 4.16. As expected, the resistance of the ZnO nanowires increased upon exposure to the oxidizing analyte, NO_x and reduced upon exposure to the reducing analyte, CH_3OH. The sensor response clearly tracks the pulsed input of the analyte. However, the recovery time for the sensor to re-attain its original resistance was somewhat high, possibly due to slow desorption rates. The continuity of the contact layers as well as sensor responses were found to be remarkably stable and reproducible for repeated testing cycles. The sensitivities of the nanowires to varying concentrations of both gases were evaluated and observed to be comparable to an existing ZnO nanowire based sensor (Figures 4.17 and 4.18).[108] While this device is still in a primitive state, it vividly demonstrates the efficacy of our nano-assembly approach.
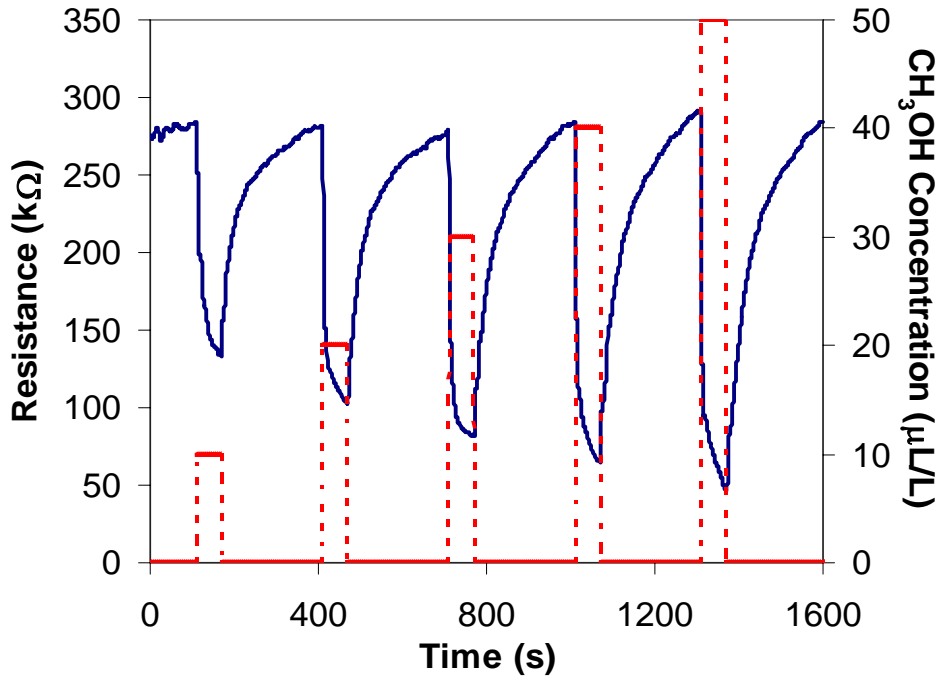
Figure 4.15 – Sensor responses from the nanowire arrays at 325 °C to varying concentration of methanol (10 – 50 ppm).
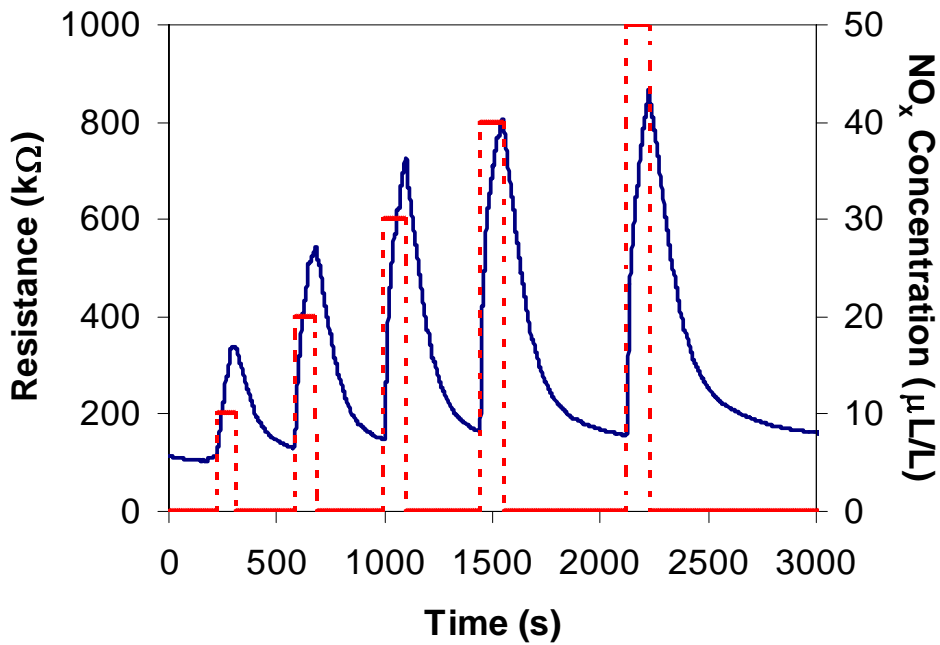
Figure 4.16 – Sensor responses from the nanowire arrays at 325 °C to varying concentration of nitrous oxide (10 – 50 ppm).
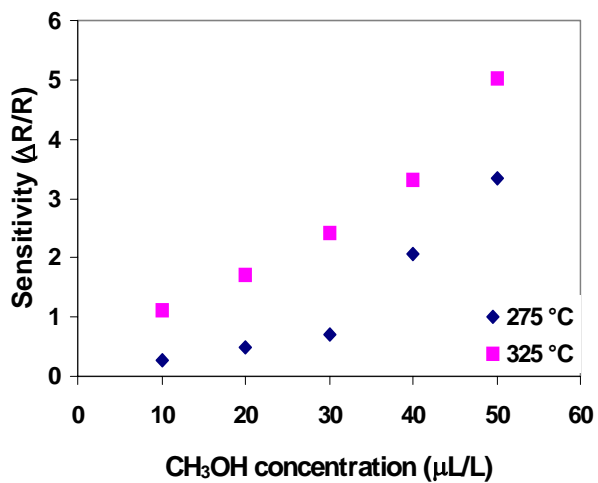
Figure 4.17 – Sensitivity of the nanowire array to methanol, evaluated at 275 and 325 °C.
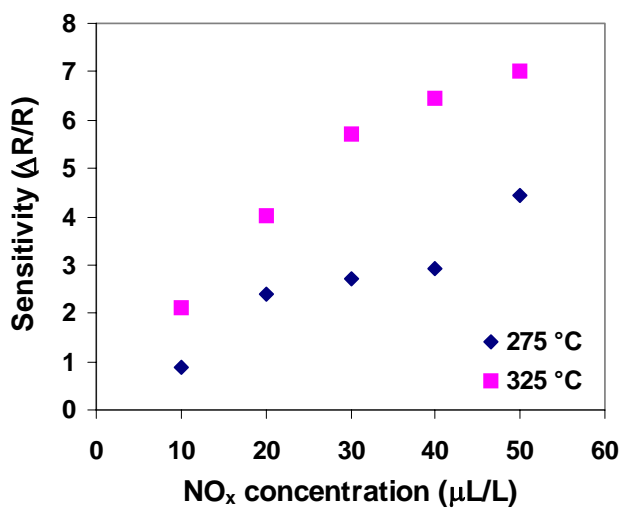
Figure 4.18 – Sensitivity of the nanowire array to nitrous oxide, evaluated at 275 and 325 °C.

4.5 Summary

In summary, we have devised and tested an entirely original, generic approach toward achieving electrical contacts to vertically aligned ZnO nanowire arrays using electrostatic-assisted deposition of Au nanoparticles. The Au nanoparticle electrode was observed to be both mechanically and electrically robust even at high temperatures. This approach of creating a top contact to a vertically aligned nanowire assembly as grown, may be useful for the design and fabrication of electrically driven nanowire-lasers and LEDs. Our first successful application of this nano-architecture was a gas-sensing device, which exhibited high sensitivities to low concentrations (10 ppm to 50 ppm) of both reducing (methanol) and oxidizing (nitrous oxide) gases.

Chapter 5

Conclusions

The ongoing research work on the direct synthesis and integration of one-dimensional nanostructures such as nanotubes (NTs), and nanowires (NWs) into gas sensing device applications has been incredibly stimulating and exciting. The central theme motivating this research topic has been to come up with simple, novel ideas not just for growing 1-D nanostructures but also in ways suitable for their direct incorporation into micro-scale devices. The main advantages of utilizing the processes described in this work would be in the development of more sensitive, highly efficient, miniscule gas sensors operable at appreciably lower powers.

We have developed an elegant process of synthesizing metal oxide NTs on microhotplates using carbon nanotubes (CNTs) as easily removable templates. Significant technical challenges were overcome in achieving direct synthesis of vertically aligned arrays of CNTs not just on microhotplates but also on a wide variety of conductive substrates. The key towards developing this generic process was the utility of a bi-metallic iron/alumina catalyst. The CNTs grown on microhotplates were further coated with SnO_2 and easily removed by annealing, creating SnO_2 NTs, which possessed far superior sensing characteristics in comparison with SnO_2 thin films. In essence, a simple, single-step process involving growth of CNT forests prior to metal oxide deposition considerably improved the sensor's capabilities. In addition, the same process

could now be extended to create NTs of other metal oxides as necessary for application such as electronic noses.

One-dimensional WO_3 NWs have been grown through a direct thermal reconstruction of W thin films within an RF plasma, on various substrates. The growth process, which was based on an existing method, was improvised to substantially reduce the growth temperature to values suitable for operation of microhotplates. In addition to NWs growth, a new hollow square microduct structure was also observed to grow. The parameters influencing the growth process included presence of a reducing agent, an oxygen source and temperature. NW synthesis conditions were optimized on macro-scale substrates before duplication on microhotplates. The WO_3 NWs exhibited better sensing capabilities than a thin film in sensing trace quantities of nitrous oxide. Hence, once again a straightforward process of heat-treating a W thin film in RF Ar/H_2 plasma can create a more efficient gas sensor.

We have also devised a unique, non-destructive approach towards contacting vertically aligned ZnO NWs through electrostatic-directed deposition of conducting nanoparticles. In spite of enormous advancements in NW growth techniques and device fabrications henceforth, research on utilizing NWs as grown has been surprisingly ignored. We successfully conceived and fabricated a highly sensitive gas-sensing device based on aligned ZnO NWs using Au nanoparticles as top contact. We believe that the approach developed in this work is universally applicable to any aligned NW or NT

structure requiring a top contact, and hence may be crucial in developing future nanoelectronic devices such as electrically driven nano-LEDs and lasers.

The key to achieve success in one-dimensional nanotechnologies lies in assembly. While synthesis techniques and capabilities continue to expand rapidly, progress in controlled assembly has been sluggish due to numerous technical challenges. In other words, cultivating the art of integrating nanostructures with suitable connectivity precisely and controllably in areas where one desires and not elsewhere, is a subject of paramount importance that needs to be addressed by future researchers. The current state-of-the-art approach to practical nano-devices is directed assembly using some form of lithography. However, although remarkable in proving several design concepts, these approaches still remain complex and suffer from prohibitively high costs. We have succeeded partially in reducing complexities to some extent by combining synthesis and assembly of nanostructures on the same platform. Apart from assembly, accurate control of size uniformity and dimensionality, as well as thorough understanding of the fundamental properties of nanostructures and their interfaces with other materials will be certainly necessary to translate nanoscale research into useful functional applications in future.

Appendix A

Avenues for Future Research

A1. Micro-calorimeters

A micron-scale differential scanning calorimeter is a device that consists of a suspended rectangular microhotplate with sample and reference zones at either end, each equipped with a microheater for temperature control.[134] The temperature difference between the two zones is measured using a thermopile which is essentially a series of polysilicon/metal junctions that alternate between the two zones. The operation of this micro-calorimeter as a sensor is based on the fact that chemical processes involve absorption or release of heat, which translates into a temperature change. Hence if a catalyst or any chemically reactive material is selectively deposited on the sample zone, and both sample and reference zones are heated uniformly to a certain temperature at which the material on the sample zone begins to interact with the surrounding gases, this results in a temperature difference between the two zones. Optical images of a 6-element array of micro-calorimeters and an individual micro-calorimeter device, along with a schematic diagram of device construction are shown in Figure A1.
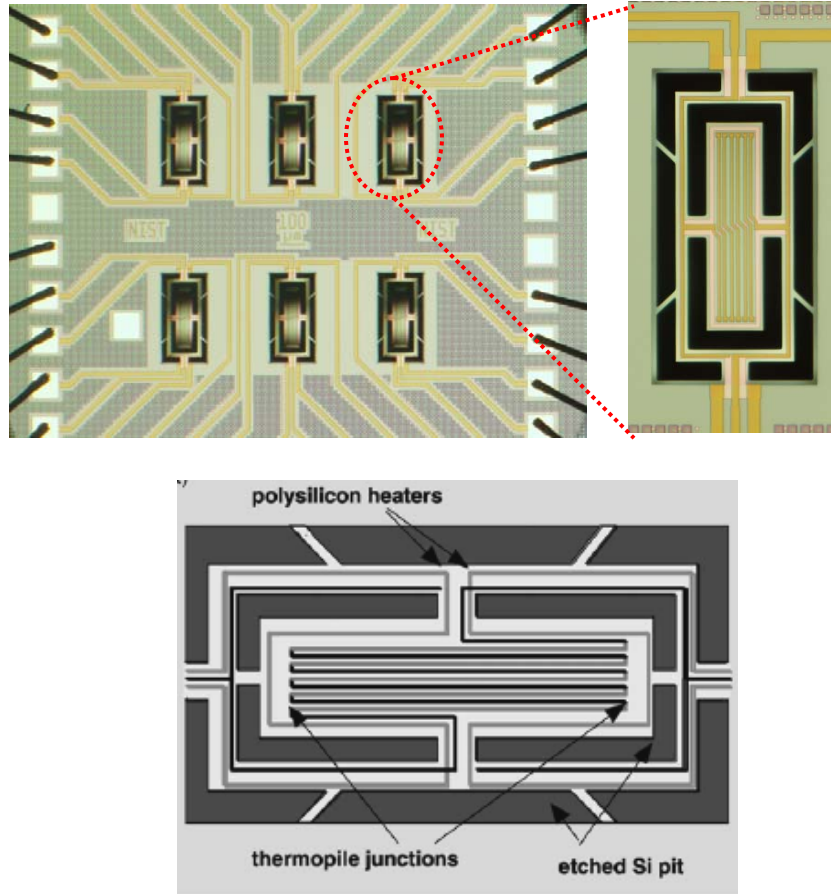
Figure A1 – Optical images of a 6-element array of micro-calorimeters integrated on a chip and a closer look at an individual micro-calorimeter are shown on top. A schematic diagram of the device configuration is shown below.

In differential scanning calorimetry (DSC), the operating system is provided with a feedback such that compensating power changes are applied to the sample zone in order to maintain a zero temperature difference with the reference zone, and the compensating power gives rise to an electrical signal. In a micro-calorimeter, rapid thermal changes are possible and temperature differences can be sensitively measured.

We have grown high-density forests of CNTs on one zone of the micro-calorimeter (sample zone) by specifically heating one side of the device. The same process conditions that resulted in successful growth of CNT forests on microhotplates were utilized. SEM images of the CNT forests grown on a micro-calorimetric device are shown in Figure A2. At present, the performance of the thermopile has been observed to degrade during CNT growth. Further optimization of process conditions will be necessary in future for successful utilization of the micro-calorimeter for gas-sensing purposes.
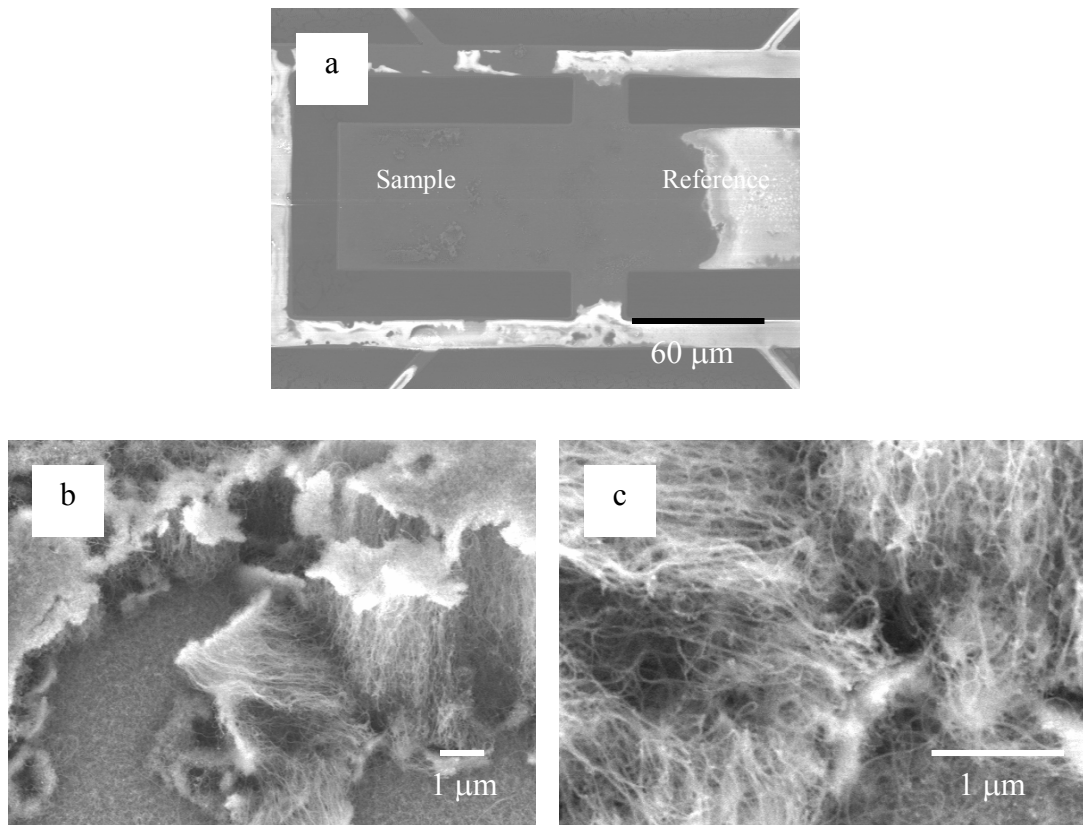
Figure A2 – SEM images of CNTs grown on a micro-calorimeter device. (b) and (c) represent CNT forests grown on the sample zone.

A2. Carbon Nanotube Array based Gas Ionization Sensors

Electrical breakdown of gases and gas mixtures is an effective method of gas identification since the ionization potentials are unique for each gas. The main drawbacks of gas-ionization sensors include bulky architecture, high power consumption and risky high-voltage operation. A possible solution to overcome these problems is to employ nanostructures with high aspect ratios such as CNT arrays to generate high electric fields at relatively low applied voltages. Miniaturized gas ionization sensors based on CNT arrays have been fabricated and tested for both gas-sensing and pressure-sensing applications.[135-137] However, even these reports employed relatively high voltages (a few hundred of volts) to achieve gas ionization, and hence may not be useful as practical devices.

The key towards developing a practical, tabletop gas-ionization sensor capable of detecting and measuring gas concentrations is to control the gap between opposing electrodes to distances of the order of a few micrometers. Since electric field scales inversely with distance, smaller voltages can be employed to initiate electrical breakdown for smaller inter-electrode gaps. We have devised a new approach towards fabricating such a device, a schematic of which is shown in Figure A3.
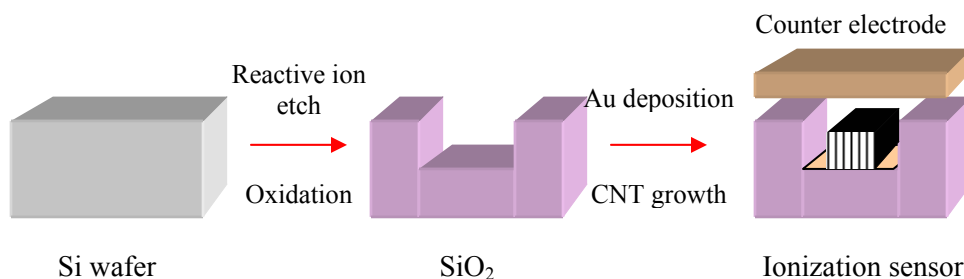
Figure A3 – Schematic of steps involved in fabrication of CNT-array based gas-ionization sensor. Both trench depth and CNT lengths can be controlled to precisely adjust inter-electrode gap through this approach.

Reactive ion etching is a commonly employed etching technique widely used in microfabrication technologies, and can be used to create trenches of varying depths on a silicon wafer with great precision. CNT lengths can also be well controlled by varying the growth time and thus the inter-electrode gap can be reduced to values under ten micrometers. Efforts are currently underway in fabricating and testing an ionization sensor using this approach for both gas and pressure sensing applications.

A3. Mechanical Properties of ZnO Nanowires

It is well known that the crystallographic surface layers experience in-plane stresses to reduce their configuration energy.[138] This surface effect is even more dramatic in low-dimensional nanostructured materials like nanowires (NW) for example where the stress surface is enhanced as a result of the large surface-to-volume ratio. It has been shown that large tensile surface-stress even induce crystallographic phase transformations at very small size (below 4 nm^2) due to the compressive stress-strain built in the wire's core.[139] To accommodate this surface stress the outer most layers relax and modify their lattice

constants. As a result the mechanical response of nanowires is different compared to those of their bulk counterparts.

We have investigated the surface stress effect on the elasticity of ZnO NWs with diameters in the range 35 nm to 80 nm on both directions, parallel and perpendicular to the [0001] axis of the wire. The radial elastic modulus and longitudinal shear modulus have been calculated from the measured normal and tangential contact stiffness of the contact between an atomic force microscope (AFM) probe and the NWs' surface. An increase in the radial elastic modulus was found for NWs with diameter around 36 nm whereas for NWs with diameter around 50 nm or larger the values are close to those measured for bulk ZnO single crystal.[140] A significant increase, more than double the bulk value, has been found for the shear modulus of 36 nm NWs. This is because in the shear measurements the mechanical response is driven almost entirely from the outer shell-part of the NWs whereas in the indentation-type measurements the radial elastic modulus includes large contributions from the wire's core. The measurements have been made on single-crystal [0001] oriented ZnO NWs and contact geometry implications were carefully considered in interpreting the measurements. A detailed discussion on measurement techniques and analysis of results is beyond the scope of this thesis.

A4. Epitaxial Growth of Nanowires

Heteroepitaxial growth of ZnO nanowires on various substrates is vital for the development of functional UV optoelectronic devices such as LEDs, lasers and detectors.[104] Optoelectronic devices generally require highly crystalline materials with

minimal defects. One possible approach for preserving crystalline order in thin semiconductor films is to grow them epitaxially on lattice-matched substrates.[141] Apart from Si and SiO$_2$, we have succeeded in growing ZnO nanowires on other substrates such as c-plane sapphire, single-crystalline aluminum nitride (AlN), diamond coated Si, and nanocrystalline titania (TiO$_2$). Typical surface morphologies of nanowires grown on these substrates are shown in Figure A4. Further optimization of growth process conditions will be necessary for rational synthesis of aligned nanowires with consistency on these substrates for novel optoelectronic applications.
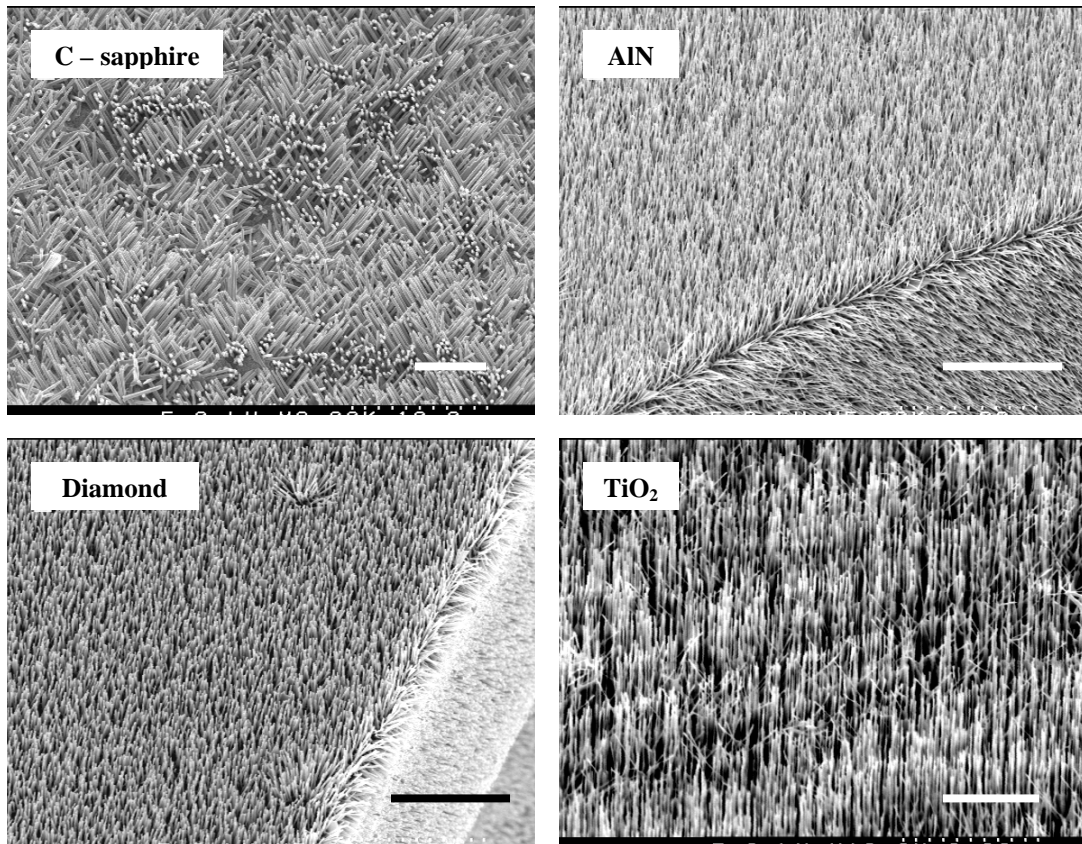
Figure A4 – Epitaxial growth of ZnO nanowires on various substrates. Scale bars represent 5 μm.

Appendix B

Characterization Techniques

B1. Scanning Electron Microscopy

A scanning electron microscope (SEM) is an instrument most commonly used in surface analysis. Typically, electrons are thermionically emitted from a heated tungsten filament and focused using condenser lenses into a beam with very fine spot size. The electron beam, which normally has energies ranging from a few thousand to 50 keV, impinges on the sample surface whereby the primary electrons transfer their energy inelastically to the atomic electrons within the lattice structure of the sample. Through random scattering events, this primary beam spreads through the sample resulting in a distribution of electrons that reflect back from the sample. Usually, the electrons with lowest energy (secondary electrons) are captured by a detector consisting of a scintillator-photomultiplier combination and converted into a surface image using a cathode-ray tube (CRT). Great depth of focus gives SEMs the possibility of imaging non-planar surfaces with good resolutions (≈ 50 Å) in all three dimensions.

B2. Transmission Electron Microscopy

A transmission electron microscope (TEM) is an instrument used to obtain structural information from extremely thin specimens that are capable of transmitting electrons through them. Typically, TEM imaging requires extensive sample preparation steps. For

studying one-dimensional nanostructures, the samples are usually removed from their original substrates and dispersed in ethanol, a small portion of which is applied and dried on a TEM grid. Unlike the SEM, the electron beam energies in a TEM are very high, ranging between hundreds of keV to 1 MeV, in order to ensure sufficient transmission of electrons after impingement through the sample. The primary electron beam interacts with the sample after which, it travels through a column and produces an image on a fluorescent screen, on a photographic plate or on a post-column charge coupled device (CCD). Apart from imaging, elastically scattered electrons with small diffraction angles can be used to determine the structure of the sample using selected area electron diffraction (SAED). The main advantage of using a TEM to analyze 1-D nanostructures lies in its ability to resolve lattice spacings of materials with remarkable precision.

B3. X-Ray Diffraction

X-ray diffraction (XRD) is a widely used technique to characterize crystalline materials. Typically, x-rays generated from a source impinge on a sample over a range of incidence angles, which are scattered due to interaction with atoms within the sample's crystal lattice. The scattered waves interfere with the waves coming from neighboring atoms, and their intensities are captured and plotted as a function of the incidence angle. The spacings between crystal lattices can then be calculated using Bragg's law of diffraction. XRD provides useful structural information such as crystallinity, orientation and composition of the sample.

B4. Photoluminescence (PL)

PL spectroscopy is a non-destructive method of studying electronic structure of materials. In a typical setup, a highly coherent laser beam is directed on the sample, which transfers its energy onto the electrons in the sample, exciting them in the process. These photo-excited electrons dissipate their energy in the form of light, which is collected using a detector. The intensity of the emitted light is collected as a function of the wavelength, which may then be used to characterize various material properties including band-gap determination, impurity levels and defects, and recombination mechanisms. In the case of semiconducting MO_x NWs such as ZnO, PL spectroscopy is a very useful technique for evaluating the optical quality of the material.

Appendix C

Supplementary Information

C1. Microhotplate Cleaning Procedure

Microhotplate devices are extremely fragile and need careful attention during cleaning procedures. Typically, the package containing the microhotplates are loaded onto a sputter chamber equipped with a gridded DC ion source (graphite rods) and pumped down to $\approx 10^{-7}$ torr. Argon is then introduced into the chamber and an Ar ion beam is quasi-neutralized via an external tungsten filament. The samples are then sputter cleaned using the beam, while being constantly swiveled in order to eliminate the formation of "hot spots". Re-deposition is also minimized because of the glancing incidence of the beam on the sample surface. The sputter-cleaning procedure usually lasts for ≈ 3 minutes.

C2. Nanostructure Synthesis Procedures

C2.1 Tin Oxide Nanotubes on Microhotplates

- Clean microhotplate arrays using Ar-ion beam

- Prepare bi-metallic catalyst solution (aqueous solution consisting equal proportions of iron and aluminum nitrates)

- Suspend and spin coat catalyst solution on the microhotplate package

- Load the microhotplate package onto fixture that delivers metered flows of carrier gases and carbon precursor

- Anneal specific elements of the array at 600 °C in pure Ar and H_2 for 5 minutes

- Grow CNTs at 600 °C in a mixture of Ar, H_2 and C_2H_2 for 5 minutes

- For SnO_2 growth, load the microhotplate package into a high-vacuum CVD chamber

- Allow tin precursor to equilibrate above the elements before heating each element specifically to 375 °C

- Carry out SnO_2 deposition for 10-20 seconds

- For SnO_2 NT creation, anneal microhotplates in air at 450 °C for 6-8 h

C2.2 WO_x Nanowires on Microhotplates

- Obtain clean microhotplate array consisting of a W thin film

- Load microhotplate package into a low-pressure CVD chamber

- Pump CVD chamber down to 5 torr

- Introduce metered flows of Ar and H_2 gases

- Heat specific elements of the microhotplate to 550 °C

- Initiate RF-plasma within chamber and maintain for 5-10 minutes

- Turn off RF-plasma and bring microhotplate back to room temperature

C2.3 ZnO Nanowire-array Based Gas Sensor

- Deposit isolated pads of Cr/Au on a clean SiO_2 substrate

- Place physical masks over the substrate

- Place the substrate and about 1 g of commercial Zn powder in an alumina boat and load into a tube furnace

- Carry out NW growth at 550 °C for 1-2 h in N_2 and O_2 at atmospheric pressure

- Allow substrates to cool down to room temperature and place within electrostatic precipitator

- Deposit Au nanoparticles generated by spray pyrolysis such that it contacts 2 of the 4 Au pads

- Verify electrical continuity of individual Au pads as well as Au nanoparticle film after deposition

- Anneal the sample at 350 °C for 8 h

Bibliography

1. National Nanotechnology Initiative (NNI) URL: www.nano.gov/index.html, http://www.nano.gov/html/about/funding.html

2. National Institute of Health (NIH) Roadmap for Medical Research URL: http://nihroadmap.nih.gov/nanomedicine/index.asp

3. Duan X., Huang Y., Agarwal R., and Lieber C. M., *Nature*, **421**, 241 (2003)

4. Klein D. L., Roth R., Kim A. K. L., Alivisatos A. P., and McEuen P. L., *Nature*, **389**, 699 (1997)

5. Pettersson H., Baath L., Carlsson N., Seifert W., and Samuelson L., *Appl. Phys. Lett.*, **79**, 78 (2001)

6. Shipway A. N., Katz E., and Willner I., *ChemPhysChem*, **1**, 18 (2000)

7. Phillips J., *J. Appl. Phys.*, **91**, 4590 (2002)

8. Brattain W. H., and Bardeen J., *Bell. Syst. Tech. J.*, **32**, 1 (1953)

9. Seiyama T., Kato A., Fujishi K., and Nagatani M., *Anal. Chem.*, **34**, 1502 (1962)

10. Taguchi N., Jpn. Patent 45-38200 (1962)

11. Figaro Inc. URL: www.figarosensor.com

12. Mandelis A., and Christofides C., "Physics, Chemistry, and Technology of Solid State Gas Sensor Devices", *John Wiley and Sons* (1993)

13. International Sensor Technology Inc. URL: www.intlsensor.com

14. Moseley P. T., *Meas. Sci. Technol.*, **8**, 223 (1997)

15. Kennedy M., *Doctoral Dissertation*, Universität Duisburg-Essen (2004)

16. Göpel W., Jones T. A., Kleitz M., Lundstrom J., and Seiyama T., *Sensors*, **Vol. 2** Part I (1991)

17. Göpel W., and Schierbaum K. D., Sens. Act. B, 26, 1 (1995)

18. Simon I., Bârson N., Bauer M., and Weimar U., *Sens. Act. B*, **73**, 1 (2001)

19. Di Natale C., Macagnano A., Davide F., D'Amico A., Paolesse R., Boschi T., Faccio M., and Ferri G., *Sens. Act. B*, **44**, 521 (1997)

20. Mitrovics J., Ulmer H., Weimar U., and Göpel W., *Acc. Chem. Res.*, **31**, 307 (1998)

21. Gardner J. W., and Bartlett P. N., *Meas. Sci. Technol.*, **11**, 1087 (2000)

22. Freund M. S., and Lewis N. S., *Proc. Nat. Acad. Sci.*, **92**, 2652 (1995)

23. Chung W. Y., Lim J. W., Lee D. D., Miura N., and Yamazoe N., *Sens. Act. B*, **64**, 118 (2000)

24. Sakai G., Baik N. S. Miura N., and Yamazoe N., *Sens. Act. B*, **77**, 116 (2001)

25. Dieguez A., Romano-Rodriguez A., Morante J. R., Weimar U., Schweizer-Berberich M., and Gopel W., *Sens. Act. B*, 31, 1 (1996)

26. Taliercio T., Dilhan M., Massone E., Gué A. M., Fraisse B., and Foucaran A., *Thin Solid Films*, 255, 310 (1995)

27. Kolmakov A., Zhang Y., Cheng G., and Moskovits M., *Adv. Mater.*, **15**, 997 (2003)

28. Kong J., Franklin N. R., Zhou C., Chapline M. G., Peng S., Cho K., and Dai H., *Science* **287**, 622 (2000)

29. Comini E., Faglia G., Sberveglieri G., Pan Z., Wang Z. L., *Appl. Phys. Lett.*, **81**, 1869 (2002)

30. Martinez C. J., Hockey B., Montgomery C. B., and Semancik S., *Langmuir*, **21**, 7937 (2005)

31. Rao C. N. R., Deepak F. L., Gundiah G., and Govindaraj A., *Prog. Solid State Chem.*, **31**, 5 (2003)

32. Xia Y., Yang P., Sun Y., Wu Y., Mayers B., Gates B., Yin Y., Kim F., and Han Y., *Adv. Mater.*, **15**, 353 (2003)

33. Law M., Goldberger J., and Yang P., *Annu. Rev. Mater. Res.*, **34**, 83 (2004)

34. Iijima S., *Nature*, **354**, 56 (1991)

35. Baughman R. H., Zakidov A. A., and de Heer W. A., *Science*, **297**, 787 (2002)

36. Fan S., Chapline M. G., Franklin N. R., Tombler T. W., Cassell A. M., and Dai H., *Science*, **283**, 512 (1999)

37. Bonard J. -M., Salvetat J. -P., Stockli T., Forro L., and Chatelain A., *Appl. Phys. A*, **69**, 245 (1999)

38. Bachtold A., Hadley P., Nakanishi T., and Dekker C., *Science*, **294**, 1317 (2001)

39. Kreupl F., Graham A. P., Duesberg G. S., Steinhögl W., Liebau M., Unger E., and Hönlein W., *Microelec. Engg.*, **64**, 399 (2002)

40. Biercuk M. J., Llaguno M. C., Radoslavljevic M., Hyun J. K., Johnson A. T., and Fischer J. E., *Appl. Phys. Lett.*, **80**, 2767 (2002)

41. Zhang M., Atkinson K. R., and Baughman R. H., *Science*, **306**, 1358 (2004)

42. Li W., Liang C., Qiu J., Zhou W., Han H., Wei Z., Sun G., and Xin Q., *Carbon*, **40**, 791 (2002)

43. An K. H., Kim W. S., Park Y. S., Moon J. -M., Bae D. J., Lim S. C., Lee Y. S., and Lee Y. H., *Adv. Func. Mater.*, **11**, 387 (2001)

44. Kong J., Franklin N. R., Zhou C., Chapline M. G., Peng S., Cho K., and Dai H., *Science*, **287**, 622 (2000)

45. Balavoine F., Shultz P., Richard C., Mallouh V., Ebbesen T. W., and Mioskowski C., *Angew. Chem. Int. Ed.*, **38**, 1912 (1999)

46. Li S., Yu Z., Rutherglen C., and Burke P. J., *Nano Lett.*, **4**, 2003 (2004)

47. Dresselhaus M. S., Dresselhaus G., and Avouris Ph. (Eds.), *Topics in Applied Physics*, **80**, Springer-Verlag (2001)

48. Meyyappan M. (Ed.), *"Carbon Nanotubes: Science and Applications"*, CRC Press (2005)

49. Baker R. T. K., Harris P. S., *"Formation of Filamentous Carbon in Chemistry and Physics of Carbon 14"*, Marcel Dekker New York (1978)

50. Sinnott S. B., Andrews R., Qian D., Rao A. M., Mao Z., Dickey E. C., and Derbyshire F., *Chem. Phys. Lett.*, **315**, 25 (1999)

51. Tenne R., Margulis L., Genut M., and Hodes G., *Nature*, **360**, 444 (1992)

52. Rothschild A., Cohen S. R., and Tenne R., *Appl. Phys. Lett.*, **75**, 4025 (1999)

53. Nath M., and Rao C. N. R., *J. Am. Chem. Soc.*, **123**, 4841 (2001)

54. Zhu Y. Q., Hsu W. K., Kroto H. W., and Walton D. R. M., *Chem. Commun.*, **21**, 2184 (2001)

55. Satishkumar B. C., Govindaraj A., Vogl E. M., Basumallick L., and Rao C. N. R., *J. Mater. Res.*, **12**, 604 (1997)

56. Zhang Y., Liu J., He R., Zhang Q., Zhang X., and Zhu J., *Chem. Phys. Lett.*, **360**, 579 (2002)

57. Rao C. N. R., Satishkumar B. C., and Govindaraj A., *Chem. Commun.*, **16**, 1581 (1997)

58. Sun Z., Yuan H., Liu Z., Han B., and Zhang X., *Adv. Mater.*, **17**, 2993 (2005)

59. Dai H., Wong E. W., Lu Y. Z., Fan S., and Lieber C. M., Nature, 375, 769 (1995)

60. Han W., Fan S., Li Q., Liang W., Gu B., and Yu D., *Chem. Phys. Lett.*, **265**, 374 (1997)

61. Han W., Fan S., Li Q., Gu B., Zhang X., and Yu D., *Appl. Phys. Lett.*, **71**, 2271 (1997)

62. Suehle J., Cavicchi R.E., Gaitan M., and Semancik, S., *IEEE Electron Device Lett.*, **14**, 118 (1993)

63. Gaitan M., Suehle J. S., Cavicchi R. E. and Semancik S., *U.S. Patent #5464966* (1994)

64. Afridi M. Y., Suehle J. S., Zaghloul M. E., Berning D. W., Hefner A. R., Cavicchi R. E., Semancik S., Montgomery C. B., and Taylor C. J., *IEEE Sensors*, **2**, 644 (2002)

65. DiMeo F., Cavicchi R. E., Semancik S., Suehle J. E., Tea N. H., Small J., Armstrong J. T., and Kelliher J. T., *J. Vac. Sci. Technol. A*, **16**, 131 (1998)

66. Cavicchi R. E., Semancik S., DiMeo F., and Taylor C. J., *J. Electroceram.*, **9**, 155 (2003)

67. Panchapakesan B., Cavicchi R., Semancik S., and DeVoe D. L., *Nanotechnology*, **17**, 415 (2006)

68. Meier D. C., Taylor C. J., Cavicchi R. E., White E., Ellzy M. W., Sumpter K. B., and Semancik S., *IEEE Sensors*, **5**, 712 (2005)

69. Delzeit L., Nguyen C. V., Chen B., Stevens R., Cassell A., Han J., and Meyyappan M., *J. Phys. Chem. B*, **106**, 5629 (2002)

70. Kind H., Bonard J. -M., Emmenegger C., Nilsson L. -O., Hernadi K., Maillard-Schaller E., Schlapbach L., Forró L., and Kern K., *Adv. Mater.*, **11**, 1285 (1999)

71. Ng H. T., Chen B., Koehne J. E., Cassell A. M., Li J., Han J., and Meyyappan M., *J. Phys. Chem. B*, **107**, 8484 (2003)

72. Wang B., Liu X., Liu H., Wu D., Wang H., Jiang J., Wang X., Hu P., Liu Y., and Zhu D., *J. Mater. Chem.*, **13**, 1124 (2003)

73. Talapatra S., Kar S., Pal S. K., Vajtai R., Ci L., Victor P., Shaijumon M. M., Kaur S., Nalamasu O., and Ajayan P. M., *Nature Nanotechnology*, **1**, 112 (2006)

74. Han Z. H., Yang B., Kim S. H., and Zachariah M. R., *Nanotechnology*, **18**, 105701 (2007)

75. El-Shereafy E., Abousekkina M. M., Mashaly A., El-Ashry M., *J. Radioanal. Nucl. Chem.*, **237**, 183 (1998)

76. Dai H. J., *Acc. Chem. Res.*, **35**, 1035 (2002)

77. Nakatsuji H., Matsuzaki Y., and Yonezawa T., *J. Chem. Phys.*, **88**, 5759 (1988)

78. Murase S., Nakayama S., Yamada Y., Shimamura K., Tezuka M., Shiga N., Watanabe K., and Kobayashi N., *IEEE Trans. Magnetics*, **32**, 2937 (1996)

79. Tersoff J., *Appl. Phys. Lett.*, **74**, 2122 (1999)

80. Tzeng Y., Chen Y., and Liu C., *Diamond Relat. Mater.*, **12**, 774 (2003)

81. Cox P. A., *Transition Metal Oxides*, Clarendon Press, Oxford (1995)

82. Shaver P. J., *Appl. Phys. Lett.*, **11**, 255 (1967)

83. Meixner H., Gerblinger J., Lampe U., and Fleischer M., *Sens. Actuators B*, **23**, 163 (2000)

84. Sberveglieri G., Depero L., Groppelli S., and Nelli P., *Sens. Actuators B*, **26-27**, 89 (1995)

85. Solis J. L., Hoel A., Kish L. B., Sauko S., Lantto V., and Granqvist C. G., *J. Am. Chem. Soc.*, **84**, 1504 (2001)

86. Moulzolf S., Ding S., and Lad R., *Sens. Actuators B*, **77**, 375 (2001)

87. Tamaki J., Zhang Z., Fujimori K., Akiyama M., Harada T., Miura N., and Yamazoe N., *J. Electrochem. Soc.*, **141**, 2207 (1994)

88. Lee D. -S., Lim J. -W., Lee S. -M., Huh J. -S., and Lee D. -D., *Sens. Actuators B*, **64**, 31 (2000)

89. Sanrato C., Odziemkowski M., Ulmann M., and Augustynski J., *J. Am. Chem. Soc.*, **123**, 10639 (2001)

90. Granqvist C. G., *Sol. Energy Mat. Sol. Cells*, **60**, 201 (2000)

91. Baeck S. H., Choi K. S., Jaramillo T. F., Stucky G. D., and McFarland E. W., *Adv. Mater.*, **15**, 1269 (2003)

92. Lee Y. H., Choi C. H., Jan Y. T., Kim E. K., Ju B. K., Min N. K., and Ahn J. H., *Appl. Phys. Lett.*, **81**, 745 (2002)

93. Gu G., Zheng B., Han W. Q., Roth S., and Liu J., *Nano Lett.*, **2**, 849 (2002)

94. Zhou J., Xu N. S., Deng S. Z., Chen J., She J. C., and Wang Z. L., *Adv. Mater.*, **15**, 1835 (2003)

95. Liu J., Zhao Y., Zhang Z., *J. Phys. Cond. Matter*, **15**, 453 (2003)

96. Vaddiraju S., Chandrasekaran H., and Sunkara M., *J. Am. Chem. Soc.*, **125**, 10792 (2003)

97. Zhou J., Ding Y., Deng S. Z., Gong L., Xu N. S., and Wang Z. L., *Adv. Mater.*, **17**, 2107 (2005)

98. Okuyama F., *J. Cryst. Growth*, **38**, 103 (1977)

99. Sarin V. K., *J. Mater. Sci.*, **10**, 593 (1975)

100. Hu W. B., Zhu Y. Q., Hsu W. K., Chang B. H., Terrones M., Grobert N., Terrones H., Hare J. P., Kroto H. W., and Walton D. R. M., *Appl. Phys. A*, **70**, 231 (2000)

101. Li Y., Bando Y., and Goldberg D., *Adv. Mater.*, **15**, 1294 (2003)

102. Volmer M., and Estermann I., *Z. Phys.*, **7**, 13 (1921)

103. Mayers B., and Xia Y., *Adv. Mater.*, **14**, 279 (2002)

104. Huang M.H., Mao S., Feick H., Yan H., Wu Y., Kind H., Weber E., Russo R., and Yang P., *Science*, **292**, 1897 (2001)

105. Kind H., Yan H., Messer B., Law M., and Yang P., *Adv. Mater.*, **14**, 158 (2002)

106. Goldberger J., Sirbuly D. J., Law M., and Yang P., *J. Phys. Chem. B*, **109**, 9 (2005)

107. Law M., Greene L. E., Johnson J. C., Saykally R., and Yang P., *Nat. Mater.*, **4**, 455 (2005)

108. Wan Q., Li Q.H., Chen Y. J., Wang T. H., He X. L., Li J. P., and Lin C. L., *Appl. Phys. Lett.*, **84**, 3654 (2004)

109. Xiang B., Wang P., Zhang X., Dayeh S. A., Aplin D. P. R., Soci C., Yu D., and Wang D., *Nano Lett.*, **7**, 323 (2007)

110. Wang Z. L., and Song J.H., *Science*, **312**, 242 (2006)

111. Wang X. D., Zhou J., Song J. H., Liu J., Xu N. S., and Wang Z. L., *Nano Lett.*, **6**, 2768 (2006)

112. He J. H., Hsin C. L., Liu J., Chen L. J., and Wang Z. L., *Adv. Mater.*, **19**, 781 (2007)

113. Zhang Y., Wang N., Gao S., He R., Miao S., Liu J., Zhu J. and Zhang X., *Chem. Mater.*, **14**, 3564 (2002)

114. Yao B. D., Chan Y. F., and Wang N., *Appl. Phys. Lett.*, **81**, 757 (2002)

115. Gao P. X., Ding Y., and Wang Z. L., *Nano Lett.*, **3**, 1315 (2003)

116. Park W. -I., Kim D. H., Jung S. -W., and Yi G. -C., *Appl. Phys. Lett.*, **80**, 4232 (2002)

117. Wu J. J., and Liu S. C., *Adv. Mater.*, **14**, 215 (2002)

118. Li Y., Meng G. W., Zhang L. D., and Phillipp F., *Appl. Phys. Lett.*, **76**, 2011 (2000)

119. Harnack O., Pacholski C., Weller H., Yasuda A., and Wessels J. M., *Nano Lett.*, **3**, 1097 (2003)

120. Wang Z. L., *J. Phys. Condens. Matter*, **16**, R829 (2004)

121. Yi G. -C., Wang C. and Park W. -I., *Semicond. Sci. Technol.*, **20**, S22 (2005)

122. Heo Y. W., Norton D. P., Tien L. C., Kwon Y., Kan B. S., Re F., Pearton S. J., and LaRoche J. R., *Mat. Sci. Eng. Res.*, **47**, 1 (2004)

123. Könenkamp R., Word R. C., and Godinez M., *Nano Lett.*, **5**, 2005 (2005)

124. Wang C., Chu X., and Wu M., *Sens. Actuators B*, **113**, 320 (2006)

125. Vanheusden K., Warren W. L., Seager C. H., Tallant D. R., Voigt J. A., and Gnage B. E., *J. Appl. Phys.*, **79**, 7983 (1996)

126. Yang P., Yan H., Mao S., Russo R., Johnson J., Saykally R., Morris N., Pham J., He R., and Choi H. -J., *Adv. Funct. Mater.*, **12**, 323 (2002)

127. Geng C., Jiang Y., Yao Y., Meng X., Zapien J. A., Lee C. S., Lifshitz Y., and Lee S. T., *Adv. Funct. Mater.*, **14**, 589 (2004)

128. Wagner R. S., and Ellis W. C., *Appl. Phys. Lett.*, **4**, 89 (1964)

129. Mitra P., Chatterjee A. P., and Maiti H. S., *Mater. Lett.*, **35,** 33 (1998)

130. Liu Y., Dong J., Hesketh P. J., and Liu M., *J. Mater. Chem.*, **15**, 2316 (2005)

131. Ryu H. -W., Park B. -S., Akbar S. A., Lee W. -S., Hong K. -J., Seo Y. -J., Shin D. -C., Park J. -S., and Choi G. -P., *Sens. Actuators B*, **96**, 717 (2003)

132. Jeong M. -C., Oh B. -Y., Nam O. -H., Kim T., and Myoung J. -M., *Nanotechnology*, **17**, 526 (2006)

133. Koshizaki N., and Oyama T., *Sens. Actuators B*, **66**, 119 (2000)

134. Cavicchi R. E., Poirier G. E., Tea N. H., Afridi M., Berning D., Hefner A., Suehle J. S., Gaitan M., Semancik S., and Montgomery C., *Sens. Actuators B*, **97**, 22 (2004)

135. Modi A., Koratkar N., Lass E., Wei B., and Ajayan P. M., *Nature*, **424**, 171 (2003)

136. Hua G., Wu L., Pan M., Chen Y., Li T., and Zhang X., *Meas. Sci. Technol.*, **17**, 2799 (2006)

137. Choi I. -M., and Woo S. -Y., *Metrologia*, **43**, 84 (2006)

138. Needs R. J., *Phys. Rev. Lett.*, **58**, 53 (1987)

139. Diao J., Gall K., and Dunn M. L., *Nature Mat.*, **2**, 656 (2003)

140. Kucheyev S. O., Bradby J. E., Williams J. S., Jagadish C., and Swain M. V., *Appl. Phys. Lett.*, **80**, 956 (2002)

141. Baxter J. B., and Aydil E. S., *J. Cryst. Growth*, **274**, 407 (2005)